NMR Studies of Ionic Liquids and Polymer Membrane Electrolytes for Batteries and Fuel Cells

by

Sufia Khatun

A dissertation submitted to the Graduate Faculty in Physics in partial fulfillment of the requirements for the degree of Doctor of Philosophy, The City University of New York

2012

This manuscript has been read and accepted for the
Graduate Faculty in Physics in satisfaction of the
dissertation requirement for the degree of Doctor of Philosophy

Prof. Steve G. Greenbaum

December 22, 2011
Date

Chair of Examining Committee

Prof. Igor L. Kuskovsky

December 22, 2011
Date

Executive Officer

Prof. Joel I. Gersten

Prof. Frank J. Owens

Prof. Mark Kobrak

Prof. Sophia N. Suarez
Supervisory Committee

THE CITY UNIVERSITY OF NEW YORK

Abstract

NMR Studies of Ionic Liquids and Polymer Membrane Electrolytes for Batteries and Fuel Cells

by

Sufia Khatun

Advisor: Prof. Steve G. Greenbaum

In this thesis, NMR (Nuclear Magnetic Resonance) spectroscopic techniques are used to study ionic liquids (ILs) and polymer membranes for advanced Li-ion batteries and fuel cells. Besides structural measurements, dynamics and motional properties were also measured using pulsed field gradient spin echo and relaxation experiments. Five projects are described in this thesis. The first two projects involve ^{1}H, ^{19}F, ^{7}Li and ^{13}C NMR transport studies of two different ILs. The third project is a study of Nafion ionomer aggregations where diffusion and viscosity measurements are made. The fourth project involves the structural study of lithium triflate:PEO_3 polymer membranes via ^{7}Li static NMR. The fifth and final project described in the thesis involves ^{27}Al NMR studies of a chloroaluminate ($AlCl_3$) IL and the assessment of the tetrahedral Al species content.

To my son, 'Rishan Islam'

Acknowledgement

First and foremost I would like to express my gratitude to my advisor Prof. Steve G. Greenbaum for his guidance and continuous support throughout the research period in my Ph.D. program. His advice, encouragement and enthusiasm in research had motivated me to get deeper in to the research and complete all those projects and this thesis. Without his support, it would not be possible at all for me.

I would also like to give special thanks to Dr. Phil Stallworth who had an extended hand for me all the times I was working on my projects. He also helped me learning the NMR techniques and solving NMR issues. I also want to thank Dr. Paul Sideris for his valuable advice and help.

I would like to give thanks to my friends and colleagues Dr. Sohan de Silva, Dr. Jaime Farrington, Marc Berman, Rafael Vazquez, Victor Udinwe and Laura Sermasan for making my graduate life joyful. I would also like to thank to all our family friends especially Mujibur Rahman and Taslima Rahman. Their precious advice and friendly encouragements helped me to continue pursuing Ph.D. abroad.

I would like to give special thanks my mother Dilara Begum for her invaluable advice, love and support throughout my whole life and education. I would like to thank my brothers Golam Kibria, Golam sarwar and my sisters Dr. Rabeya Khatun, Sajeda Khatun and Rashida Khatun for their love and support and advice as well.

I would like to thank my husband Mohammed Rafiqul Islam for his inspiration and encouragement that made me have this dream for higher education. Taking share of my happiness and sorrows for every moment and his support helped me all the way to complete my whole Ph.D. journey. Finally I want to give my special thanks to our four and half year old only son Rishan Islam for his cooperation. Without his cooperation, it wouldn't be possible for me to continue pursuing Ph. D.

Table of Contents

List of Tables

List of Figures

Chapter 1

1. Introduction

Energy is an essential commodity in modern life around the world. It was estimated by the Energy Information Administration in 2007 that 86.4% of energy sources in the world are from fossil fuels. Since fossil fuels are non-renewable energy resources, taking millions of year to form, supplies are considered finite. Consequently, given the demand for energy, the acquisition and security of known fossil fuel reserves have led to international tensions. The burning of fossil fuels has had a negative impact on the environment, primarily through the release of large amounts of carbon dioxide that has been implicated in global warming by climate scientists. The anticipated rise in the demand for energy, coupled with the increased concern over the environment, have prompted research into alternative, renewable sources of energy such as solar, wind, tidal, etc. These sources are intermittent, requiring new energy storage methods for their effective utilization. Fuel cells, batteries and supercapacitors are important technologies that are currently being investigated to resolve this energy problem. Fuel cells and batteries have distinct advantages in that they can be used in conjunction with renewable energy sources as well as energy storage devices.

1.1. Batteries

A battery is an energy storage device that converts chemical energy into electrical energy. A battery consists of one or more electrochemical cells. The cell consists of three major components: the anode, the cathode and the electrolyte.

Anode or negative electrode – gives up electrons to the external circuit and is the site of oxidation processes during the electrochemical reaction.

Cathode or positive electrode – accepts electrons from the external circuit and is the site of reduction processes during the electrochemical reaction.

Electrolyte – The electrodes are connected internally by the electrolyte, an ion conductor that transfers charge between the anode and the cathode inside the cell. Different types of electrolytes are used in rechargeable batteries typically characterized as: polymer, gel or liquid electrolytes. The performance of the battery depends critically on the material properties of the electrolyte.

1.2. Operation of a Battery or a Cell

During discharge, with the cell connected to an external load, electrons flow from the anode to the cathode through the external load and thereby generate electricity. In the example of a Zn/Cl_2 Cell, the discharge reaction can be written as:

Anodic Reaction: $Zn \rightarrow Zn^{2+} + 2e$ (loss of electrons)

Cathodic Reaction: $Cl_2 + 2e \rightarrow 2Cl^-$ (gain of electrons)

Overall Reaction for discharge: $Zn + Cl_2 \rightarrow Zn^{2+} + 2Cl^- (ZnCl_2)$

During the recharge of a rechargeable cell, the current is reversed by an external power source. The reaction for charging can be written as:

Cathodic Reaction: $Zn^{2+} + 2e \rightarrow Zn$ (gain of electrons)

Anodic Reaction: $2Cl^- \rightarrow Cl_2 + 2e$ (loss of electrons)

Overall Reaction for Charge: $Zn^{2+} + 2Cl^- \rightarrow Zn + Cl_2$

1.3. Types of Batteries

There are two types of battery: Primary or disposable battery and Secondary or rechargeable battery.

1.3.1. Primary Batteries

The primary battery is convenient, inexpensive and lightweight for portable electronic devices. Primary batteries typically exhibit higher energy densities than rechargeable batteries. The common types of primary batteries are Zinc-Carbon and Alkaline.

1.3.2. Secondary or Rechargeable Batteries

These batteries are also known as storage batteries and are assembled with the active materials in the discharged state. Therefore, these batteries need to be charged before use.

1.4. Different Types of Secondary Batteries

1.4.1. Lead Acid Batteries

The lead acid battery was invented in 1859 by French physicist Gaston Plante. This battery has a low energy to weight ratio, low energy to volume ratio and the cells maintain relatively large power-to-weight ratio. Still the low cost makes this battery most attractive for auxiliary power use in motor vehicles.

1.4.2. Nickel-Cadmium Batteries

The nickel-cadmium battery has been in use since 1899 and is usually available in several cell designs and in a wide range of sizes. Being made of nickel Oxyhydroxide and cadmium electrodes, it is reliable, sturdy and has long lifetime. It also has a high discharge rate and wide temperature range of operation. The application of this battery is in heavy-duty industries as: trucks, mining vehicles, and railway signaling, as well as portable electronics.

Environmental concerns have led to gradual replacement of these batteries by less toxic alternatives.

1.4.3. Nickel Hydrogen Batteries

This rechargeable battery is a hybrid and can be thought of as a combination of battery and fuel cell technologies: nickel-oxide as the positive electrode (i.e. from the nickel-cadmium cell design) and hydrogen as the negative electrode (i.e. from the hydrogen-oxygen fuel cell design). Since these batteries are characterized by long cycle life, high specific energy and high power density, they have applications in space technologies for geosynchronous earth orbit (GEO), commercial communication satellites and low earth orbit (LEO) satellites.

1.4.4. Nickel-Metal Hydride Batteries

The nickel-metal hydride (NiMH) battery is a commercially important rechargeable battery for multiple consumer and vehicle propulsion applications. It was first studied in 1960s as an environmentally safer derivative of the NiCd and the NiH_2 batteries [1]. It uses a hydrogen absorbing alloy for the anode instead of Cd. Beyond the environmental advantages, this battery is characterized by high energy density, flexible cell sizes (from 0.06 to 250 Ah), safe operation at high voltage (≥320 V), long cycle life, low cost compared to NiCd [1].

1.4.5. Nickel-Zinc Batteries

Nickel-zinc batteries have been known for over 100 years as rechargeable small, lightweight power sources with excellent rate discharge capability. The technology has typically a lower cost compared to lithium-ion batteries and has applications in cordless telephones, digital cameras, flashlights, electric bicycles, etc.

1.4.6. Li-ion Batteries

Lithium ion batteries uses lithium storage compounds as positive and negative electrodes, where depending on whether the cell is charging or discharging, Li-ions move back and forth between the positive and the negative electrodes. Lithium cells can produce 1.5V to 4.2V depending on the design and chemical compounds used. Lithium-ion batteries are commonly used for consumer electronics such as: laptop computers, cell phones, MP3 players, digital cameras, power tools, electric bikes as well as military devices and aerospace applications. They are also present in new hybrid and plug-in hybrid electric cars. The main advantages of Li-ion cells are high specific energy (240 Wh/Kg), high energy density (up to 640Wh/L), low self-discharge rate, long cycle life, reduced weight and wide temperature range for operation. All these advantages make the Li-ion cells attractive for use in commercial products. The disadvantages of some lithium batteries are rapid degradation when discharged below 2V and danger of venting when overcharged [1]. The comparable energy density chart for different types of batteries is shown in figure 1.4.6.1.

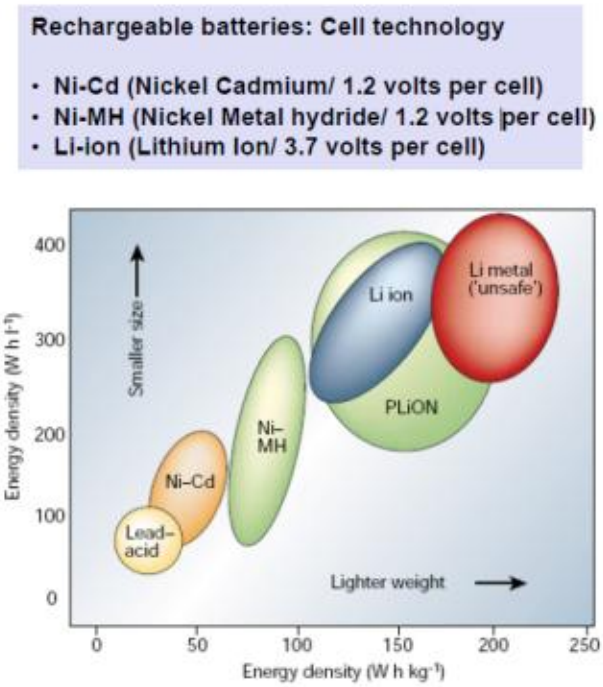

J.-M. Tarascon and M. Armand, Nature 414, 359 - 367 (2001)

Figure 1.4.6.1: Energy density chart for lead-acid, Ni-Cd, Ni-MH, Li-ion, Li metal batteries.

The chemical reactions of Li-ion cells are:

Positive: $LiMO_2 \underset{discharge}{\overset{charge}{\leftrightarrow}} Li_{1-x}MO_2 + xLi^+ + xe^-$

Negative: $C + yLi^+ + ye^- \underset{discharge}{\overset{charge}{\leftrightarrow}} Li_yC$

Overall: $LiMO_2 + \left(\frac{x}{y}\right)C \underset{discharge}{\overset{charge}{\leftrightarrow}} \left(\frac{x}{y}\right)Li_yC + Li_{1-x}MO_2$

During the charging of Li-ion cells, the active positive electrode material is oxidized and the active negative electrode material is reduced. In the above equation, $LiMO_2$ represents the metal oxide positive electrode material (i.e. $LiCoO_2$), C represents the carbonaceous negative electrode material (i.e. graphite). x and y are the molar capacities of

the electrode materials for lithium and are not generally the same because of the presence of irreversible reactions[1].The diagram of a lithium-ion battery is shown in fig 1.4.6.2.

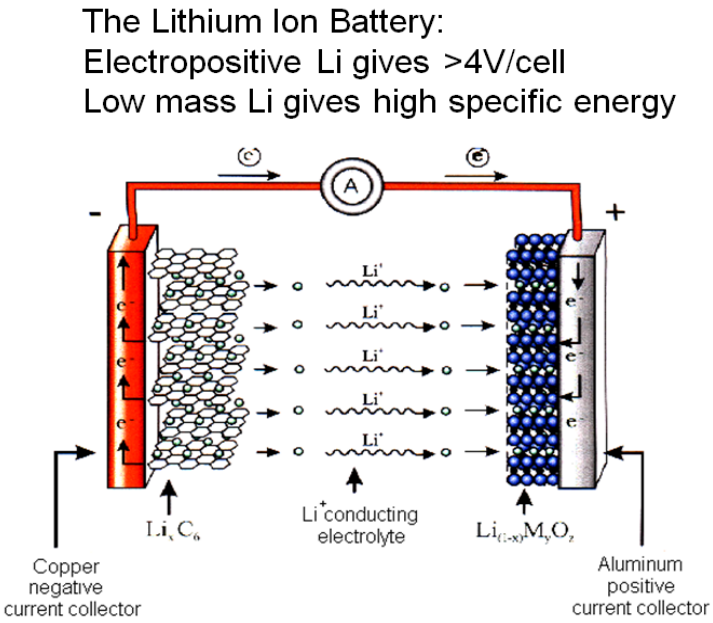

Figure1.4.6.2: The diagram of Lithium ion Battery.

1.5. Fuel Cells

The first fuel cell was developed in 1839 by William Grove, and the first commercial uses of fuel cells were by NASA to generate power for spacecraft. Fuel cells, like batteries, are electrochemical cells that convert chemical energy into electrical energy through chemical reactions involving a specific fuel. They consist of three components as: anode, cathode and electrolyte that allows passage of the charges between the two electrodes. Hydrogen is the most common fuel used in fuel cells.

Fuel cell technology is classified in two ways, depending on the nature of fuel:

1. fuels, such as hydrogen and methanol that oxidize directly inside the fuel cell [1].

2. fuels, such as natural gas or other fossil fuels, that are first converted by reforming to a hydrogen rich gas, then fed into the fuel cell [1].

The fuel cell works through catalytic oxidation of the fuel (H_2 in this example) at the anode into positively charged ions (H^+) and electrons. The electrolyte is chosen that allows transport of the positive ions from anode to cathode, while being electronically non-conducting. The generated electrons travel through an external circuit (load) to perform work. The proton ions then recombine with the electrons in the presence of oxygen at the cathode in a reduction reaction to form water as a byproduct.

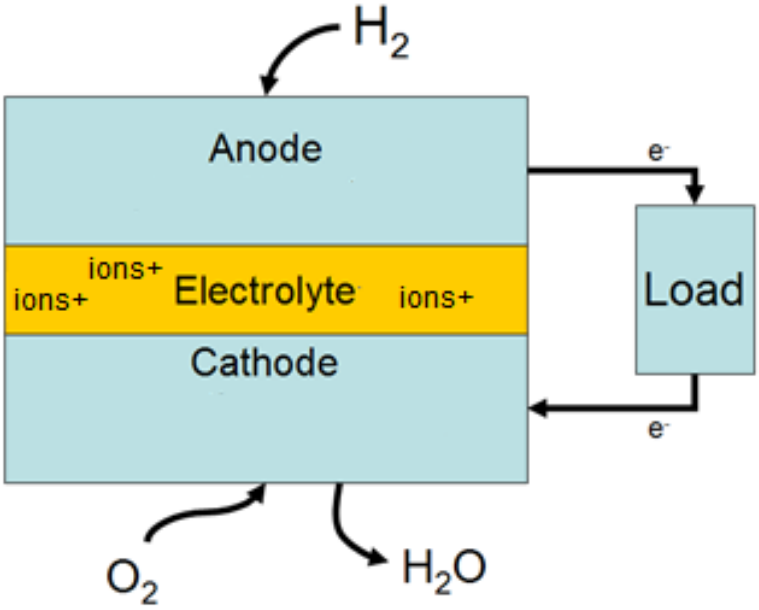

Figure 1.5: A block diagram of a hydrogen fuel cell.

There are different types of fuel cells depending on the electrolytes used: proton exchange membrane fuel cells, alkaline fuel cells, phosphoric acid fuel cells, direct methanol fuel cells, solid oxide fuel cells. Proton Exchange Membrane Fuel Cells (PEMFCs) are one of the popular and efficient fuel cells. Despite their environmental friendliness and efficiency, there are still many challenges in making these fuel cells commercially viable.

Proton Exchange Membrane and Direct Methanol Fuel Cells are described in the following section as these are related with the project mentioned in this thesis.

1.5.1. Proton-Exchange Membrane Fuel Cell (PEMFC)

Proton exchange membrane (PEM) fuel cells use a solid polymer as the electrolyte and hydrogen as the fuel. Nafion, a commercial product made by Du Pont, whose structure is shown in Figure 1.5.1.1, is the most widely used PEM due to its very high proton conductivity. The design of PEMFC is shown in fig. 1.5.1.2.

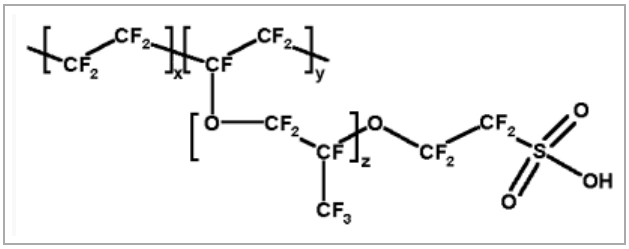

Figure 1.5.1.1: Chemical structure of the polymer Nafion. The subscripts x, y, z represent the number of the respective polymeric units.

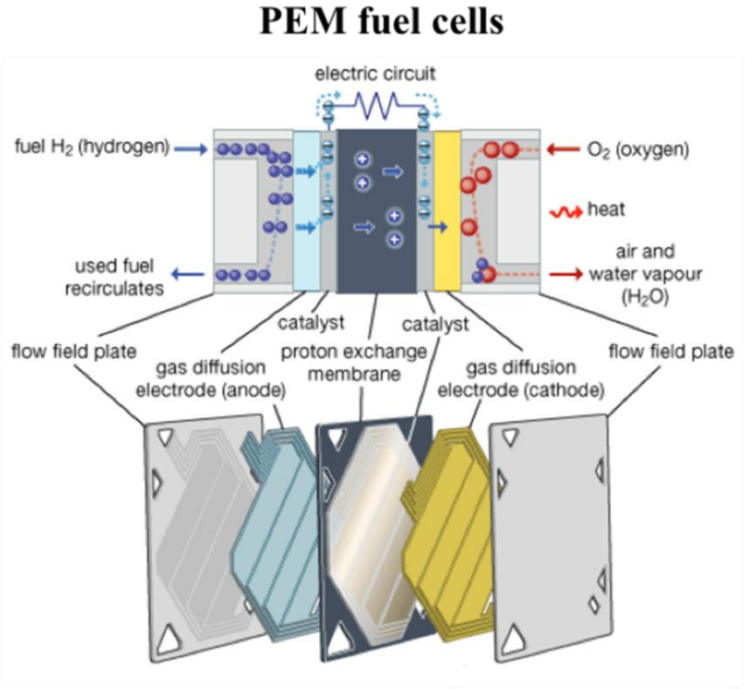

Figure 1.5.1.2: Schematic diagram of a polymer electrolyte membrane (PEM).

The hydrogen molecule is split into positive ions (protons) and electrons at the anode. The chemical reaction at the anode and the cathode sides are as follows:

Anode Reactions: $2H_2 \rightarrow 4H^+ + 4e^-$

Cathode Reactions: $O_2 + 4H^+ + 4e^- \rightarrow 2H_2O$

Overall Cell Reactions: $2H_2 + O_2 \rightarrow 2H_2O$

PEMFCs have a low operating temperature, which allows for quick start up. This makes PEMFCs one of the top candidates for automotive power applications. However, the PEM must be maintained in a hydrated state (~ 20% by weight H_2O). One of the main hurdles in making PEMFCs commercially successful is the high cost of production. Currently, platinum (Pt^0) is used as the major catalytic component in both the reduction of oxygen at the cathode, and the oxidation of hydrogen at the anode, where approximately 0.4 mg Pt/cm^2 and 0.2 mg Pt/cm^2 are required for the cathode and anode respectively for satisfactory short term and long term performance (information from MysticMD Inc).

1.5.2. Direct Methanol Fuel Cell (DMFC)

The DMFC is similar to the PEMFC, however, methanol (CH_3OH) is used instead of H_2 as fuel. Methanol is a widely available chemical and easy to handle [1], and can be stored as a liquid from -97^{o}C to 64.7^{o}C at atmospheric pressure. The energy density of methanol is much higher than lithium and nearly as high as gasoline. The diagram of DMFC is shown in fig. 1.5.2.

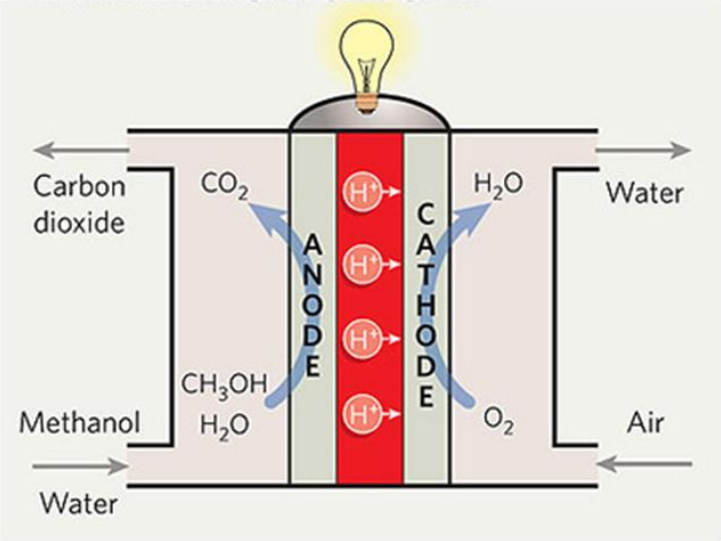

Figure 1.5.2: The basic diagram of DMFC.

At the anode, liquid methanol is oxidized in the presence of water and produces CO_2, protons (H^+) and electrons that travel through the external circuit. The protons travel through the electrolyte and react with oxygen from air and electrons from the external circuit to form H_2O at the cathode. A single anode/electrolyte/cathode unit is called membrane electrode assembly (MEA). The reactions are:

Anode Reaction: $CH_3OH + H_2O \rightarrow CO_2 + 6H^+ + 6e^-$

Cathode Reaction: $\frac{3}{2}O_2 + 6H^+ + 6e^- \rightarrow 3H_2O$

Overall Reaction: $CH_3OH + \frac{3}{2}O_2 \rightarrow CO_2 + 2H_2O$

1.6. Ionic Liquids

1.6.1. Introduction

An ionic liquid is a salt consisting exclusively of cations and anions in the liquid state at ambient temperatures. In conventional salts, attractive forces between oppositely charged ions bind them in a more or less immobile condensed and usually crystalline phase. In the case of the ionic liquid, these attractive forces are smaller and thereby allow more motional freedom between the ions such that a liquid state results. Ionic liquids are also known as molten salts. The first ambient temperature ionic liquid ethyl ammonium nitrate $[EtNH_3][NO_3]$ (m.pt. 12^oC) was discovered in 1914, but interest developed when binary ionic liquids as the mixture of aluminum chloride and N-alkylpyridinium was discovered [9].

There are two categories of ionic liquids: 1) simple salts that consist of a single anion and cation like $[EtNH_3][NO_3]$ and 2) binary liquids where several ionic species are presents like the mixture of aluminum chloride and 1,3-alkylimmidazolium. Examples of simple ILs are shown in figure 1.6.1 [9].

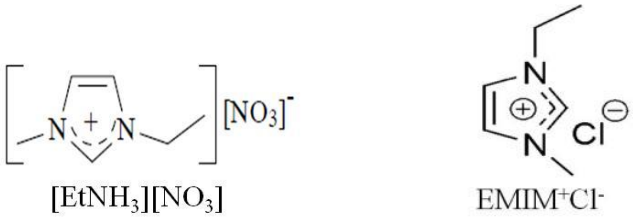

Figure 1.6.1: Structure of simple ionic liquids.

Ionic liquids are usually composed of organic cations and organic or inorganic anions where both ions are large. This combination of large cation and anion with delocalized charge helps to reduce the lattice energy of the crystalline form of the salt and hence, lower

the melting point [9]. Another advantage is that ionic liquids consist only of ions and therefore have high ion conductivity.

The common cations are immidazolium, pyridinium, quaternary ammonium, and quaternary phosphonium. Some typical anions are the chloride (Cl^-) and other halogens, triflate ($CF_3SO_3^-$), tetrafluoroborate(BF_4^-), hexafluorophosphate (PF_6^-), bis(trifluoromethylsulfonyl)-imide($TFSI^-$) and dicyanamide(DCA^-), dicyanotriazole ($DCTA^-$). Some of these anions and cations are shown in figure 1.6.2.

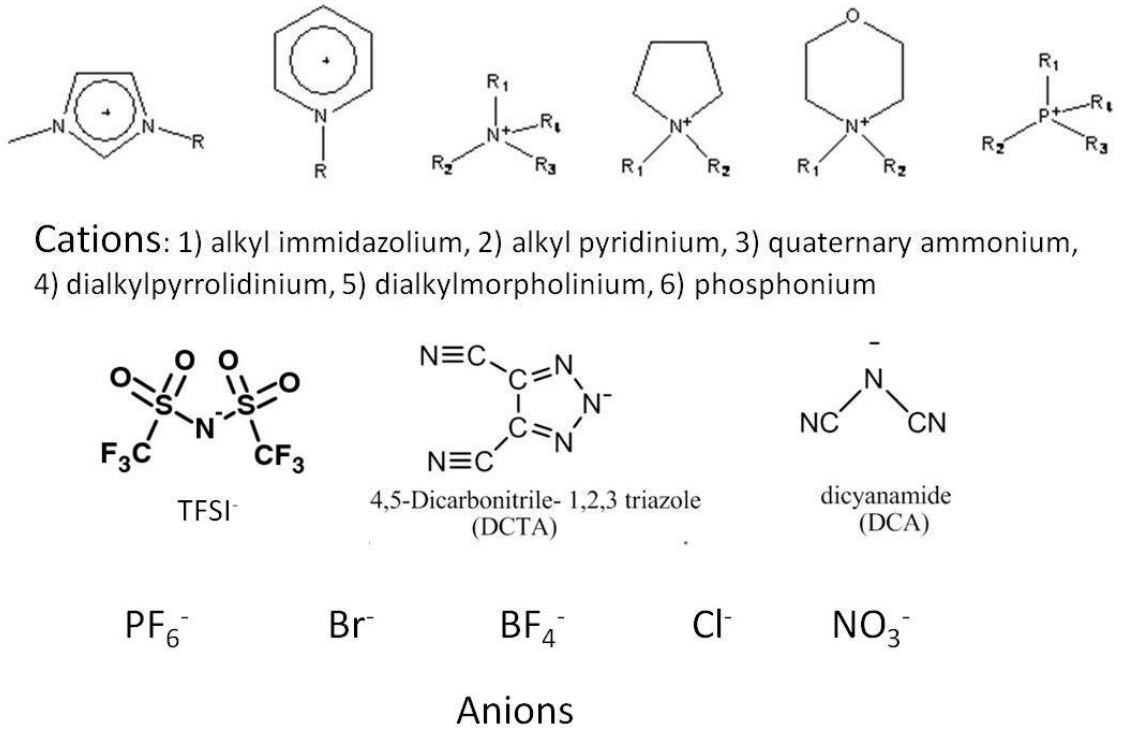

Figure 1.6.2: The chemical structures of Cations and Anions of Ionic Liquids.

In that there is virtually unlimited structural variation for candidate cations and their contribution with different anions, so there are unlimited possibilities to design ionic liquids. Therefore, by altering the structure, the properties of ionic liquids such as melting point, viscosity, density, polarity and hydrophobicity can be varied. For example, the melting points

of 1-alkyl-3-methylimidazolium tetrafluoroborates and hexafluorophosphates are a function of the length of the 1-alkyl group, and they form liquid crystalline phases for alkyl chain lengths over 12 carbon atoms [9].

1.6.2. Properties of Ionic Liquids

Ionic liquids have unique characteristics that make them well suited for use in industrial application. These properties include: non-flammability, low vapor pressure, high thermal stability, good electrochemical stability, low melting points and high ion content.

Non-flammability: This is obviously a great advantage to have in energy devices as there are very few other molecular solvents with this property. It has been shown from studies that while direct application of an external flame can make organic salts present in the electrolytes burn, the fire is immediately extinguished when the external flame is removed [11]. Therefore, ionic liquids are also known as "self-extinguishing" or "fire retardant". This property also helps to avoid "thermal runaway" (strong exothermic reaction that are accelerated by temperature rise) that can occur in the rechargeable lithium ion batteries.

Low vapor pressure: Ionic liquids have negligible vapor pressure and this property helps ILs to be non-flammable. Ionic liquids do not evaporate under normal conditions because the attractive electrostatic forces between the ions are enough to counteract surface dispersive forces. This means that ionic liquids can be 'dried' under vacuum even at elevated temperatures. This is an important consideration because conventional electrolytes are made from solvents that have been dried over molecular sieves

or fabricated under strict anhydrous conditions. Additionally, conventional electrolytes need to be stored and handled under rigorously controlled conditions in order to avoid moisture. All this adds to the cost of using conventional electrolytes. So it is clear why ionic liquids have attracted attention for battery applications.

High thermal stability: Ionic liquids have very high thermal stabilities relative to conventional electrolytes. Many well behaved ionic liquids, like 1-ethyl-3-methylimidazolium tetrafluoroborate ($EMIM^+$- BF_4^-) and 1-butyl-3-methylimidazolium hexafluorophosphate ($BMIM^+$-PF_6^-), are thermally stable up to 300^{o}C. This property is of value where higher operating temperatures are desirable, for example in battery applications for down-hole drilling, engine sensors, etc.

Good electrochemical stability: Ionic liquids are characterized by a wide electrochemical window, i.e. up to 6 volts. The electrochemical window is defined by the electrochemical stability against oxidation and reduction as:

$$Cation^+ + e^- \longrightarrow \text{Neutral species}$$

$$Anion^- \longrightarrow \text{Neutral species} + e^-$$

The broad electrochemical window allows for the use of very strong reducing and oxidizing agents as anodes and cathodes. Under these conditions, therefore, high cell voltages and high energy densities can be produced [11]. Examples of good electrochemically stable ionic liquids are N-butyl-N-methylpyrrolidinium bis(trifluoromethylsulfonyl)imide and N-methyl-N-trioctylammonium bis (trifluoromethylsulfonyl)imide.

Low melting points: For reasons mentioned previously (i.e. high ionic mobility), ionic liquids are usually designed with low melting temperatures. Some ionic liquids have temperature ranges from -40^{o}C to +200^{o}C. 1-ethyl-3-methylimidazolium tetrafluoroborate ($BMIM^{+}$-BF_4^{-}) has a melting point at about -80^{o}C.

High ion content: Ionic liquids have very high concentration of charge carriers as ILs are composed of 100% ions. The payoff, therefore, is that ILs have very high ionic conductivities although they have high viscosities as a drawback. The high concentration of ions helps to overcome concentration polarization in batteries during high rate discharge [11]. This property is also important in capacitors where the charge storage is a function of charge carrier concentration.

1.6.3. Application of Ionic Liquids

Ionic liquids have various industrial applications because of their attractive intrinsic properties. Some applications of ILs are:

1. Electroplating: ILs are useful in electrodeposition because of the properties: high metal solubility, wide potential windows, non-flammability, high conductivity resulting in low ohmic losses and good throwing power, and easy of handling. It is possible to direct electroplating of metals on water sensitive materials as Al, Mg and light alloys with ILs. ILs are also useful to obtain quality coating under anhydrous condition. As ILs are non-aqueous, there is negligible hydrogen produced during electroplating and the coating possesses much superior mechanical properties of pure metal, which make possible crack-free and corrosion-resistant deposition [16].

Therefore, it allows the use of thinner deposition that reduces the overall material and consumed energy.

2. Chemical Industry: Room temperature ILs are useful as solvents. Room temperature ILs are able to solubilize inorganic as well as organic compounds [13]. Therefore, ILs are useful for chemical analysis as liquid – liquid extractors. The first industrial ILs application was the Biphasic Acid Scavenging utilizing ionic liquids (BASIL), in which 1- alkylimidazole scavenged the acid from an existing process.

3. Cellulose Processing: Cellulose is the most abundant bio-renewable resource. Although cellulose is not soluble in water and most organic liquids, it can be dissolved in ILs, such as 1-butyl-3-methylimidazolium chloride (BMIMCl) and 1-allyl-3-methylimidazolium chloride (AMIMCl).

   In 1934, Graenacher first suggested that molten N-ethylpyridinium chloride could be used in the presence of a nitrogen-containing base [15]. Cellulose can be regenerated from its ionic liquid by addition of water or ethanol and acetone [14].

4. Dispersants: Ionic liquids are useful as dispersing agents in paints to expedite finishing and drying properties.

5. Lithium Batteries: ILs with lithium salt are now the most promising electrolytes used in Lithium Batteries due to their specific properties, such as non-flammability, high ion conductivity, non-volatility and thermal stability. As the conventional electrolytes are volatile organic solvents, the use of conventional electrolytes can

cause accidental vaporization because of local overheating which can generate gaseous products because of their chemical decomposition [17].

6. Others: Ionic liquids have other applications such as biological reaction media, in purification of gases, metal ions removal, heat transfer and storage medium in solar thermal systems and nuclear fuel reprocessing.

Chapter 2

2. Theoretical Background of NMR

2.1. NMR Phenomenon

Nuclear Magnetic Resonance (NMR) is a spectroscopic technique that exploits the magnetic properties of nuclei to probe surrounding structure and dynamic properties of ions, atoms, molecules, and condensed matter. NMR signals were observed for the first time in 1946 by the two research groups, that of F. Bloch, W. W. Hansen, M. E. Packard and that of E. M. Purcell, H. C. Torrey and R. V. Pound. Bloch and Purcell both were awarded the Nobel Prize in 1952 for their discovery.

Fundamentally, NMR involves the interaction of radio frequency electromagnetic radiation with "spin-active" nuclei in the presence of a strong magnetic field. Certain nuclei such as ^{1}H, ^{13}C, ^{19}F, ^{2}H and ^{14}N, for example, have a non-zero spin angular momentum and therefore corresponding magnetic moment μ given by,

$$\mu = \gamma I \text{ and } I = m\hbar \quad \ldots\ldots\ldots\ldots\ldots\ldots\ldots\ldots (2.1.1)$$

where $\hbar$ is the reduced Planck's constant, γ the magnetogyric ratio, m the magnetic quantum number of the nucleus and I the net nuclear spin. When such nuclei are placed in a magnetic field B_0 whose direction is arbitrarily taken along the z – axis, the nuclei precess about the direction of magnetic field as in fig. 2.1.1 and are split the energy levels of the spin states.

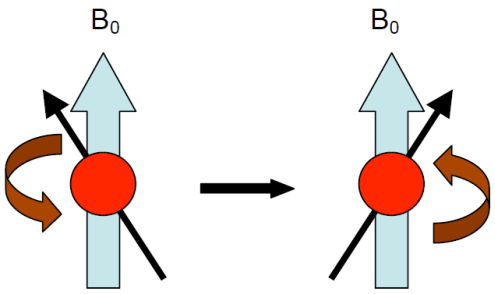

Figure 2.1.1: Spin precession around a static magnetic field B_0

For example, if a proton is placed in a static magnetic field B_o which has spin ½, there are two energy levels corresponding to the two m (quantum number) values +1/2 and -1/2. The energy of each level is given by,

$$E = -\mu_z B_0 = -\gamma I_z B_0 \quad \ldots\ldots\ldots\ldots\ldots\ldots \quad (2.1.2)$$

and the energy difference between the two adjacent energy levels for spin ½ is:

$$\Delta E = 2\mu B_o \quad \ldots\ldots\ldots\ldots\ldots\ldots\ldots\ldots \quad (2.1.3)$$

The energy spacing between the levels is thus directly proportional to the static external magnetic field B_0. Figure 2.1.2 shows the energy spacing between the two levels of a spin ½ nucleus as a function of magnetic field.

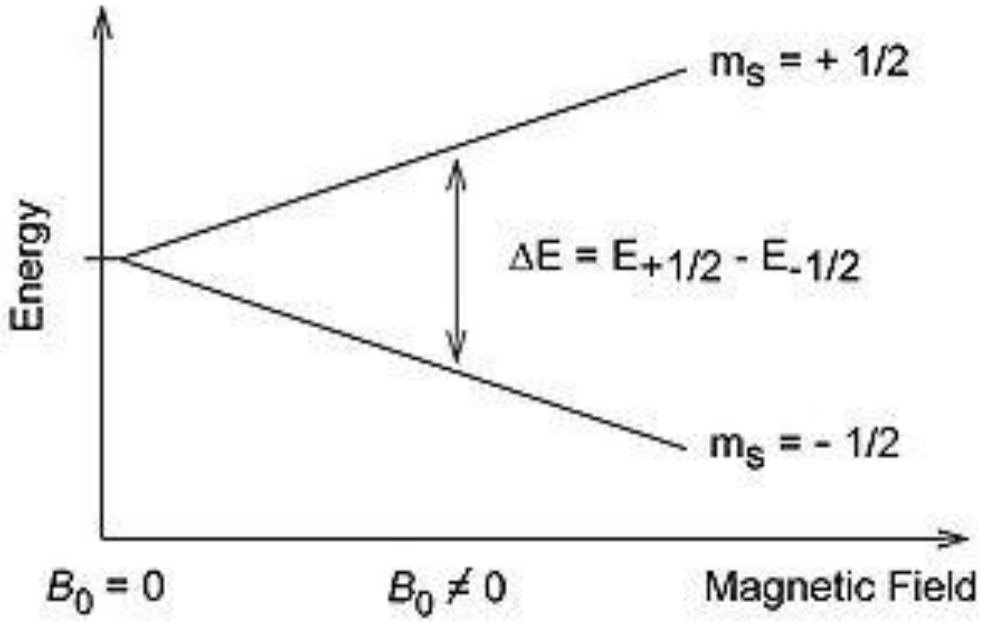

Figure 2.1.2: Schematic representation of the energy spacing between the +1/2 and -1/2 energy levels of a spin-½ nucleus as a function of the strength of the magnetic field B_0.

In the lowest energy orientation, the magnetic moment of the nucleus is most closely aligned and in the highest energy orientation it is least closely aligned with the external magnetic field. At equilibrium, there is a slight excess of nuclei in the lower energy state than in the upper energy state and this difference is responsible for the NMR signal. A vector representation of the preferential alignment of the magnetic moments is shown in Figure 2.1.3.

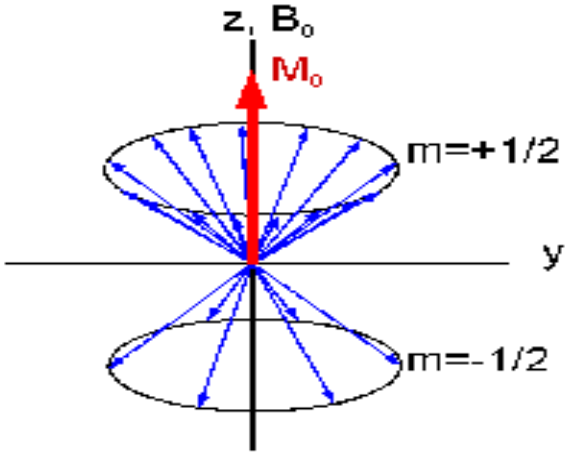

Figure 2.1.3: A vector representation of the magnetic moments of spins in one of two (blue) states of spin- ½ nuclei in the presence of an external magnetic field B_0. The red vector represents the net magnetic moment M_0 which is preferentially aligned with B_0.The nuclei precess about B_0 at the larmor frequency, as represented by the cones.

In quantum mechanics, the low energy state is described by the spin function α and high energy state is described by the spin function β. The ratio of the populations of the two states is given by the Boltzmann distribution:

$$\frac{N_\beta}{N_\alpha} = \exp\left(\frac{-\Delta E}{k_B T}\right) \approx 1 - \frac{\Delta E}{k_B T} = 1 - \frac{\gamma \hbar E}{k_B T} \qquad \ldots\ldots\ldots\ldots\ldots\ldots\ldots\ldots (2.1.4)$$

where N_α is the population of the lower energy state, N_β is the population of the higher energy state, ΔE is the energy difference between the states, k_B is the Boltzmann constant and T is the absolute temperature.

If radio frequency electromagnetic radiation is applied in the direction perpendicular to the external magnetic field and at a frequency that exactly matches the precessional frequency of the nucleus, then the nucleus flips from lower energy state to the higher energy

state by absorbing a photon of energy $h\omega_o$. The precessional frequency of the nucleus is called the Larmor frequency ω_0 and is given by,

$$\omega_0 = -\gamma B_0 \quad \text{..... (2.1.5)}$$

The effect of applying a radiofrequency pulse is as follows

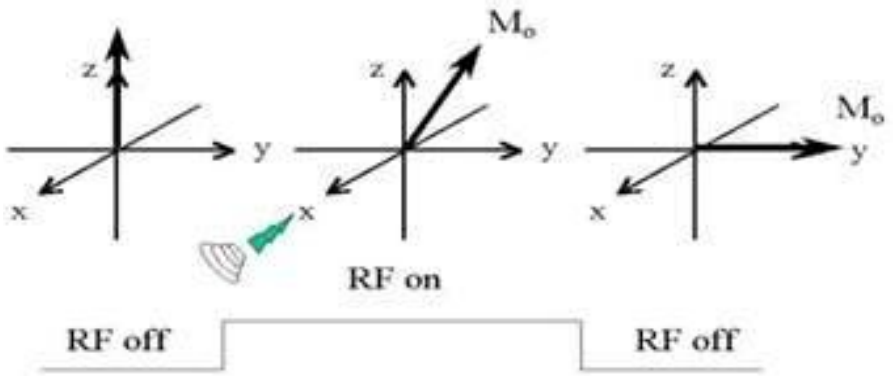

Figure 2.1.4: The nutation of net magnetization by RF pulse.

The flip angle or nutation angle θ_{rf} of an on-resonance pulse is the angle that the rf field B_1 (rf field in x direction) rotates the magnetization away from B_0 during time τ which is given by

$$\theta_{rf} = 2\pi \gamma \tau B_1 \quad \text{..... (2.1.6)}$$

where τ is the duration of rf pulse. τ can be chosen to flip the angle $\pi/2$ or π to obtain maximum transverse magnetization or inverted equilibrium magnetization.

2.2. NMR Relaxation

When the radio frequency (rf) pulse is switched on in an NMR experiments, the magnetization vector M_o is initially perturbed from its equilibrium state through an angle θ as described above. After the pulse is switched off, the magnetization eventually relaxes back to its equilibrium state through relaxation processes. The motion of the magnetization vector, both during the application of the radiofrequency field and in the subsequent relaxation, was mathematically described by F. Bloch through two first order processes as:

$$\frac{dM_z}{dt} = -\frac{M_z - M_0}{T_1}$$

……………………………… (2.2.1)

and $$\frac{dM_x}{dt} = -\frac{M_x}{T_2}, \ \frac{dM_y}{dt} = -\frac{M_y}{T_2}$$

which are known as the Bloch equations. The reciprocals T_1^{-1} and T_2^{-1} of the relaxation times correspond to the rate constants for the longitudinal or spin-lattice and transverse or spin-spin relaxations respectively. The relaxation of the magnetization along the external magnetic field is called the longitudinal or spin-lattice relaxation because in this process energy is exchanged between the spins and the lattice. The charateristic time for this relaxation process is known as the spin-lattice relaxation times T_1. The relaxation of the magnetization in the X-Y plane is called transverse or spin-spin relaxation because in this process energy is exchanged between the spins.

The spin lattice relaxation times T_1 and spin spin relaxation times T_2 are measured by solving Bloch's equations. Working with the proper boundary conditions, the solutions are given as:

$$M_z = M_o (1 - e^{-t/T1}) \quad \ldots\ldots\ldots\ldots\ldots\ldots \quad (2.2.2)$$

And $$M_{XY} = M_{XYo}\, e^{-t/T2} \quad \ldots\ldots\ldots\ldots\ldots\ldots\ldots\ldots \quad (2.2.3)$$

The corresponding exponential recovery and decay curve are shown below:

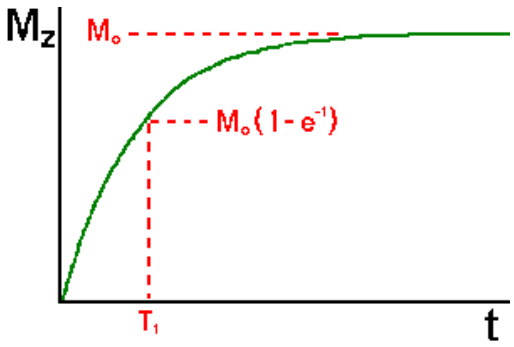

Figure 2.2.1: The exponential curve for T_1 measurements.

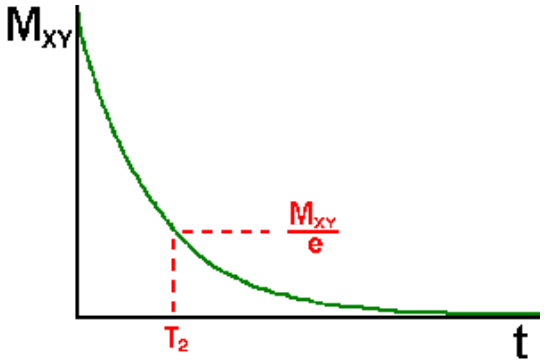

Figure 2.2.2: The exponential curve for T_2 measurements.

Typically there are four main interactions that provide a pathway of energy exchange governing T_1 and T_2 relaxation processes. The main interactions are magnetic dipole-dipole,

nuclear quadrupole, chemical shift anisotropy and scalar coupling. These interactions act in a dynamic sense by modulating the local magnetic field about the nuclear spin. The interaction is detectable if the modulation frequency is within 1 MHz or so of the larmor frequency. Brownian motion that occurs in liquids can cause fluctuations, the Fourier analysis of these motions in terms of frequency is described by the spectral density function j(ω) defined as:

$$j(\omega) = A\frac{\tau_C}{1+\omega^2{\tau_C}^2} \quad \text{..... (2.2.4)}$$

where A depends on the specific relaxation mechanism and ω the angular frequency. τ_c the correlation time, is typically expressed by the Arrhenius relation for thermally activated processes:

$$\tau_c = \tau_0 \exp\left(\frac{E_a}{RT}\right) \quad \text{..... (2.2.5)}$$

where τ_0 is known as the correlation time constant which represents the frequency of attempts to overcome the energy barrier, E_a is the activation energy and R the universal gas constant.

2.3. NMR Interaction

2.3.1. Chemical Shift

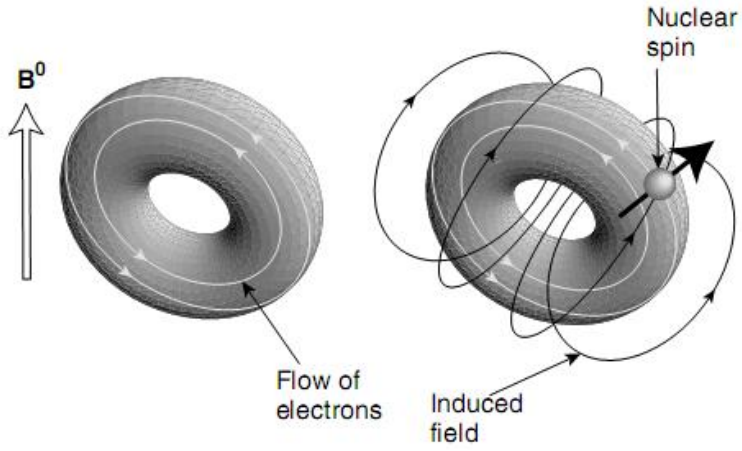

Figure 2.3.1.1: Mechanism of chemical shift.

If an atom is placed in an external magnetic field, electronic motions within the atomic orbitals will responds in fashion, similar to the classical Lenz's law, generating an induced and oppositely directed magnetic field as in fig. 2.3.1.1. This secondary (induced) magnetic field contributes to the external field to produce a total or effective magnetic field at the nucleus. The interaction due to the secondary magnetic field at the nucleus is known as the chemical shift interaction. Depending on whether the effective magnetic field is less than or greater than the applied magnetic field B_o, the effect is termed 'shielding' or 'deshielding' respectively. The chemical shift interaction is expressed by the equation,

$$B_{eff} = (1-\sigma)B_0 \quad \ldots\ldots\ldots\ldots\ldots\ldots\ldots \quad (2.3.1.1)$$

here, σ is the shielding constant (dimensionless). Thus, due to the induced field, the resonance frequency is slightly shifted from the Larmor frequency. The resonance condition becomes:

$$\nu_1 = \frac{\gamma}{2\pi}(1-\sigma)B_0 \quad \text{..... (2.3.1.2)}$$

where ν_1 is the chemical shift frequency and γ is the magnetogyric ratio. The total spectral frequency in absolute units is the Larmor frequency plus the chemical shift frequency. Typically, chemical shifts are not given in absolute frequencies (Hz). Instead, ppm units are used on a scale referenced to a specific line in the spectrum of a standard chemical. The chemical shift δ_{iso} in this way, is given by:

$$\delta_{iso} = \frac{\nu - \nu_{ref}}{\nu_{ref}} \quad \text{..... (2.3.1.3)}$$

The Hamiltonian of the chemical shift interaction with a spin I is

$$\hat{H}_{cs} = \gamma \hat{I} \cdot \sigma \cdot B_0 \quad \text{..... (2.3.1.4)}$$

the term σ is expressed as a second rank Cartesian tensor and called the shielding tensor. It is represented by 3×3 matrix as:

$$\begin{pmatrix} \sigma_{xx} & \sigma_{xy} & \sigma_{xz} \\ \sigma_{yx} & \sigma_{yy} & \sigma_{yz} \\ \sigma_{zx} & \sigma_{zy} & \sigma_{zz} \end{pmatrix} \quad \text{..... (2.3.1.5)}$$

The product of the shielding tensor expressed in the laboratory frame with the magnetic field B_o along the z – axis, the effective magnetic field B_{loc} at a nucleus.

$$B_{loc} = \sigma^{lab} \cdot B_0 = \begin{pmatrix} \sigma_{xx}^{lab} & \sigma_{xy}^{lab} & \sigma_{xz}^{lab} \\ \sigma_{yx}^{lab} & \sigma_{yy}^{lab} & \sigma_{yz}^{lab} \\ \sigma_{zx}^{lab} & \sigma_{zy}^{lab} & \sigma_{zz}^{lab} \end{pmatrix} \cdot \begin{pmatrix} 0 \\ 0 \\ B_0 \end{pmatrix} = \begin{pmatrix} \sigma_{xz}^{lab} B_0 \\ \sigma_{yz}^{lab} B_0 \\ \sigma_{ZZ}^{lab} B_0 \end{pmatrix} \quad \text{..... (2.3.1.6)}$$

The shielding tensor is generally given in its principal axis frame (PAF) with diagonal components as:

$$\sigma^{PAF} = \begin{pmatrix} \sigma_{xx}^{PAF} & 0 & 0 \\ 0 & \sigma_{yy}^{PAF} & 0 \\ 0 & 0 & \sigma_{zz}^{PAF} \end{pmatrix} \quad \text{..... (2.3.1.7)}$$

The numbers along the resulting diagonal of σ^{PAF} are the principal values of the shielding tensor. The orientation of the principal axis frame is determined by the local environment of the nucleus in which interactions take place. The three principal values of an interaction tensor can be expressed as the isotropic value δ_{iso}, the anisotropy Δ_A and asymmetry η_A of the interaction as:

$$\delta_{iso} = \frac{1}{3}\left(\delta_{xx}^{PAF} + \delta_{yy}^{PAF} + \delta_{zz}^{PAF}\right) \quad \text{..... (2.3.1.8)}$$

$$\Delta_A = \delta_{zz}^{PAF} - \delta_{iso} \quad \text{..... (2.3.1.9)}$$

$$\eta_A = \frac{\delta_{xx}^{PAF} - \delta_{yy}^{PAF}}{\Delta_A} \quad \text{..... (2.3.1.10)}$$

2.3.2. Dipolar Coupling

For two nuclei with spins I_1 and I_2 (and corresponding magnetic moment μ_i) separated by a distance r as in the figure below.

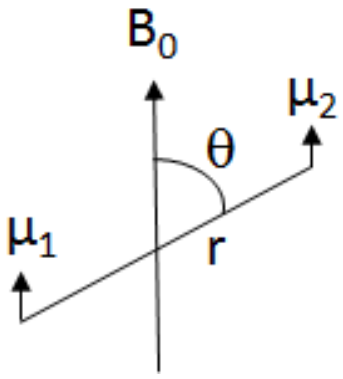

Figure 2.3.2.1: The dipolar interaction of two nuclear spins μ_1 and μ_2.

the energy of interaction between the two magnetic dipoles, μ_1 and μ_2 is

$$E = \frac{\mu_0}{4\pi}\left[\left(\vec{\mu}_1.\vec{\mu}_2\right)r^{-3} - 3\left(\vec{\mu}_1.\vec{r}\right)\left(\vec{\mu}_2.\vec{r}\right)r^{-5}\right] \quad \ldots\ldots\ldots\ldots\ldots\ldots \text{(2.3.2.1)}$$

where μ_0 is the permeability constant and is equal to $4\pi\times10^{-7}$kg.m.s^{-2}.A^{-2}. The Hamiltonian for two interacting nuclear spins is

$$H_D = \frac{\vec{\mu}_1.\vec{\mu}_2}{r^3} - \frac{3\left(\vec{\mu}_1.\vec{r}\right)\left(\vec{\mu}_2.\vec{r}\right)}{r^5} \quad \ldots\ldots\ldots\ldots\ldots\ldots\ldots \text{(2.3.2.2)}$$

where $\mu_1=\gamma\hbar I_1$, $\mu_2=\gamma\hbar I_2$. As there is an angular dependency, the Hamiltonian can be expressed in terms of spherical coordinates as:

$$\hat{H}_D = \frac{\mu_0\gamma_1\gamma_2\hbar^2}{r^3}\left(A+B+C+D+E+F\right) \quad \ldots\ldots\ldots\ldots\ldots\ldots \text{(2.3.2.3)}$$

Where

$$A = \hat{I}_{1Z}\hat{I}_{2Z}\left(1-3\cos^2\theta\right)$$

$$B = -\frac{1}{4}\left[\hat{I}_1^+\hat{I}_2^- + \hat{I}_1^-\hat{I}_2^+\right]\left(1-3\cos^2\theta\right)$$

$$C = -\frac{3}{2}\left(\hat{I}_1^+\hat{I}_{2Z} + \hat{I}_{1Z}\hat{I}_2^+\right)\sin\theta\cos\theta e^{-i\phi}$$

$$D = -\frac{3}{2}\left[\hat{I}_1^-\hat{I}_{2Z} + \hat{I}_{1Z}\hat{I}_2^-\right]\sin\theta\cos\theta e^{i\phi}$$

$$E = -\frac{3}{4}\hat{I}_1^+\hat{I}_2^+\sin^2\theta e^{-2i\phi}$$

$$F = -\frac{3}{4}\hat{I}_1^-\hat{I}_2^-\sin^2\theta e^{2i\phi}$$

The dipolar interaction is typically much smaller than the Zeeman interaction. Its strength depends on the relative orientation of the interacting dipoles and their separation distances. Dipolar coupling is very useful in the study of molecular structure as it can be used to extract internuclear distances. In typical solid state NMR experiments there are a very large number of spin-spin dipolar interactions. These have the resultant effect of broadening the NMR spectrum more or less symmetrically. In most cases, the dipolar interactions can be treated as Gaussian and/or Lorentzian convulations of the polycrystalline powder pattern.

2.3.3. Quadrupolar Interaction

Nuclei with spin greater than ½ have non-spherical nuclear charge distributions. In such cases, an electric quadrupole moment specific to each nuclear isotope is found, and nuclei are referred to as quadrupolar nuclei. The interaction between the nuclear electric quadrupole moment and the electric field gradient at the nucleus is called the Quadrupolar Interaction. Electric field gradients are found at atomic sites in all solids and arise from non-spherical charge distributions of neighboring nuclei and electrons. The Hamiltonian of the quadrupole interaction is:

$$\hat{H}_Q = \frac{eQ}{2I(I-1)\hbar}\hat{I}.V.\hat{I}\,, \qquad (2.3.3.1)$$

where V is the electric field gradient, $\hat{I}$ is the nuclear spin vector and Q is the nuclear quadrupole moment. The electric field gradient (EFG) is diagonal in its principal axis system (PAS)

$$\begin{pmatrix} V_{XX} & V_{XY} & V_{XZ} \\ V_{YX} & V_{YY} & V_{YZ} \\ V_{ZX} & V_{ZY} & V_{ZZ} \end{pmatrix} \overset{Rotation}{\leftrightarrow} \begin{pmatrix} V_{XX} & 0 & 0 \\ 0 & V_{YY} & 0 \\ 0 & 0 & V_{ZZ} \end{pmatrix} \quad \ldots\ldots\ldots\ldots\ldots\ldots\ldots\ldots (2.3.3.2)$$

where $V_{XX}+V_{YY}+V_{ZZ}=0$ and $|V_{ZZ}| > |V_{XX}| > |V_{YY}|$

In the EFG principal axis system, the quadrupolar Hamiltonian is given as:

$$H_Q = \frac{e^2qQ}{4I(2I-1)\hbar}\left[3I_Z^2 - I(I+1) + \eta\left(I_X^2 - I_Y^2\right)\right] \ldots\ldots\ldots\ldots\ldots\ldots\ldots\ldots (2.3.3.3)$$

Where e is the magnitude of the electron charge and eq=V_{ZZ}, the largest component of EFG and η is called the asymmetry parameter defined as:

$$\eta = \frac{V_{XX} - V_{YY}}{V_{ZZ}} \quad \ldots\ldots\ldots\ldots\ldots\ldots\ldots\ldots \quad (2.3.3.4)$$

If we assume the electric field gradient has axial symmetry ($V_{XX}=V_{YY}$ or η=0) then the Hamiltonian of quadrupolar interaction $\hat{H}_Q$ in the lab coordinate system becomes

$$\hat{H}_Q = \frac{e^2qQ}{4I(2I-1)}\left[3I_Z{}^2\cos^2\theta + 3I_X{}^2\sin^2\theta + 3(I_ZI_X + I_XI_Z)\sin\theta\cos\theta - I(I+1)\right] \qquad (2.3.3.5)$$

The first order energy correction to the energies of the Zeeman levels from quadrupole coupling using perturbation theory is:

$$E_m{}^{(1)} = \frac{e^2qQ}{4I(2I-1)}\left(3m^2 - I(I+1)\right)\frac{1}{2}\left[\left(3\cos^2\theta - 1\right) + \eta\cos 2\varphi\sin^2\theta\right] \qquad (2.3.3.6)$$

The effect of quadrupolar coupling is to shift the nuclear energy levels as follows for a I=1 case:

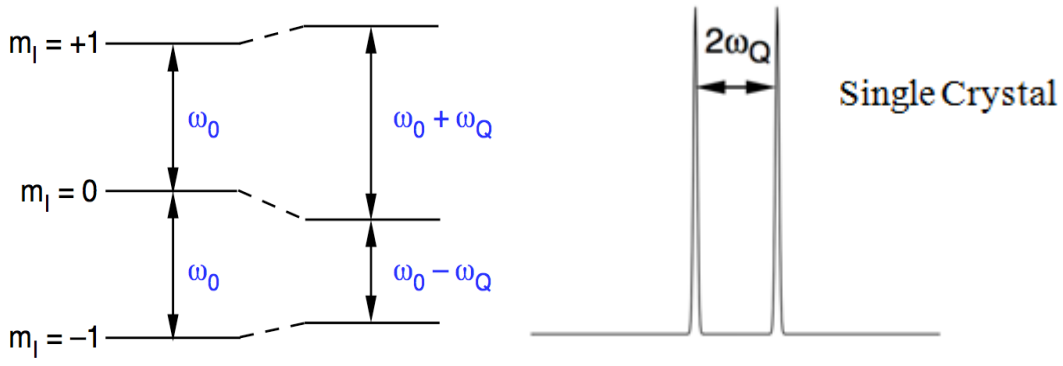

Figure 2.3.3.1: Nuclear energy levels due to the effect of quadrupolar coupling and corresponding pattern for a single crystal.

For a single crystal, the chemical shift depends on the orientation of solid with respect to the magnetic field and this is called chemical shift anisotropy (CSA). The lineshape observed in the NMR spectrum (Fig. 2.3.3.2) is a sum of individual lines for all possible molecular orientations with a characteristic shape called a powder pattern [18].

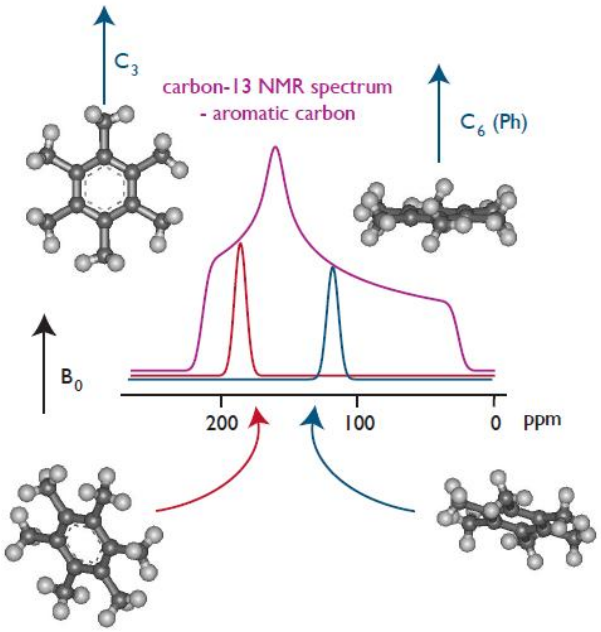

Figure 2.3.3.2: The powder lineshape for a single crystal.

A powder consists of many crystals, all with different orientations. In a powder sample, all possible orientations of the internuclear vector are present, resulting in a pattern known as Pake doublet as in following figure [18].

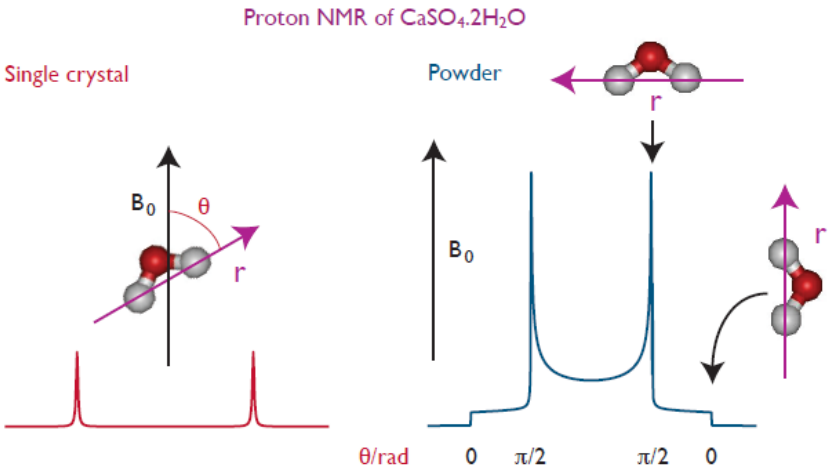

Figure 2.3.3.3: ^{1}H NMR Powder pattern of a powder and comparison with single crystal.

The powder pattern of first order quadrupolar interaction for spin 3/2 is shown in figure 2.3.3.4.

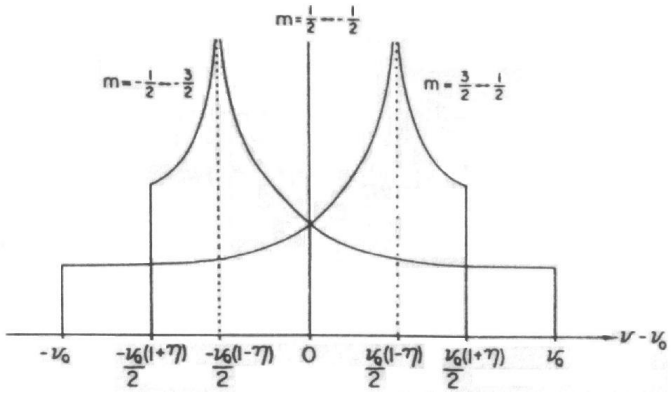

Figure 2.3.3.4: The satellite view of first order quadrupolar interaction for spin 3/2.

It is calculated by integrating the angular dependent satellite transitions ($\pm\frac{3}{2}\Leftrightarrow\pm\frac{1}{2}$) over all solid angles.

2.4. Basic NMR Pulse Sequences

NMR experiments in this thesis were performed using a Varian Direct Digital Drive Spectrometer operating at 7.1 T (300 MHz) and a Varian Inova spectrometer operating at 11.4 T (500MHz). The pulse sequences used in this research are described in this Section.

2.4.1. Single Pulse

This is the simplest and most basic pulse sequence for NMR experiments. The single pulse sequence consists of one $\pi/2$ pulse followed by a delay and signal acquisition, as in figure 2.4.1. Action of the pulse along the x-axis is to flip the magnetization from its equilibrium position (along the z-axis) to the xy plane. The magnetization signal is maximized by a $(\pi/2)_x$ excitation pulse (where subscript x denotes that the pulse phase is along the x-axis) and an NMR free induction decay (FID) or time domain signal is detected after the pulse delay (DE). The NMR frequency spectrum is obtained through Fourier transformation and additional processing of the FID.

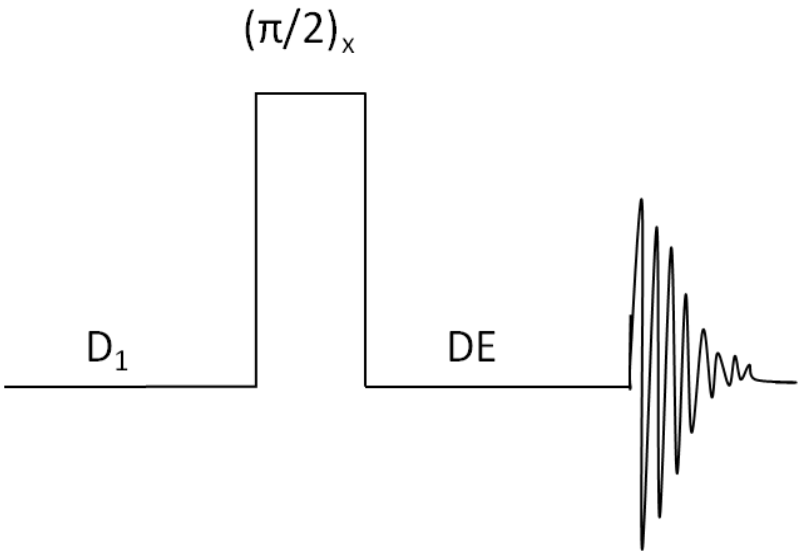

Figure 2.4.1: Single Pulse Sequence.

The recycle delay time D_1 (usually 5-10 times of T_1) should be chosen such that the magnetization relaxes fully to its equilibrium position, before another excitation pulse is applied. Relaxation is important as the NMR signal will evolve according to the initial conditions of the magnetization. If the magnetization is not allowed to relax to equilibrium before applying the RF pulse, signal saturation will progress as more pulses are applied. The dead time, DE, is the time between the end of the pulse and the beginning of acquisition of the FID. DE is usually 10 to 20 μs, as this is roughly the amount of time it takes for the receiver to recover after the applied RF pulse.

2.4.2. Inversion Recovery Pulse Sequence

Inversion recovery is a common technique to measure the spin lattice relaxation time T_1. T_1 is the characteristic time required for the spin to attain equilibrium with the surrounding lattice as previously discussed. The pulse sequence consists of two RF pulses, π_x and $(\pi/2)_x$ separated by a time delay (τ), as in figure 2.4.2.1.

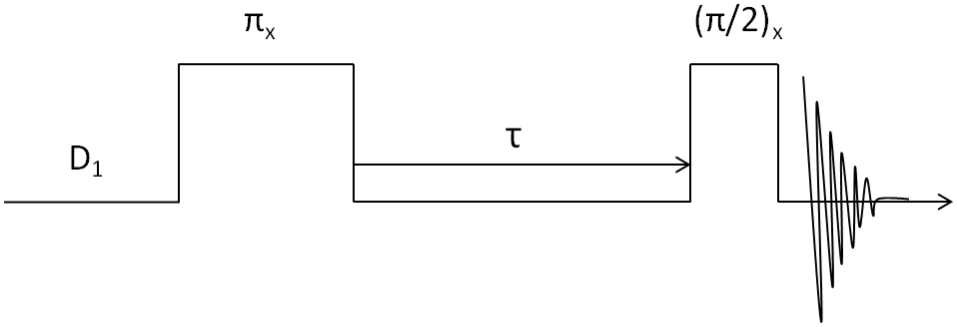

Figure 2.4.2.1: Inversion Recovery Pulse Sequence.

The use of single headed arrow in fig. 2.4.2.1 indicates that the pulse is repeated with different time intervals τ. The magnetization is inverted along -z axis after the π_x pulse. During the interval τ, the inverted magnetization partially or fully recovers as a function of τ along the +z -axis as the spins achieve thermal equilibrium. The recovering magnetization is

then detected by subjecting it to a second RF pulse $(\pi/2)_x$. At the end of the second pulse, free induction decay with amplitude in proportion to the amount recovered is recorded. The recovery for simple relaxation processes has an exponential dependence with time τ, and the spin-lattice relaxation time T_1 can be extracted. The expression describing the behavior as stipulated by the Bloch relation for initial ($M_z(0) = -M_0$) and final ($M_z(\infty) = M_0$) conditions becomes:

$$M_z(\tau) = M_0\left(1 - 2e^{-\frac{\tau}{T_1}}\right) \quad \text{..... (2.4.2)}$$

and the corresponding decay curve as:

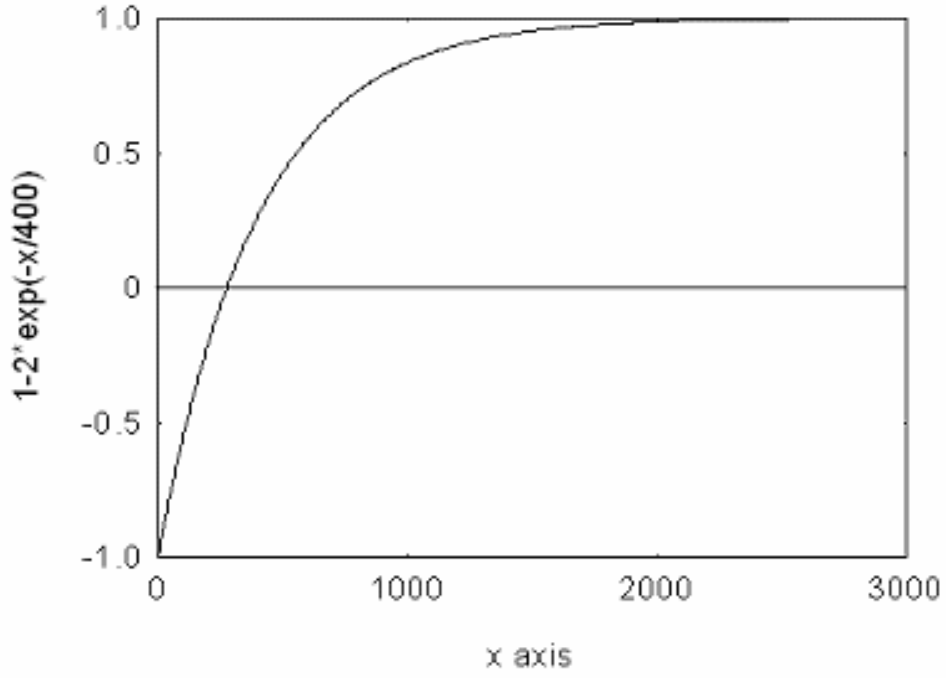

Figure 2.4.2.2: Decay profile of T_1 (M vs. τ).

2.4.3. Saturation Recovery Pulse Sequence

An alternative method to measure T_1 is called saturation recovery. In this technique, the magnetization is initially saturated ($M_z(0) = 0$) then is allowed to recover towards equilibrium. This pulse sequence is very useful if T_1 is long, since one does not have to wait for the spins to achieve thermal equilibrium between transients. The pulse sequence is shown in figure 2.4.3.1.

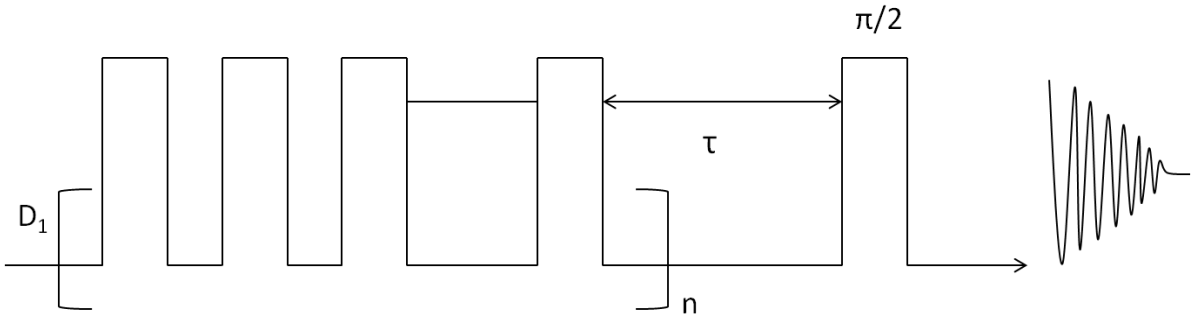

Figure 2.4.3.1: Saturation Recovery Pulse Sequence.

In the above figure, $[\ ]_n$ indicates the repetition of pulses (pulse train) needed in order to achieve the saturation condition. The pulse train is usually comprised of 10 to 100 high power $\pi/2$ pulses separated by a delay, which is typically much less than T_1 but greater than T_2. So, in this sequence, the recovered magnetization is monitored from the saturated state to the equilibrium state as a function of τ. Again, solving the Bloch relation with the initial condition $M_z(0) = 0$, yields an expression whereby T_1 can be extracted.

$$M_z(\tau) = M_0\left(1 - e^{-\frac{\tau}{T_1}}\right) \quad \text{..... (2.4.3)}$$

The corresponding decay curve as:

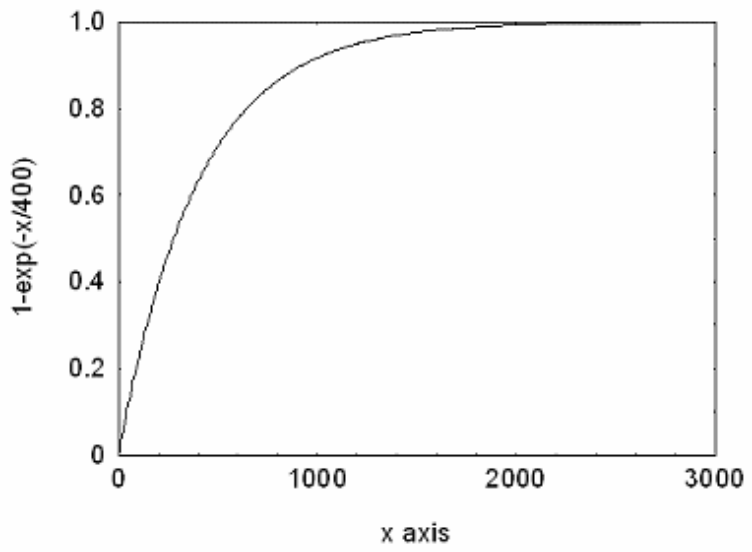

Figure 2.4.3.2: Decay profile of T_1 (M vs. τ).

2.4.4. Spin Echo Pulse Sequence

Spin Echo pulse sequence is used to study spin-spin relaxation and obtain T_2 but it has a variety of other spectroscopic applications as well. It consists of two RF pulses, π/2 and π respectively, separated by a delay τ as in the following figure.

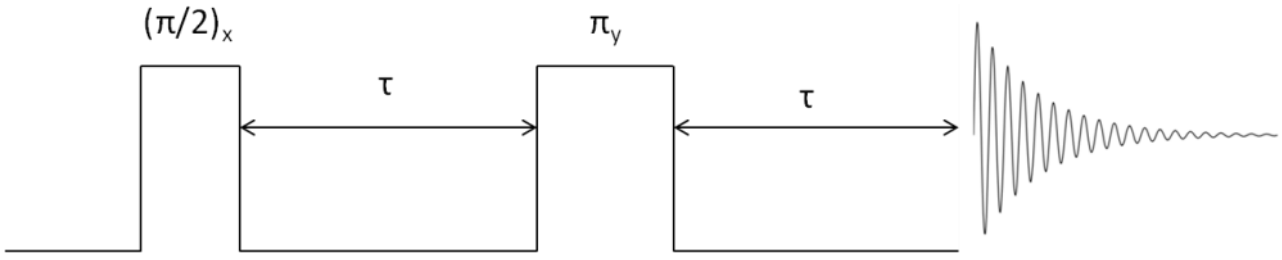

Figure 2.4.4: Spin Echo Pulse Sequence.

For example, the first π/2 pulse, if applied along the x-axis, will rotate the equilibrium magnetization from the +z-axis to the –y-axis. During the interval τ, magnetization from different spatial regions progressively decoheres or dephases due to field inhomogeneities. After the first interval τ, a second pulse of duration π is applied along the +y-axis which rotates the dephased magnetization by π around the +y-axis. During the second interval τ, the

magnetization refocuses and an echo is formed. With the proper initial and final conditions, the transverse Bloch relation can be solved. The magnetization varies exponentially as a function of τ and T_2 is determined according to the following equation.

$$M(2\tau) = M_0 e^{-\frac{2\tau}{T_2}} \quad \text{..... (2.4.4)}$$

2.5. NMR Diffusion

There are three different kinds of motion of molecules described as rotational, translational and internal motions. Internal molecular motions refer to vibrations of molecule, rotations of some internal molecular groups and chemical isomerizations. Molecular rotation involves a change in the orientation of each molecule in space. There are two essential types of molecular translational motion: diffusion and flow. Diffusion is the random motion of molecules and flow is the molecular motion that is biased in some particular direction by an external pressure gradient. There are also different types of diffusion referred to as self-diffusion and mutual diffusion.

Self-diffusion: Self-diffusion is the random thermal motion of molecules often referred to as Brownian motion without an applied force. In this case therefore, there is no net displacement as in fig 2.5.1. The unit of the self-diffusion coefficient is m^2/s.

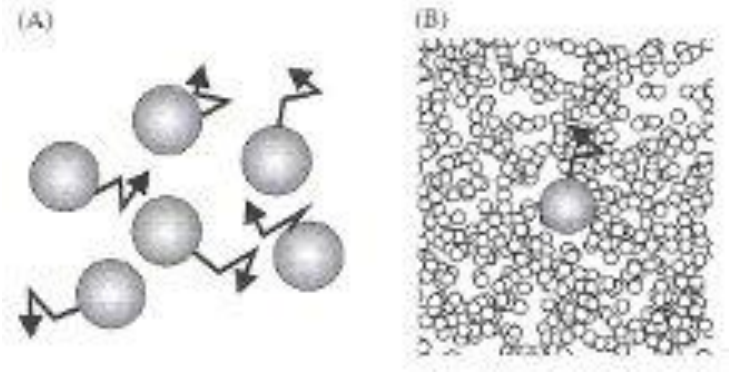

Figure 2.5.1: Random motion of molecules.

Mutual diffusion: Mutual diffusion is also known as interdiffusion or concentration diffusion. Concentration inhomogeneities of any component in a multicomponent system result in mass fluxes to average out the inhomogeneity to achieve thermodynamic equilibrium [19]. The driving force behind mutual diffusion is the gradient of the chemical potential. The unit of the mutual diffusion coefficient is the same as self-diffusion (m^2/s).

NMR diffusion measurement provides a direct means to determine self-diffusion coefficients. There are various NMR techniques to measure diffusion. The most common is the Pulse Field Gradient Spin Echo technique.

The intensity of the spin echo is dependent on the spin amplitude and corresponding phase. The Magnetization M(τ) at time τ after 180^o pulse can be obtained by averaging the individual contributions over all nuclei in the sample as [20]:

$$M(\tau) = \left\langle e^{+i\gamma\int_0^{\tau} dt'\omega_L(t')} \; e^{-i\gamma\int_{\tau}^{2\tau} dt'\omega_L(t')} \right\rangle \quad \text{..... (2.5.1)}$$

where the first term in the brackets corresponds to dephasing and the second term to rephasing. If there is molecular motion, the dephasing and rephasing periods do not exactly cancel at time 2τ and therefore the amplitude of the spin echo is reduced. τ can be expressed in terms of an arbitrary length δ and Δ in the PFG spin echo technique as shown in fig.2.5.3.

As the spin phase is dependent on γ, the gradient g and the position of the nuclei z, the phase of the field gradient spin echo can be written as [20]:

$$\Phi(t_e) = -\gamma \int_0^{t_e} dt' \tilde{g}(t') z(t') \quad \ldots\ldots\ldots\ldots\ldots\ldots \quad (2.5.2)$$

where t_e is the time of the echo maximum. The phase integral can be expanded through integration by parts as:

$$\Phi(t_e) = -\int_0^{t_e} \tilde{G}(t) v(t) dt \quad \ldots\ldots\ldots\ldots\ldots\ldots\ldots\ldots\ldots\ldots \quad (2.5.3)$$

where v(t) is the velocity of the nuclei and $G(t_e)=0$. And $\tilde{G}(t)$ is defined as:

$$\tilde{G}(t) = \gamma \int_0^{t} dt' \tilde{g}(t') \quad \ldots\ldots\ldots\ldots\ldots\ldots\ldots\ldots\ldots\ldots \quad (2.5.4)$$

The amplitude of the spin echo is the sum of the contributions of all N spins in the sample and can be written as:

$$M(t_e) = \sum_{k=1}^{N} e^{i\Phi_k(t_e)} = M_0 \left\langle e^{i\Phi_k(t_e)} \right\rangle \quad \ldots\ldots\ldots\ldots\ldots\ldots\ldots\ldots \quad (2.5.5)$$

which is described in equation 2.5.1. The second term of this equation can be simplified by cumulant expansion [20] as:

$$M(t_e) = M_0 \exp\left\{ i\langle \Phi_k(t_e) \rangle - \frac{1}{2}\left(\langle \Phi_k^2(t_e) \rangle - \langle \Phi_k(t_e) \rangle^2 \right) \pm ..... \right\} \quad \text{..... (2.5.6)}$$

If the motion of the spin is free and isotropic, then $\Phi(t_e)$ is expressed as a Gaussian distribution with 0 mean value [20]. Therefore, equation (2.5.5) can be written as:

$$M(t_e) = M_0 e^{-\frac{1}{2}\langle \Phi_k^2(t) \rangle} \quad \text{..... (2.5.7)}$$

Using equation (2.5.3) and averaging the echo amplitude with the velocity autocorrelation function, $M(t_e)$ can be written as:

$$M(t_e) = M_0 \exp\left\{ -\frac{1}{2}\int_0^{t_e} dt_1 \int_0^{t_e} dt_2 \tilde{G}(t_1)\tilde{G}(t_2) \times \langle v(t_1)v(t_2) \rangle \right\} \quad \text{..... (2.5.8)}$$

The self-diffusion coefficient in a homogeneous system is related to the root mean square displacement of the molecules as:

$$\left(\langle r^2 \rangle \right)^{\frac{1}{2}} = (2nDt_e)^{\frac{1}{2}} \quad \text{..... (2.5.9)}$$

where n is the number of dimension a particle can move, t_e is the diffusion time and D is the self-diffusion coefficient. Therefore, the velocity autocorrelation function can be expressed by a delta function assuming simple isotropic diffusion as:

$$\langle v(t_1)v(t_2) \rangle = 2D\delta(t_2 - t_1) \quad \text{..... (2.5.10)}$$

Using this, equation (2.4.5.8) can be written as:

$$M(t_e) = M_0 \exp\left\{-D\int_0^{t_e} dt_1 \tilde{G}^2(t_1)\right\} \quad \text{…………………………….. (2.5.11)}$$

Therefore, the echo intensity in the PFG Hahn echo (or Spin echo) sequence can be obtained by solving equation (2.5.11) as:

$$M(\delta,\Delta) = M_0 \exp\left(-\gamma^2 g^2 \delta^2 D\left(\Delta - \frac{1}{3}\delta\right)\right) \quad \text{………………….. (2.5.12)}$$

The pulse sequence corresponding to the above equation is:

$$g`(t`)=\{\,g\,;\quad (t_1 < t < t_1+\delta) < \tau \quad \text{and } (t_1+\Delta < t < t_1+\Delta+\delta) < 2\tau\,\}$$

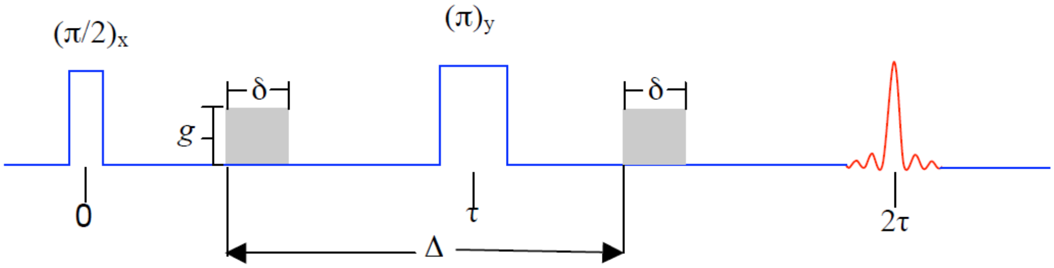

Figure 2.5.2: Pulse field gradient Spin echo (PFGSE) sequence.

Self-diffusion coefficients of molecules, atoms and ions can be obtained from spin echo experiments with the application of magnetic field gradient pulses. The PFGSE sequence accomplishes this, as it consists of two RF pulses separated by τ and two gradient pulses separated by Δ as shown in figure 2.5.2. The central idea is that any particle motion within the 2τ period will be encoded as diminishing echo intensity with increasing applied gradient strength. Other parameters that need to be specified are: δ - the gradient pulse

duration, and d1- the recycle delay. In practice, the parameters δ, Δ and τ are usually kept fixed while the gradient strength is varied. The magnetization echo intensity is monitored as a function of gradient strength as shown in figure 2.5.3.

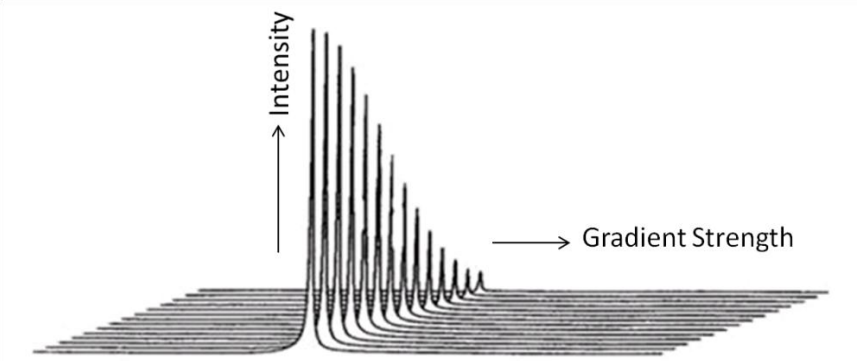

Figure 2.5.3: NMR diffusion profile using PFGSE pulse sequence.

Accordingly, the self-diffusion coefficient is extracted from plots of the integrated NMR echo signal (A(g,2τ)) and via the Stejskal and Tanner equation:

$$A(g,2\tau) = A(0,0)\exp\left[-\gamma^2 g^2 D\delta^2\left(\Delta - \frac{\delta}{3}\right)\right] \quad \ldots\ldots\ldots\ldots\ldots\ldots\ldots\ldots\ldots\ldots \quad (2.4.5)$$

A(0, 0) is the initial echo amplitude, γ the magnetogyric ratio and D is the self-diffusion coefficient.

Chapter 3

3. Spin diffusion measurements of Gel type Polymers based on Py_{24}TFSI Ionic Liquid (IL) using NMR techniques

This project has been done in collaboration with Dr. Maria A. Navarra at University of Rome.

3.1. Introduction

Safety and environmental issues are now two major concerns to commercialize Lithium ion Batteries. The applications of Li-ion batteries are mainly for the portable electronic devices such as laptop computers, cell phones, digital cameras and also for hybrid electric vehicles. Safety hazards can be reduced by considering the replacement of conventional, volatile, flammable organic alkyl carbonate electrolytes with highly stable ionic liquids (ILs). ILs are low temperature molten salts as described in Chapter 1 in section 1.6. The most common example of ILs are those composed of EMI (1-ethyl-3-methyl-imidazolium) or Py (1-methyl-1-butyl-pyrrolidinium) cations with delocalized anion such as TFSI (trifluoromethane sulfonyl amide). These ionic combinations give a good range of ion conductivity which is comparable to many organic electrolyte solutions and an absence of decomposition or significant vapor pressure up to ~ 300 to 400^{o}C [5]. The IL described in this chapter is the combination of Pyrrolidinium cation with TFSI anion as shown in fig. 3.1.

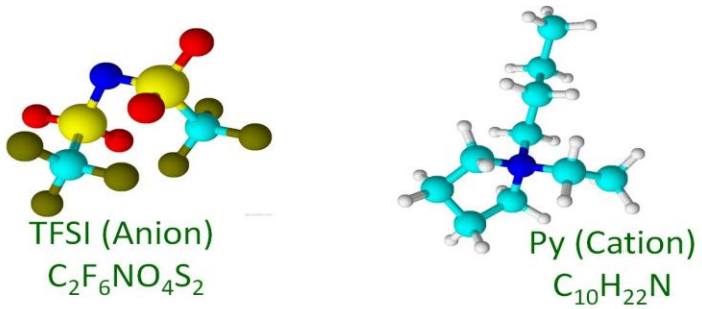

Figure 3.1: Structure of IL with TFSI anion and Py_{24} cation.

To provide the electroactive species for the cell reactions, a proper lithium salt must be dissolved in IL, which results in an increased viscosity, enhanced ion-ion interactions and reduced the conductivity with respect to the pure IL. As LiTFSI salt was added in the ionic liquids (described in this thesis), the salt makes the ILs viscous and therefore reduces the diffusion coefficients. The organic solvents ethylene carbonate (EC), propylene carbonate (PC) and dimethyl carbonate (DMC) were added to the IL and salt mixtures. The inclusion of organic solvents in the mixture offers advantages of a) the high dielectric constant of both EC and PC that enhances the lithium-anion interactions, b) passivating film forming ability of EC that optimizes the interfacial behavior, c) low viscosity of DMC enhances ion transport, d) widens the temperature range of high ionic conductivity when these three solvents are added to a thermally stable ionic liquid [1].The performance of the lithium battery also depends on the stability of the IL electrolyte towards the electrode components. Py_{24}TFSI (N-n-butyl-N-ethyl-pyrrolidinium N,N bis(trifluoromethanesulfonyl) imide) ionic liquid has improved cathodic stability without reducing its ionic conductivity which can be used for safe and reliable battery design [6].

Much research is aimed toward making polymer electrolytes suitable for commercial large format Li-ion batteries. The main problems of using polymer electrolytes are the low conductivity at ambient temperature and reactivity with the lithium metal electrode. The combination of polymer matrix and ionic liquid offers mechanical and chemical stability as ionic liquids have favorable properties (described in chapter 1). In this chapter, NMR studies of new types of electrolytes based on Py_{24}TFSI ionic liquid, poly(vinylidenefluoride-co-hexafluoropropylene) (PVDF-HFP) and mixtures of organic solvents such as ethylene, propylene and dimethyl carbonates (EC-PC-DMC) are presented. In order to study the ionic transport, pulsed field gradient spin echo technique was performed in order to obtain self-diffusion coefficients of both gel-type and liquid electrolytes. Spin – lattice relaxation times were also measured.

3.2. Experimental

3.2.1. Preparation of Sample

The preparation of the sample was performed at the University of Rome.

The N-n-butyl-N-ethyl-pyrrolidinium N,N-bis(trifluoromethanesulfonyl)imide Py_{24}TFSI was prepared according to a synthetic route previously established [6]:

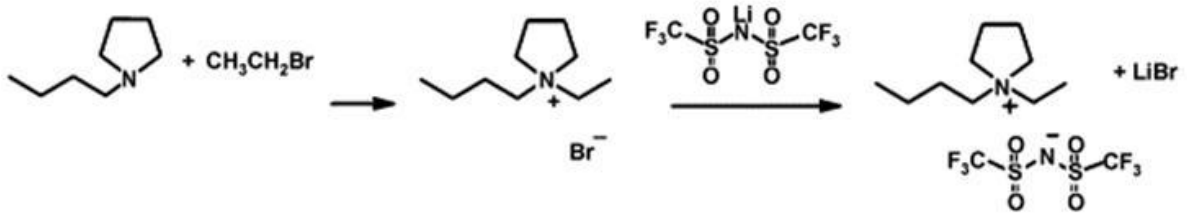

Figure 3.2: Procedure of Synthesizing Py_{24}TFSI IL.

For this synthesis, 1-butylpyrrolidine and 1-bromoethane were mixed in ethylacetate and the resulting solution was stirred at 50°C for 2 days. The solvent was evaporated, leaving a solid product ($Py_{24}Br$), which was then purified by recrystallization in a suitable mixture of ethylacetate and ethanol. The anion-exchange was obtained by adding drop by drop an aqueous solution of LiTFSI to the bromide precursor, following subsequent extractions of the organic phase. Purification of the synthesized IL was assured by treatments with activated carbon and alumina. The liquid obtained was finally dried under vacuum at 80 °C. The Purity of $Py_{24}Br$ was confirmed by differential scanning calorimetry (DSC 821 Mettler-Toledo). The water content of the ionic liquid was revealed to be less than 20 ppm according to the standard Karl Fischer titration method (Metrohm KF 831 Coulometer) [1]. LiTFSI salt was added to the ionic liquid ($Py_{24}TFSI$) with a concentration of 0.2 $molKg^{-1}$ to provide conducting Li^+ ions.

The polymer gel electrolyte membranes were prepared by a solution casting procedure [1]. First, PVdF-HFP (Kynar Flex 2801) was dissolved in acetonitrile. Thereafter, LiTFSI-$Py_{24}TFSI$, or the mixture of the IL-salt solution and the alkyl carbonates, was added to the PVdF-HFP acetonitrile solution. Weight ratio of EC:PC:DMC was selected as 1:1:2. The resulting solution was vigorously stirred overnight at room temperature and then cast in a Petri dish by heating at 70 °C and rapidly cooling down to room temperature. The heating-quenching process was repeated until free-standing membranes were obtained; the membranes were finally vacuum dried at 60 °C.

NMR investigation was performed on 7 samples having different composition, as reported below:

- Pure ionic liquid ($Py_{24}TFSI$),
- $Py_{24}TFSI$-LiTFSI solution (0.2 $molKg^{-1}$),
- $Py_{24}TFSI$-LiTFSI solution/EC:PC:DMC (80/20 w/w%),
- $Py_{24}TFSI$-LiTFSI solution/EC:PC:DMC (64/36 w/w%),
- PVDF-HFP / $Py_{24}TFSI$-LiTFSI solution (30/70 w/w%),
- PVDF-HFP / $Py_{24}TFSI$-LiTFSI solution / EC:PC:DMC (30/56/14 wt%),
- PVDF-HFP / $Py_{24}TFSI$-LiTFSI solution / EC:PC:DMC (22/50/28).

The preparation and handling of materials were carried in an argon filled glove box.

3.2.2. NMR Studies of Ionic Liquids

NMR measurements were performed on a Varian Direct Drive 300 MHz spectrometer (i.e field strength of 7.1 T) using a Doty diffusion probe. Three nuclei ^{1}H, ^{19}F, and ^{7}Li were selected to study the ion transport of the liquid and polymer electrolytes based on $Py_{24}TFSI$ IL. The operating frequencies were 301.40 MHz for ^{1}H, 283.53 MHz for ^{19}F and 117.13 MHz for ^{7}Li. Spectroscopic references were TMS (tetramethysilane) for ^{1}H, LiTf (an aqueous solution of lithium triflate) for ^{19}F and an aqueous solution of LiCl (lithium chloride) for ^{7}Li. Pulse widths were about 21μs for ^{1}H, 20μs for ^{19}F and 7μs for ^{7}Li. Self diffusion coefficients were obtained for all three nuclei using the pulsed field gradient spin echo (PFGSE) sequence. Spin lattice relaxation times T_1 were obtained for all three nuclei using the inversion recovery pulse sequence. $Py_{24}TFSI$-LiTFSI solution / EC:PC:DMC (64/36) and PVDF – HFP / $Py_{24}TFSI$-LiTFSI solution / EC:PC:DMC (22/50/28) samples

were chosen for the variable temperature NMR measurements. Self-diffusion coefficients and T_1 measurements were obtained for these two samples at temperatures 25°C, 30°C, 40°C, 50°C, 60°C and 70°C for all three nuclei (^{1}H, ^{19}F and ^{7}Li). The decay curve for the signal intensity vs. gradient values (^{7}Li) is shown in figure 3.3, fitted to the Stejskal Tanner equation (equ. 3.1).

$$A(g) = A(0)\exp\left[-D\gamma^2 g^2 \delta^2 \left(\Delta - \frac{\delta}{3}\right)\right] \quad \ldots\ldots\ldots\ldots\ldots\ldots\ldots\ldots\ldots\ldots \quad (3.1)$$

This equation is described in chapter 2 in section 2.5.

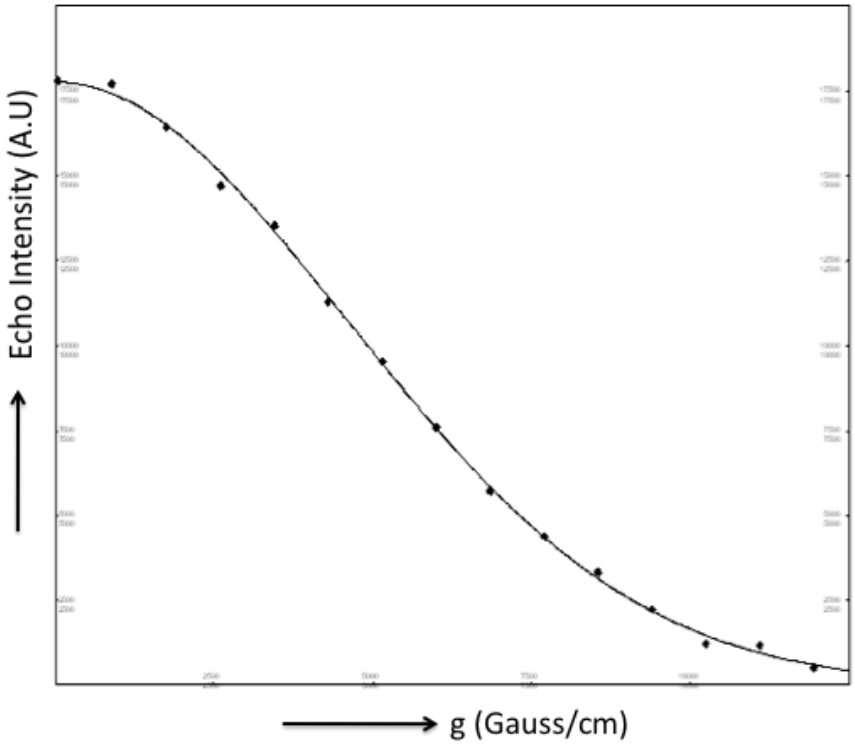

Figure 3.3: Diffusion profile (^{7}Li) of Py_{24}TFSI ionic liquid in peakfit software.

The NMR spectra of Py_{24}TFSI-LiTFSI solution / EC:PC:DMC (64/36) and PVDF – HFP / Py_{24}TFSI-LiTFSI solution / EC:PC:DMC (22/50/28) for three nuclei at 25°C are shown in figure 3.4 and figure 3.5.

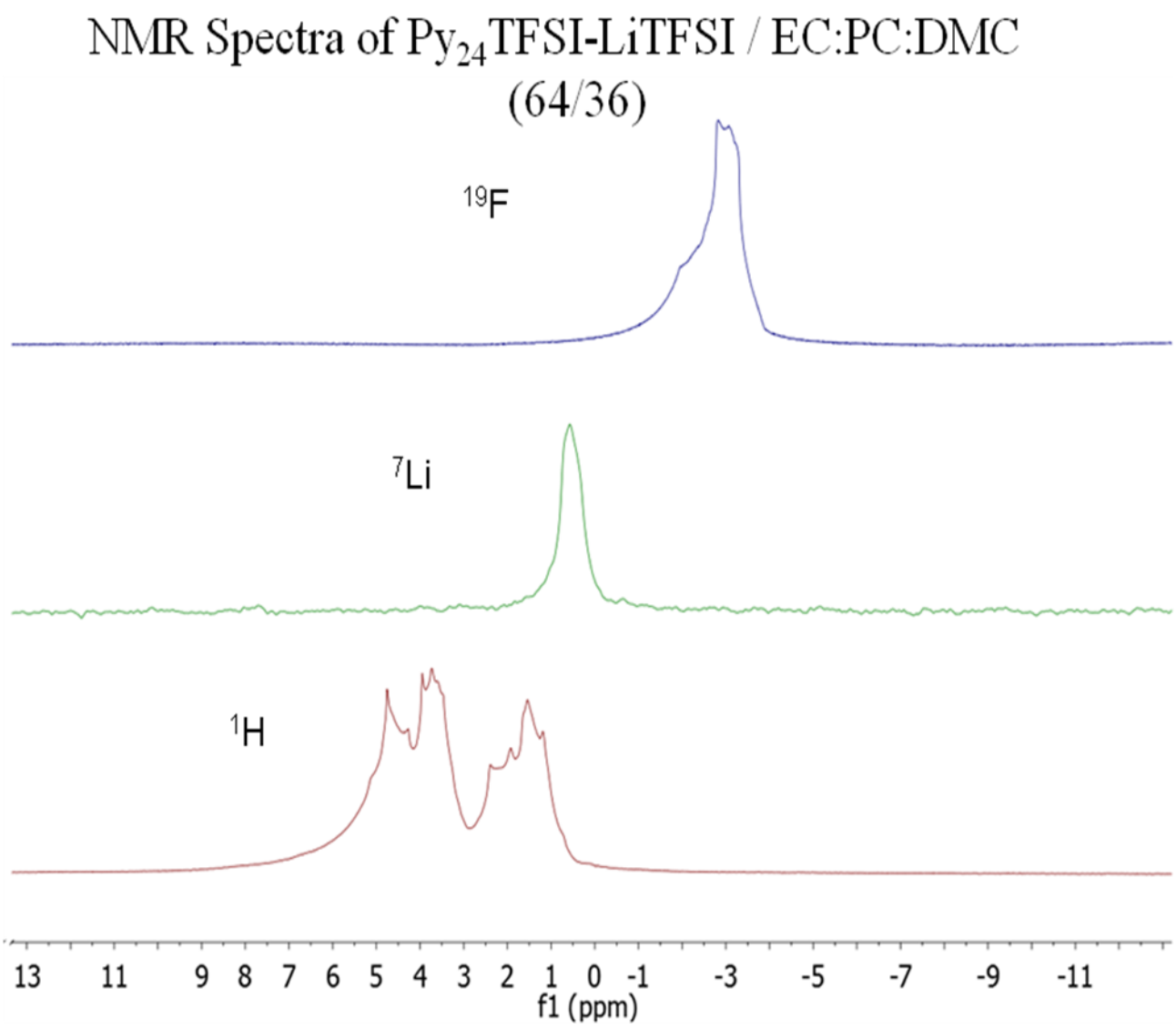

Figure 3.4: NMR Spectra of ^{1}H, ^{7}Li, ^{19}F for $Py_{24}TFSI$-LiTFSI/EC:PC:DMC (64/36).

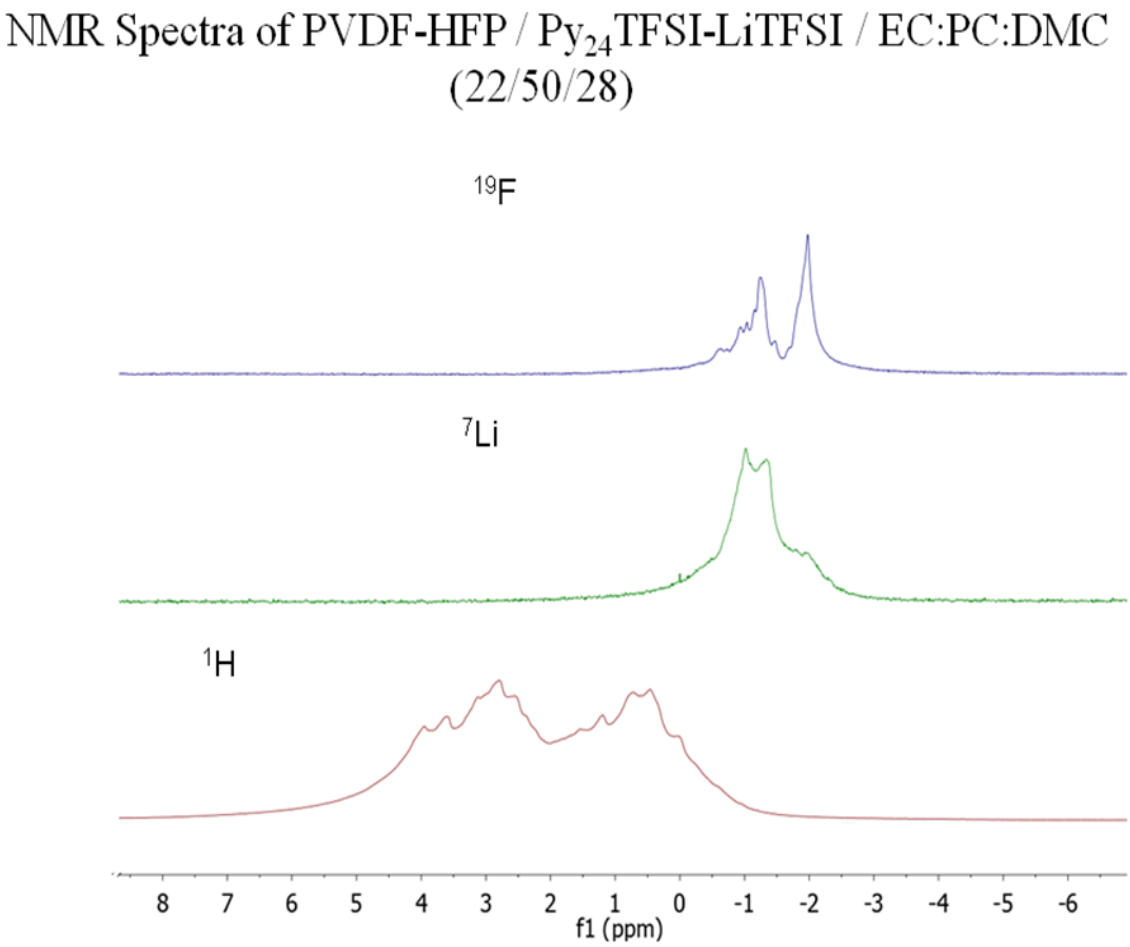

Figure 3.5: NMR Spectra of ^{1}H, ^{7}Li, ^{19}F for PVDF-HFP/Py_{24}TFSI-LiTFSI/EC:PC:DMC (22/50/28).

3.3. Results and Discussion

The NMR studies were to investigate self diffusion coefficients of composite ion-conducting materials based on a polymer (PVDF-HFP), an ionic liquid (Py_{24}TFSI), a salt (LiTFSI) and mixtures of organic solvents (EC:PC:DMC). To study the effect of each component on the properties of the final electrolyte, samples with different composition were analysed. Three membrane compositions were considered on the basis of the results of previous electrochemical studies [1]. For a comprehensive and comparative investigation,

liquid electrolytes formed by IL, LiTFSI salt and alkyl carbonates in the same ratio as in the polymer membranes were also analysed.

NMR spectra show that there are multiple peaks for all three nuclei as in fig 3.5. The multiple peaks in ^{1}H spectra are for the carbonate mixture as shown in fig. 3.4 and 3.5. The multiple peaks in ^{19}F, which is shown in figure 3.5, are from PVDF-HFP gel and the IL. ^{7}Li spectra in fig. 3.5 also show multiple peaks, which suggests the coexistence of different Li^{+} solvation environments.

The impact of adding carbonates to IL-salt mixtures and polymer matrix are shown in table 3.1. The samples are labelled S1, S2, S3, S4, S5, S6 and S7. It is clear from the table that adding the salt reduces the diffusion coefficients to almost half that of the pure ionic liquid (compare S1 and S2). The diffusion coefficient is higher for S3 when 20 wt% carbonate solvents are added to the IL solution. S4 has the diffusion coefficients twice than the S3 as 36 wt% alkyl carbonate is in the IL. Similarly for the polymer matrix, S7 has the highest diffusion coefficient, probably due to the percentage of alkyl carbonate is higher than S6. S5 has almost the same diffusion coefficients as S2. The diffusion coefficient of ^{1}H is always higher than ^{19}F and ^{7}Li except for S7.

Comparing the self-diffusion coefficients of ^{19}F and ^{7}Li for all ILs, ^{7}Li self diffusion coefficient for S2 (without alkyl carbonate) is half that of the ^{19}F but this ratio is reduced for S3 and S4 (with alkyl carbonate). Adding carbonates to the membranes also increases ionic diffusivity.

Table 3.1: Self diffusion coefficients for the ILs with nuclei ^{1}H, ^{19}F and ^{7}Li.

Sample Name	Sample Content	Nucleus	Self – Diffusion Coefficients D ($\times 10^{-11} m^2/s$)
S1	Py_{24}TFSI	1H 19F	1.3 1.3
S2	Py_{24}TFSI-LiTFSI, 0.2M	1H 19F 7Li	0.7 0.8 0.4
S3	Py_{24}TFSI-LiTFSI+EC:PC:DMC(80:20)	1H 19F 7Li	7.4 5.2 3.5
S4	Py_{24}TFSI-LiTFSI+EC:PC:DMC(64:36)	1H 19F 7Li	16.2 12.8 8.1
S5	PVDF-HFP+Py_{24}TFSI-LiTFSI(30:70)	1H 19F 7Li	0.5 0.4 0.5
S6	PVDF-HFP+Py_{24}TFSI-LiTFSI+EC:PC:DMC(30:56:14)	1H 19F 7Li	1.5 1.0 1.1
S7	PVDF-HFP+Py_{24}TFSI-LiTFSI+EC:PC:DMC(22:50:28)	1H 19F 7Li	4.9 5.7 3.5

Samples, S4 and S7 were selected for variable temperature diffusion and T_1 measurements. Fig. 3.6 shows the diffusion of three nuclei (^{1}H, ^{19}F and ^{7}Li) for S4 sample. The diffusion coefficients are higher for ^{1}H than ^{19}F and ^{7}Li. Unfortunately, the spectra of ^{1}H nuclei for all of the IL and carbonate constituents are characterized by severe overlap, therefore it is hard to separate the peak for the cation from the carbonate solution. The comparisons are shown in figure 3.7 for the peaks of cation and carbonate solution for IL with carbonate mixture and polymer matrix with IL and carbonate mixtures. The diffusion

coefficients are thus an average of the IL and solvent molecules. At higher temperatures the diffusion coefficients of ^{7}Li is almost same as ^{19}F.

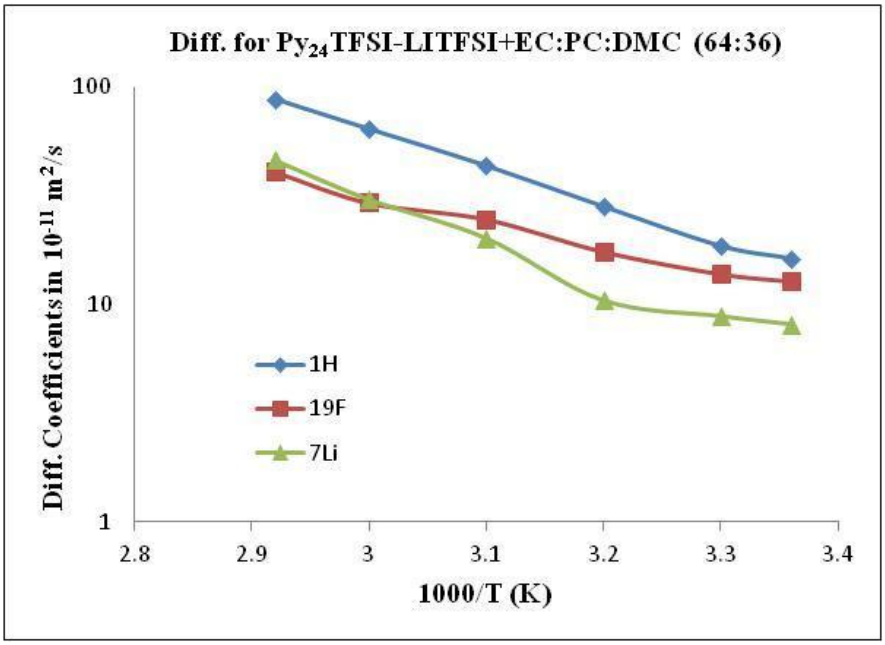

Figure 3.6: Diffusion curve of Py_{24}TFSI-LiTFSI with EC:PC:DMC (S4) for ^{1}H, ^{19}F and ^{7}Li.

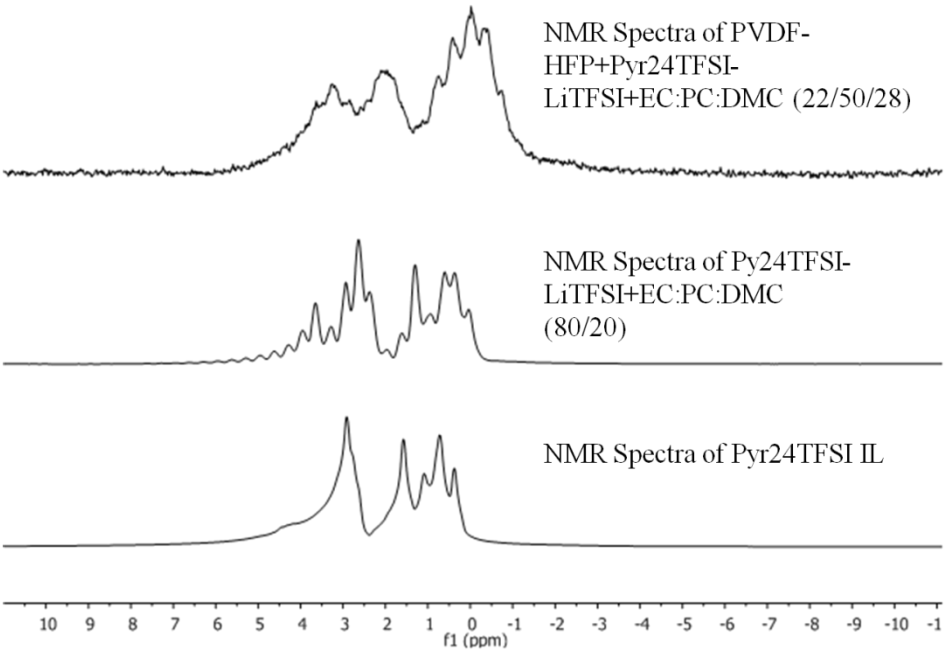

Figure 3.7: The comparison of ^{1}H NMR Spectra for three samples pure IL (S1), IL with carbonate mixture (S3) and polymer with IL and carbonate mixture (S7).

The diffusion curve of S7 sample at variable temperature for nuclei ^{1}H, ^{19}F and ^{7}Li is shown in fig. 3.8. The ^{19}F diffusion coefficients are higher in S7 sample than ^{1}H and ^{7}Li which is different in variable temperature (VT) data for S4 (without Polymer matrix) as in fig 3.6. Although ^{1}H self-diffusion coefficient is the average of self-diffusion coefficients from polymer, cation and alkyl carbonate, ^{7}Li self-diffusion coefficient is almost same as ^{1}H at all temperatures.

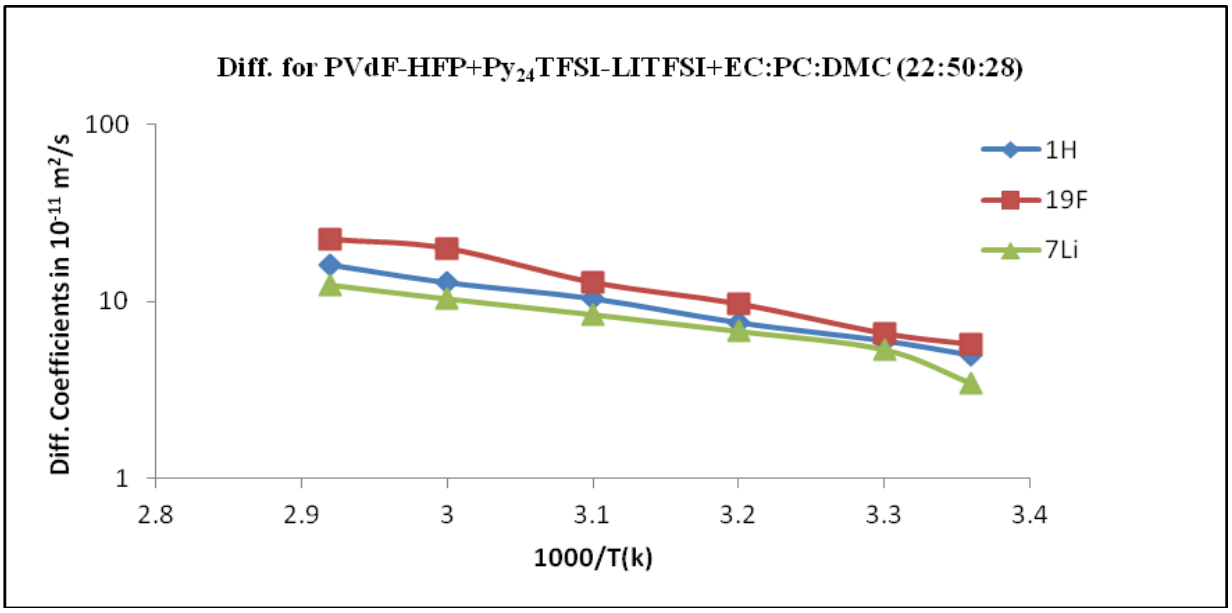

Figure 3.8: Diffusion curve of PVDF-HFP with Py_{24}TFSI-LiTFSI and EC:PC:DMC (S7) for ^{1}H, ^{19}F and ^{7}Li as a function of temperature.

The variable temperature spin-lattice relaxation times T_1 for samples S4 and S7 are shown in figure 3.9 and 3.10. The value of T_1 increases with increasing temperature for both samples S4 and S7. The T_1 plot for all three species (^{1}H, ^{19}F and ^{7}Li) do not show the T_1-minimum that occurs if the molecular correlation time is equal to the reciprocal of 2π times the NMR frequency, which presumably would be observed at a lower temperature [7]. The relaxation time of ^{1}H in sample S4 is shorter than that for ^{19}F and ^{7}Li. ^{19}F has the higher T_1 values for both S4 and S7. At higher temperature 70^{o}C, T_1 is same for ^{1}H and ^{7}Li in S4,

which is also noticeable in the variable temperatures (VT) diffusion measurements. The relaxation times of ^{1}H and ^{7}Li are almost same for S7 at all temperature as is the case for the diffusion measurements. The overall T_1 values are higher in S4 than S7 for all three species due to restricted motion from the membrane-salt interaction. At temperature 50^{o}C, T_1 exhibits a maximum for ^{19}F in sample S7 compared to other temperature.

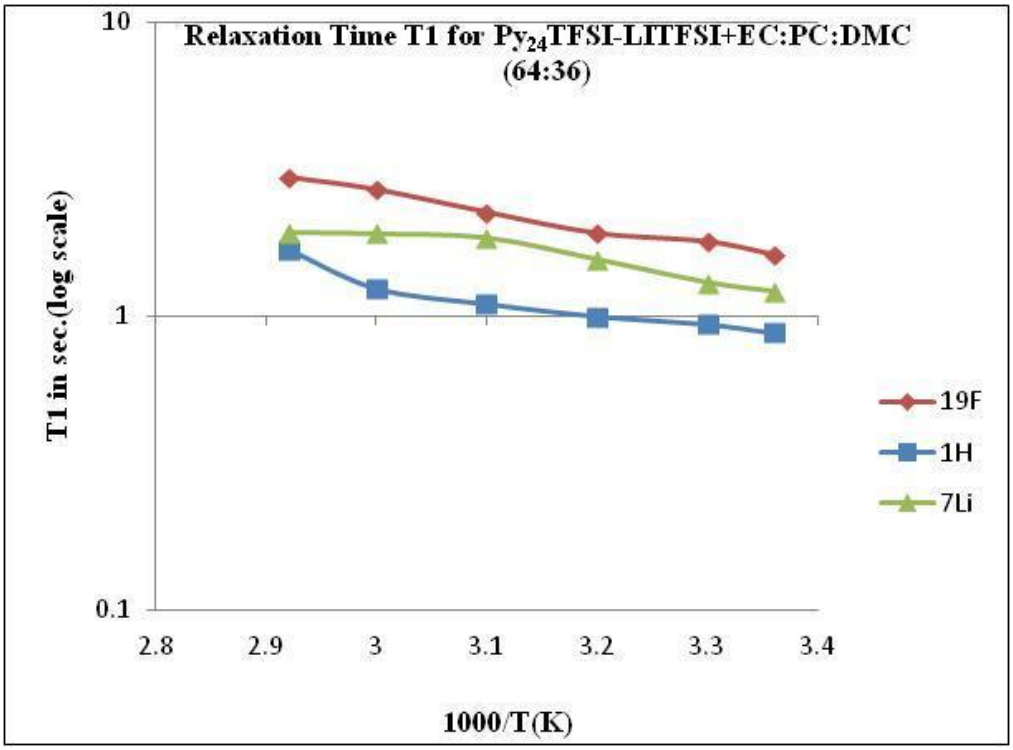

Figure 3.9: Arrhenius plot of T_1 as a function of temperature of Py_{24}TFSI-LiTFSI with EC:PC:DMC (S4).

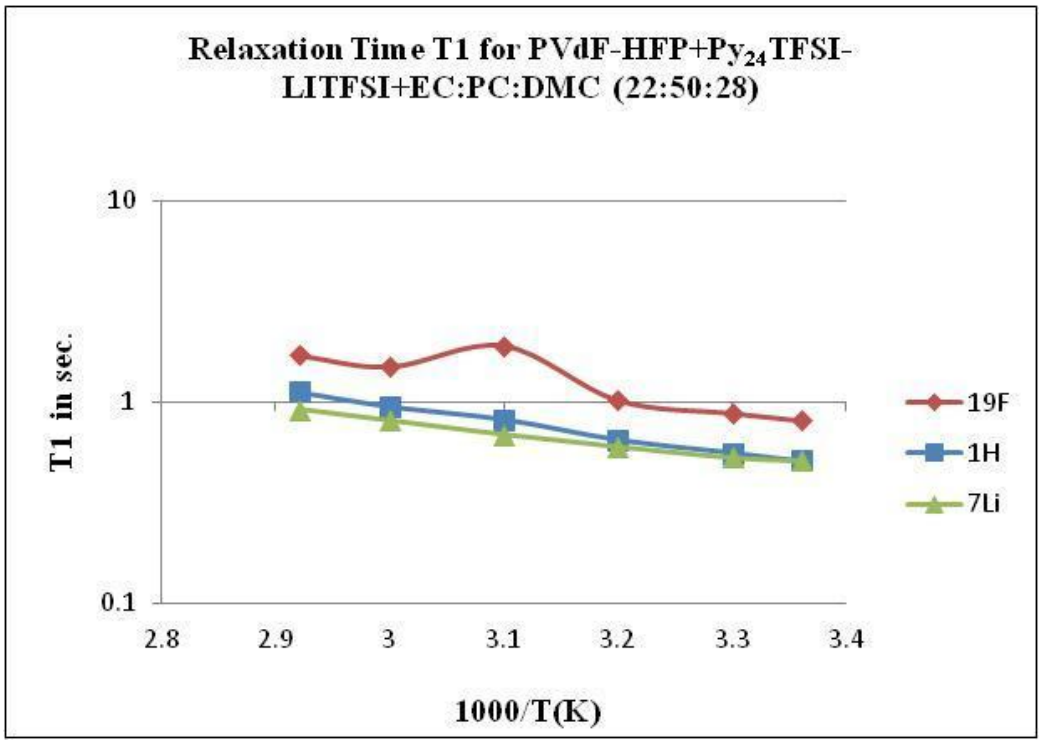

Figure 3.10: Arrhenius plot of T_1 as a function of temperature of PVDF-HFP with Py_{24}TFSI-LiTFSI and EC:PC:DMC (S7).

3.4. Summary

The results from NMR experiments confirmed that alkyl carbonate in IL-salt mixtures and membrane-IL-salts enhances the self-diffusion coefficients. Spin-lattice relaxation time also supports the diffusion measurements. Spin-lattice relaxation (T_1) measurements reflect mostly short-range molecular motions and the consistently higher T_1 values for ^{19}F are attributed to rotation of the CF_3 groups. The measured self-diffusion coefficient and previous results[1] show that the S7 sample can be a good choice of electrolyte for future lithium batteries.

3.5. Acknowledgement

This project is supported in part by grants from the U.S. Department of Energy and the Italian Ministry of University Research.

Chapter 4

4. ^{13}C NMR PFGSE measurements on Fluorine free Ionic Liquids

This work has been performed in collaboration with Dr. Wesley Henderson at North Carolina State University, Dr. Patrick Judeinstein at Institute de Chimie Moleculaire et des Materiaux d'Orsay, University Paris-Sud and Dr. Michel Armand at University de Picardie Jules Verne.

4.1. Introduction

Ionic liquids (ILs) are now considered very promising electrolytes for electrochemical devices due to their unique properties such as non-flammability, high thermal stability, low vapor pressure, tunable polarity as solvents and high conductivity. The most common classic ILs, that are formed by the combination of imidazolium (EMI^+) based cations as 1-ethyl-3-methyl-EMI^+ and delocalized charge anions as bis(trifluoromethanesulfonyl)imide ($TFSI^-$) which is very bulky and possesses extensive charge delocalization and conformational flexibility due to the facile rotation around S-N-S bonds. ILs with imidazolium or pyrolidinium cations and $TFSI^-$ anion are non-flammable and thermally stable, but if the battery is exposed to external fire, it can reach temperatures triggering extremely exothermic reaction of the positive electrode on the aluminium current collector and releases huge amounts of highly toxic HF. Also perfluorinated species are expensive, a drawback to commercialization. The fluorine free anions as DCTA (dicyanotriazole), DCA (dicyanomide), and TCM (tricyanomethanide) which are azacarbons, can be use instead of $TFSI^-$ and related anions. These azacarbons anions are flat in shape and have stabilized charge. The structures of anions are as in fig 4.1.

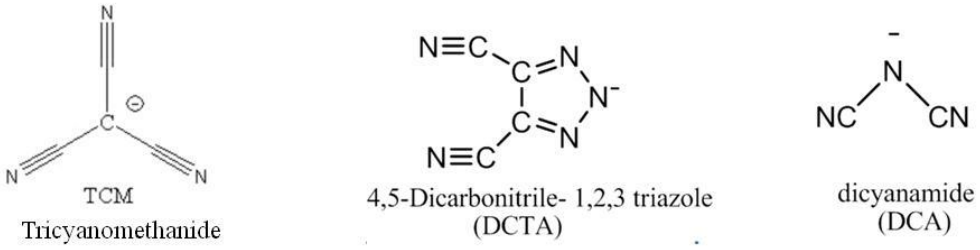

Figure 4.1: The Structure of Non-Fluorinated Anions TCM, DCTA and DCA.

NMR pulse field gradient technique is the only way to directly measure self-diffusion coefficients of molecules and ions in ILs. The fluorine free anions depicted above contain the nuclei carbon and nitrogen. Thus, ^{13}C and ^{15}N are the nuclei to perform NMR diffusion experiments on the anions. ^{15}N NMR diffusion experiment on these ILs has proven unsuccessful due to the poor NMR properties such as low γ and long relaxation time of this nucleus. Therefore, ^{13}C measurements were undertaken. The ^{13}C NMR diffusion experiment is challenging because it has natural abundance of 1.1% and also low γ (1/4 of ^{1}H). The NMR diffusion studies on ^{13}C and ^{1}H nuclei of these ILs are presented in this chapter.

4.2. Experimental

4.2.1. Ionic Liquids Preparation

Ionic Liquids are sythesized at Prof. Wesley Henderson's lab at the North Carolina State University.

Commercial Sodium dicyanamide $NaN(CN)_2$ was purified from NaCl impurity by dissolution in DMF, filtration and precipitation in CH_2Cl_2. Lithium tricyanomethane $LiC(CN)_3$ was transformed into the potassium salt by addition of excess KF in methanol, evaporation and extraction of $KC(CN)_3$ in acetonitrile, followed by recrystalization in hexane/acetonitrile (50/50 v:v). $Py_{13}Br$ and $Py_{14}Br$ were prepared from equimolar amounts of

N-methylpyrrolidine and 1-bromopropane or 1-bromobutane with a small amount of acetonitrile. HDCTA was synthesized by reacting diaminomaleonitrile and tert-butyl nitrile (10 mol% excess) in diethyl ether at 0^{o}C. The solution was centrifuged to remove impurities. DCA based ILs were prepared by reacting equimolar quantities EMIMCl, $Py_{13}Br$ or $Py_{14}Br$ with AgN(CN) in acetonitrile. TCM based ILs were prepared by reacting equimolar quantities of $Py_{13}Br$ with $KC(CN)_3$ in acetonitrile. The ILs were stored in hermitically sealed bottles in the glove box.

4.2.2. NMR Experiments

NMR diffusion measurements were performed with a Varian Direct Digital Drive 300 MHz spectrometer (B_0 = 7.1 T) with a Doty dual frequency z-gradient water cooled diffusion probe. Self-Diffusion coefficients were measured for the ^{1}H and ^{13}C nuclei, respectively at 300.1 MHz and 75.5 MHz. $\pi/2$ pulses were 21 μs for ^{1}H and 18 μs for ^{13}C nuclei. Tetramethylsilane (TMS) was used as a reference for both nuclei. The sample temperature was controlled with ± 0.5^{o}C accuracy.

Pulsed Field Gradient Spin Echo sequence (PFGSE) was used to obtain self-diffusion coefficients for both ^{1}H and ^{13}C nuclei. The values of self-diffusion coefficients were extracted from the classical Stejkal and Tanner equation (described in chapter 2 section 2.5) as:

$$A(g) = A(0)\exp\left[-D\gamma^2 g^2 \delta^2 \left(\Delta - \frac{\delta}{3}\right)\right] \quad \text{..... (4.1)}$$

The gradient pulse duration δ was fixed to 1.5 ms for ^{1}H and 4 ms for ^{13}C, its strength was varied from 50 G/cm to 600 G/cm in 15 steps, Δ was fixed to 100 ms for both nuclei. ^{13}C spectra were recorded without ^{1}H decoupling, and 32 free induction decays (FIDs) were

needed to get a reasonable S/N ratio; recovery delay was 30 seconds, which allowed determination of the full set of measurements to get a diffusion coefficient in 4.5 hours at 60^{o}C, but 13 hours at 25^{o}C as 100 FIDs were needed to get good S/N ratio. Spectra were recorded with 4K data points and zerofilled to 16K to improve digital resolution. An exponential filter of 7Hz was applied to the FID. For ^{1}H, 8 FIDs were added, and recovery delay of 15 seconds was used at both temperatures (25^{o}C & 60^{o}C).

In order to increase accuracy and reduce S/N, integration was performed separately on each component of the spectra multiplet and the corresponding components were added together {a+b+c+e+d+f} for the cation side and {g+h} for the anion side as in fig. 4.4. The peak fit software was used to fit the diffusion curve using eq. (4.1) as presented in figure 4.2.

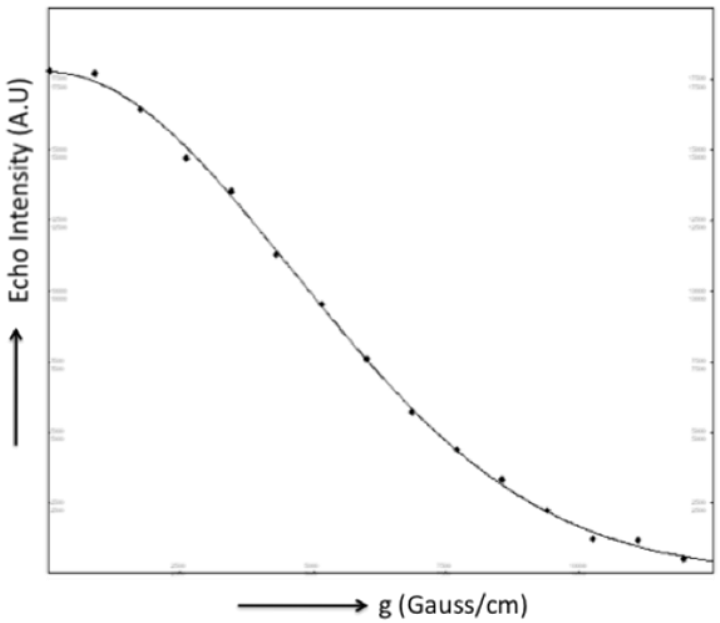

Figure 4.2: ^{13}C NMR Diffusion profile using Stejskal-Tanner equation in peakfit sotware.

4.3. Result and Discussion

There are eight combinations of cation and anion of fluorine free ILs were chosen for NMR studies such as EMIMDCTA, BMIMDCTA, Pyr_{13}DCTA, Pyr_{14}DCTA, Pyr_{13}TCM, EMIMDCA, Pyr_{13}DCA and Pyr_{14}DCA. The abbreviations EMIM, BMIM, Pyr_{13} and Pyr_{14} represent 1-ethyl-3-methylimidazolium, 1-butyl-3-methyimmidazolium, 1-methyl-1-propylpyrrolidinium and 1-methyl-1-butylpyrrolidinium. The structures of the cation are shown in fig. 4.3.

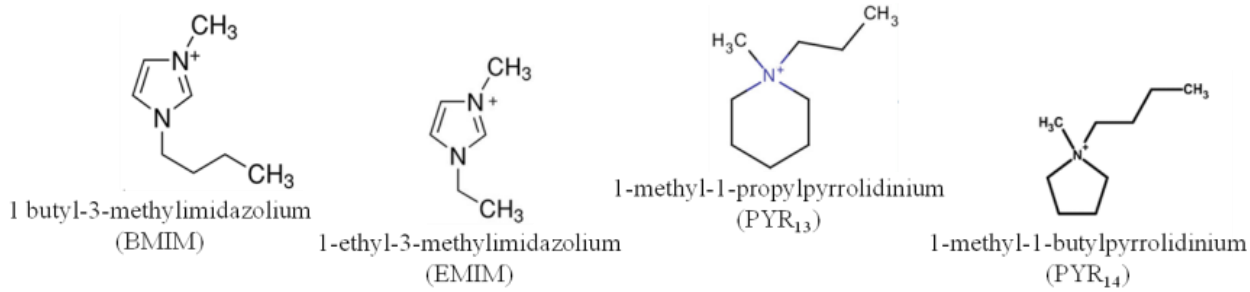

Figure 4.3: Structure of Cation for Fluorine free ILs.

4.3.1. NMR Spectra

^{13}C and ^{1}H NMR spectra of EMIMDCTA IL are shown in figure 4.4 and 4.5.

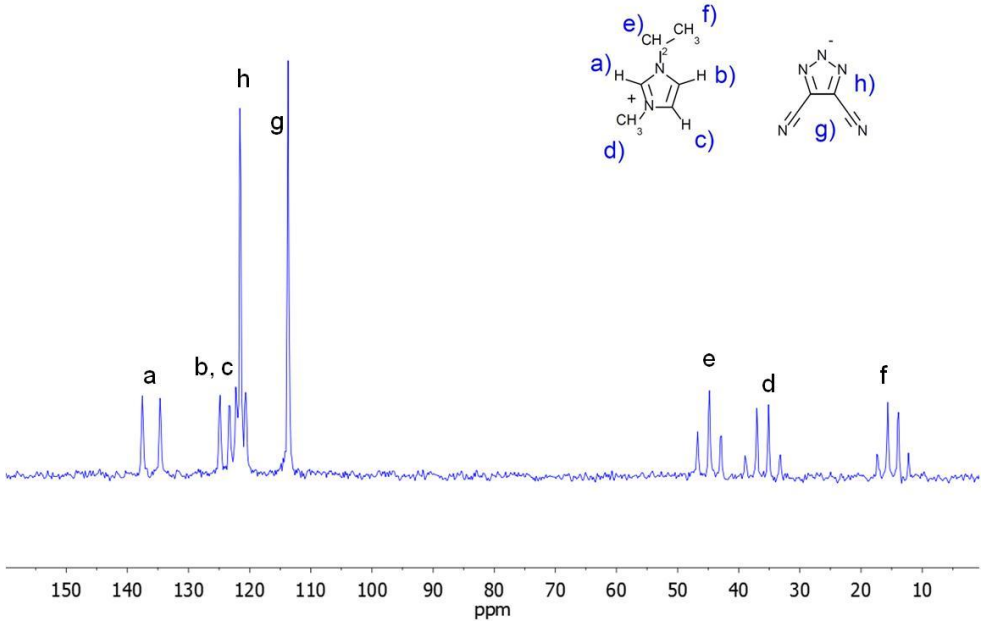

Figure 4.4: ^{13}C NMR Spectra of EMIMDCTA IL at 60^{o}C without decoupling.

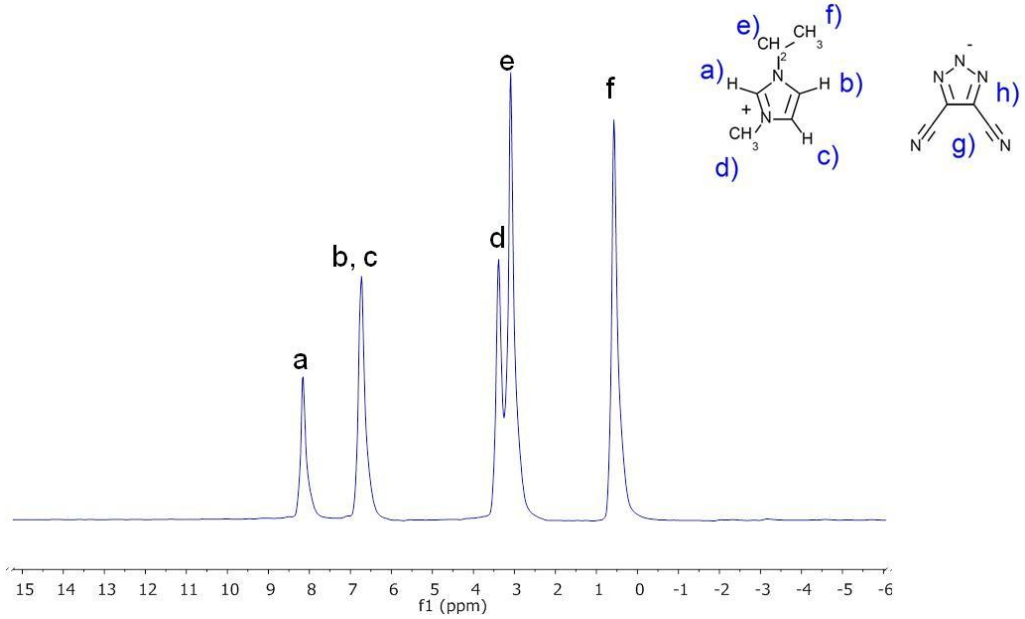

Figure 4.5: ^{1}H NMR Spectra of EMIMDCTA IL at 60^{o}C without decoupling.

In ^{13}C and ^{1}H NMR spectra, each peak identifies the position of carbon and proton nuclei in different environment of molecule and also shows the chemical shift with respect to TMS. The peaks a, b, c, e, d and f are from the cation and the peaks g, h from the anion. As it

is easy to separate anion and cation from ^{13}C spectra, self – diffusion coefficients are easily determined for anion and cation of ILs.

4.3.2. ^{13}C and ^{1}H Self-diffusion Coefficients

^{13}C diffusion measurement gives the self-diffusion coefficients for both cation and anion but ^{1}H diffusion measurements give self-diffusion coefficients only for cation as there are no protons in the anion. The self-diffusion coefficients of anion and cation for each IL at 25°C and 60°C are shown in table 4.1.

Table 4.1: Self-diffusion coefficients and cation transport number of fluorine free ionic liquids at 25°C and 60°C.

Sample Name	298K cation diff. coeff. (in x10^{-11} m^2s^{-1}) ^{1}H ^{13}C	298K anion diff. coeff. (in x10^{-11} m^2s^{-1})	333K cation diff. coeff. (in x10^{-11} m^2s^{-1}) ^{1}H ^{13}C	333K anion diff. coeff. (in x10^{-11} m^2s^{-1})	T+ 298K/333K cation transport number
EMIMDCTA	3.07 (±0.03) 2.76 (±0.04)	2.5 (±0.2)	13.7 (±0.2) 12.8 (±0.2)	12.3 (±0.1)	0.54 / 0.52
BMIMDCTA	1.87 (±0.02) 1.81 (±0.02)	1.8 (±0.2)	8.53 (±0.03) 7.22 (±0.2)	7.4 (±0.2)	0.50 / 0.52
Pyr13-DCTA	1.36 (±0.01) 1.17 (±0.04)	1.5 (±0.1)	7.2 (±0.5) 7.8 (±0.8)	8.6 (±0.8)	0.46 / 0.46
Pyr14-DCTA	1.61 (±0.01) 1.41 (±0.03)	1.7 (±0.1)	7.31 (±0.05) 6.39 (±0.1)	7.7 (±0.2)	0.47 / 0.47
Pyr13-TCM	4.7 (±0.2) 4.4 (±0.8)	5.5 (±0.4)	19.2 (±0.6) 18.8 (±0.3)	18.6 (±0.5)	0.45 / 0.50
EMIM-DCA	6.83 (±0.18) 6.18 (±0.18)	6.7 (±0.5)	20.02 (±0.2) 18.49 (±0.3)	19.9 (±0.3)	0.49 / 0.49
Pyr13-DCA	4.76 (±0.05) 4.04 (±0.05)	6.4 (±0.3)	13.5 (±0.2) 14.5 (±0.3)	16.3 (±0.2)	0.41 / 0.46
Pyr14-DCA	3.62 (±0.01) 3.00 (±0.01)	4.5 (±0.3)	10.73 (±0.1) 9.59 (±0.1)	13.5 (±0.3)	0.42 / 0.43

There is very good agreement between ^{1}H and ^{13}C diffusion measurements, which provides a measure of confidence for the ^{13}C NMR results. The data from table 4.1 shows that the ILs based on small anions such as DCA and TCM have higher self-diffusion coefficients than ILs with large anion such as DCTA. The self-diffusion coefficients are also almost the same for anion and cation for all ILs. This is because, these ILs have approximately the same volume of cation and anion. The discrepancy between cation diffusion coefficients determined from both nuclei is less than ±10%. The cation transport numbers are also shown in table 4.1 and are calculated from the diffusion coefficients by the following equation

$$T^{+} = \frac{D_{+}}{\left(D_{+} + D_{-}\right)} \quad \text{..... (4.2)}$$

where, D_{+} is the self diffusion coefficient of cation and D_{-} is the self diffusion coefficient of anion. The data shows that ILs with the imidazolium based cation have higher cation transport number than pyrrolidinium based ILs. Imidazolium based ILs have lower viscosities than Pyrrolidinium based ILs as in fig. 4.6.

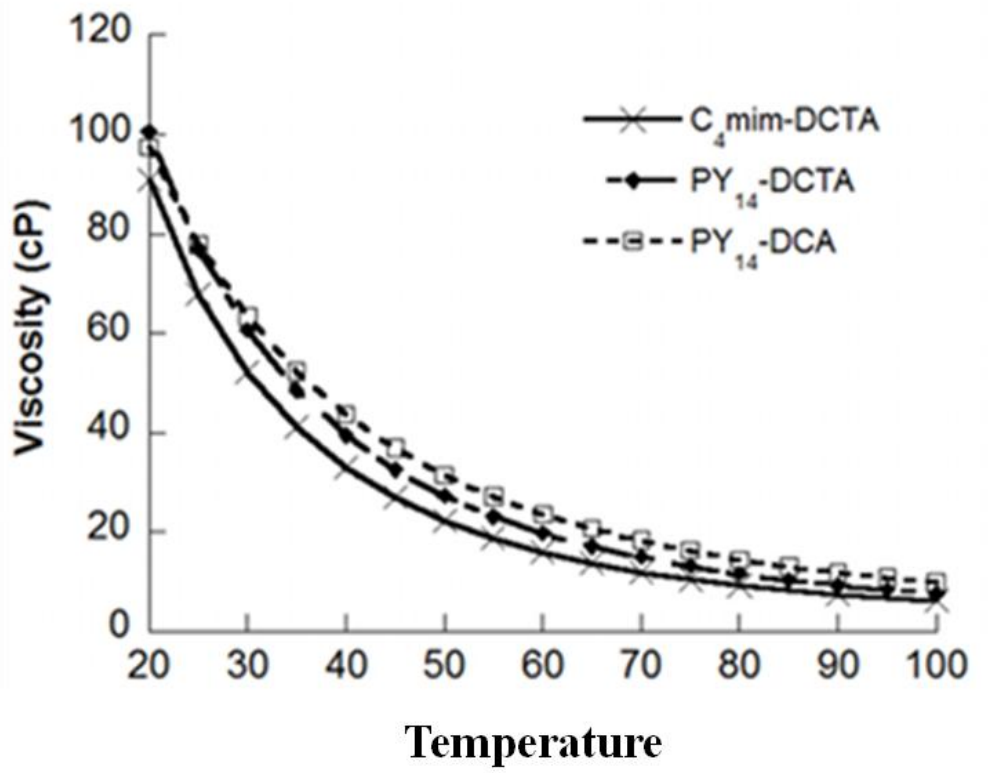

Figure 4.6: Temperature dependence of the viscosity of the ILs (EMIMDCTA and DCA, Py_{14}DCTA and DCA).

Variable temperature (VT) diffusion measurements were performed on Py_{14}DCTA IL as it has melting point at 0^{o}C. The self-diffusion coefficients of Py_{14}DCTA IL at VT are shown in table 4.2.

Table 4.2: Self-diffusion Coefficients of $Py_{14}DCTA$ IL as a function of temperature

Temperature °C	Nucleus	Cation diff. coeff. (in x 10^{-11} m^2s^{-1})	Anion diff. coeff. (in x 10^{-11} m^2s^{-1})
30	^{13}C	**2.22 (+/- 0.1)**	**2.74 (+/- 0.01)**
	^{1}H	**2.18 (+/- 0.02)**	
40	^{13}C	**2.80 (+/- 0.09)**	**3.26 (+/- 0.12)**
	^{1}H	**3.21 (+/- 0.03)**	
50	^{13}C	**3.96 (+/- 0.17)**	**4.70 (+/- 0.15)**
	^{1}H	**4.77 (+/- 0.04)**	
60	^{13}C	**6.54 (+/-0.37)**	**7.78 (+/-0.15)**
	^{1}H	**7.42 (+/-0.07)**	
70	^{13}C	**10.8 (+/- 0.54)**	**12.7 (+/- 0.25)**
	^{1}H	**10.7 (+/- 0.06)**	
85	^{13}C	**13 (+/- 0.5)**	**15 (+/- 0.6)**
	^{1}H	**12.9 (+/- 0.4)**	
100	^{13}C	**22.4 (+/- 0.7)**	**24.9 (+/- 0.9)**
	^{1}H	**24.8 (+/- 0.5)**	

There is also a very good agreement between ^{1}H and ^{13}C self-diffusion coefficients in this VT measurement, which proves again the confidence on the self-diffusion coefficients of anion. The cation and anion have similar self-diffusion coefficients as in fig. 4.7.

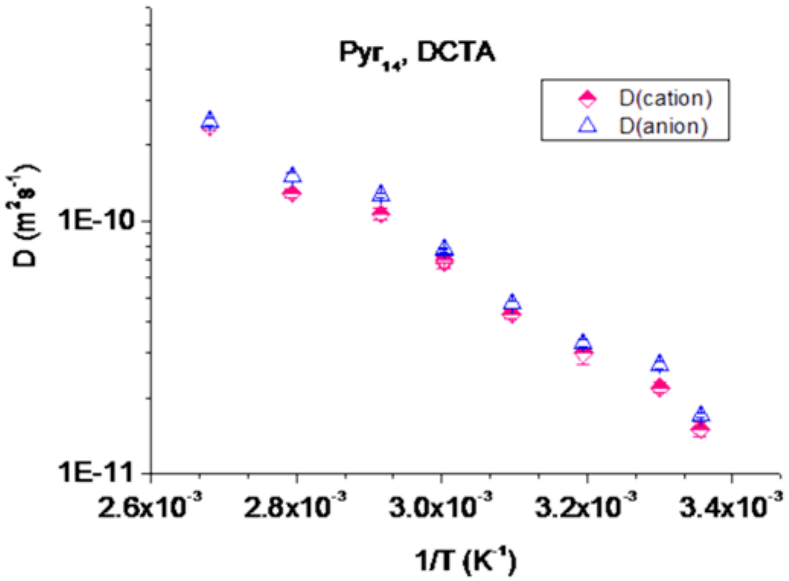

Figure 4.7: Variable temperature self-diffusion coefficients of cation and anion of Py_{14}DCTA IL.

4.3.3. Calculated and Experimental Conductivity Values

The conductivity measurements on these ILs were performed at North Carolina State University.

The Arrhenius plot of measured conductivity of ILs is shown in fig. 4.8. The data shows that EMIMDCTA has the highest conductivity and BMIMDCTA has the lowest conductivity of all other ionic liquids except EMIMDCA and Pyr_{13}TCM ILs. The conductivity measurements were not performed on EMIMDCA and Pyr_{13}TCM ILs due to shortage of samples.

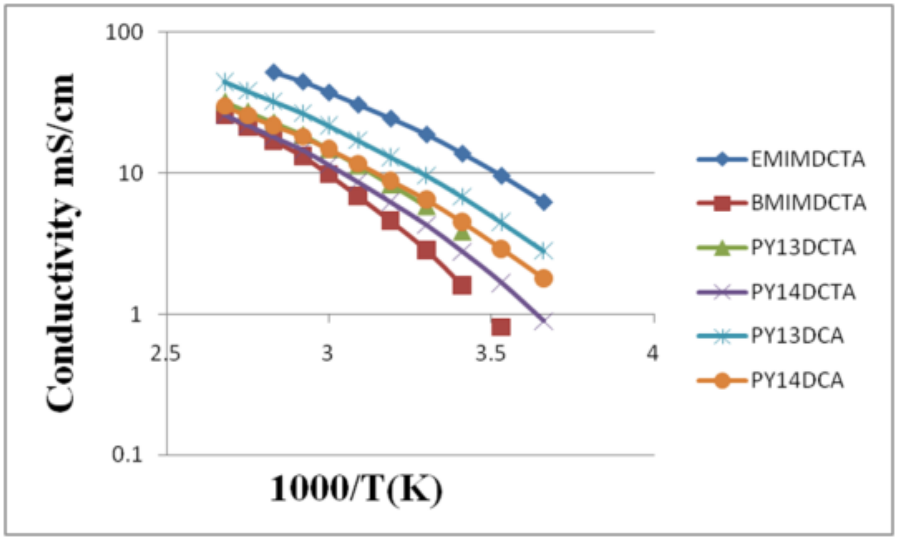

Figure 4.8: Arrhenius plot of measured conductivity at variable temperature.

The molar conductivity Λ_{NMR} is correlated with the diffusion coefficient by the Nernst-Einstein equation as 4.3.

$$\Lambda_{NMR} = \frac{N_A e^2}{RT}(D_+ + D_-) \quad \text{..... (4.3)}$$

where N_A is the Avogadro's number, e the charge of electron, R the gas constant, T the absolute temperature and all the cations and anions are assumed to be mobile. The calculated molar conductivity and measured conductivity at 60^{o}C are given in table 4.3. The calculation of molar conductivity at 25^{o}C may be problematic because some ILs are in a supercooled state at room temperature.

Table 4.3: Calculated conductivity Λ_{NMR}, measured conductivity Λ_M values at 60^{o}C.

T (K)	Ionic Liquids	^{13}C D_{cation} (m^2 s^{-1})	^{13}C D_{anion} (m^2 s^{-1})	Λ_{NMR} (S cm^2 mol^{-1})	Λ_M (S cm^2 mol^{-1})
333.15	$IM_{104}DCTA$	7.2×10^{-11}	7.4×10^{-11}	4.9	3.2
	$Pyr_{13}DCTA$	7.8×10^{-11}	8.6×10^{-11}	5.5	3.4
	$Pyr_{14}DCTA$	6.4×10^{-11}	7.7×10^{-11}	4.7	2.9

Table 4.3 shows the molar conductivity for DCTA based ILs as the value of density for DCA based ILs is not known. Calculated conductivities for all DCTA based ILs are higher than molar conductivities, because the diffusion experiments counts all diffusive species even though there are neutral species such as ion pairs or higher aggregates and conductivity experiments count only charged species.

4.4. Summary

Ionic liquids with fluorine free anions have good diffusion rates and also good conductivities. Comparing all the data, DCA based ILs have higher self-diffusion coefficients than DCTA based ILs at both temperatures. Also the comparison between the calculated conductivity and measured conductivity for all DCTA based ILs shows that there are incomplete ion dissociation.

The goal was to perform NMR pulse field gradient experiment on ^{13}C nucleus and to obtain self-diffusion coefficients for Fluorine free anions. The experimental data prove that the experiments have been done successfully. The agreement between the ^{1}H and ^{13}C NMR results shows that the self-diffusion coefficients of anions are reliable.

4.5. Acknowledgement

This project is supported in part by the U. S. DOE BATT program and by a grant from the U. S. DOE- Basic Energy Sciences.

Chapter 5

5. Nuclear Magnetic Resonance technique to investigate Nafion ionomer aggregation for Direct Methanol Fuel Cell

This work has been done in collaboration with Dr. Hui Yang at Shanghai Institute of Microsystem and Information Technology, Shanghai Advanced Research Institute, Chinese Academy of Sciences, Dr. Daniel Akins at City College of CUNY and Dr. Sophia N. Suarez at Brooklyn College of CUNY.

5.1 Introduction

Direct methanol fuel cell (DMFC) is a potential power source for electronic and portable devices due to its high energy density, low operating temperature and easy fuel storage capacity. The main drawbacks to make DMFC commercially successful are their durability and the cost of platinum as a catalyst. To overcome these drawbacks, researchers are investigating the development of a novel membrane electrode assembly.

The membrane electrode assembly (MEA) is the heart of DMFC. It plays an important role in the DMFC performance as the electrochemical reactions takes place within a three phase boundary zone: catalyst, reactants and electrolyte [1]. Each reaction active site is composed of catalyst and Nafion ionomer. Therefore, it is important to maximize the catalyst and electrolyte interface in order to extend the three phase boundary zone [2]. Different studies on this issue have shown that the main barrier to maximizing the contact area between the catalyst and electrolytes are the significant differences in sizes of carbon particles and Nafion micelles (figure 5.1). Nafion ionomers have the tendency to aggregate

and in different aggregation states. Small Nafion particles first aggregate through their hydrophobic backbones to form rod-like primary aggregations with the ionic side chains surrounding the surface of the rod-like structures. These primary aggregation particles aggregate again through the hydrophilic ionic side chain to form secondary aggregation [3]. These two aggregation process are found in alcohol/water mixture [3].

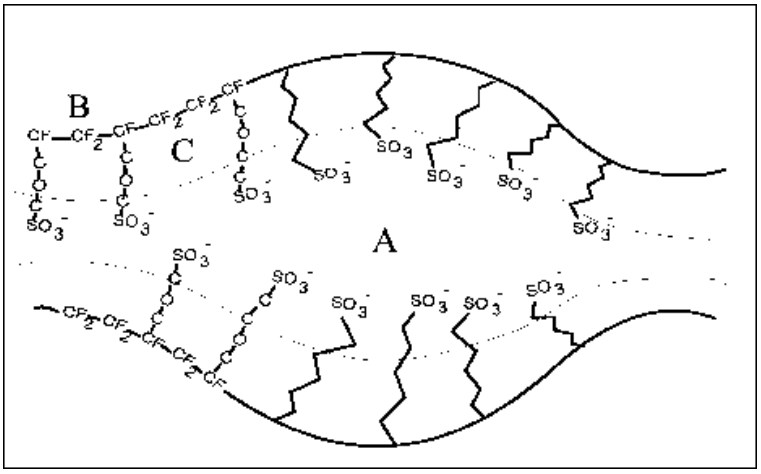

Figure 5.1: Nafion microstructure.

Various research has been performed to suppress the aggregation of Nafion ionomer, for example by adding NaOH to the aqueous solution [2]. In this chapter, a NMR spectroscopic technique is described to study the Nafion aggregation states after heat treatments of the solution (without Pt/C catalyst ink) at different temperatures. The studies of aggregation state of Nafion solution (with Pt/C catalyst ink) by Dynamic Light Scattering are also presented in this chapter, which was performed at the Shanghai Institute of Microsystem and Information Technology, Shanghai Advanced Research Institute, Chinese Academy of Sciences in China.

5.2. Experimental

5.2.1. Preparation of Pt/C Catalyst Ink

Pt/C catalyst ink was prepared by Hui Yang's group at Shanghai Institute of Microsystem and Information Technology, Shanghai Advanced Research Institute, Chinese Academy of Sciences in China.

To prepare Pt/C catalyst ink, 10mg of Pt/C catalysts (HiSpec 9100, Johnson Matthey), 0.5mL of as-received Nafion solution (Aldrich, Nafion 117 solution, 70160 - 5 wt.% in lower aliphatic alcohols and water) and 2.5mL of ultrapure water were mixed ultrasonically to form a suspension. This mixture was heat-treated for 1 h at 25, 50, 80^{o}C, respectively, and then mixed ultrasonically for a period of time. The particle distribution of congeries formed between Pt/C nanoparticles and Nafion ionomers was examined by a Mastersizer 2000 particle size analyzer (Malvern, Inc.) at room temperature. For NMR measurements, only Nafion (from Aldrich) solution was taken.

5.2.2. NMR Experiment

NMR measurements were conducted on a 300MHz Varian Direct Digital Drive Spectrometer with magnetic field 7.1 T. ^{19}F NMR spectra, spin lattice relaxation time and diffusion measurements were made. The diffusion probe was not fluorine free, so there was a significant background ^{19}F signal. Therefore, a fluorine free static broadband probe was used to obtain NMR spectra following a single $\pi/2$ pulse. Each peak of Nafion was defined from spectra as in fig 5.2, which agreed with ref [5]. NMR spectra were referenced with respect to $CFCl_3$ at 0 ppm.

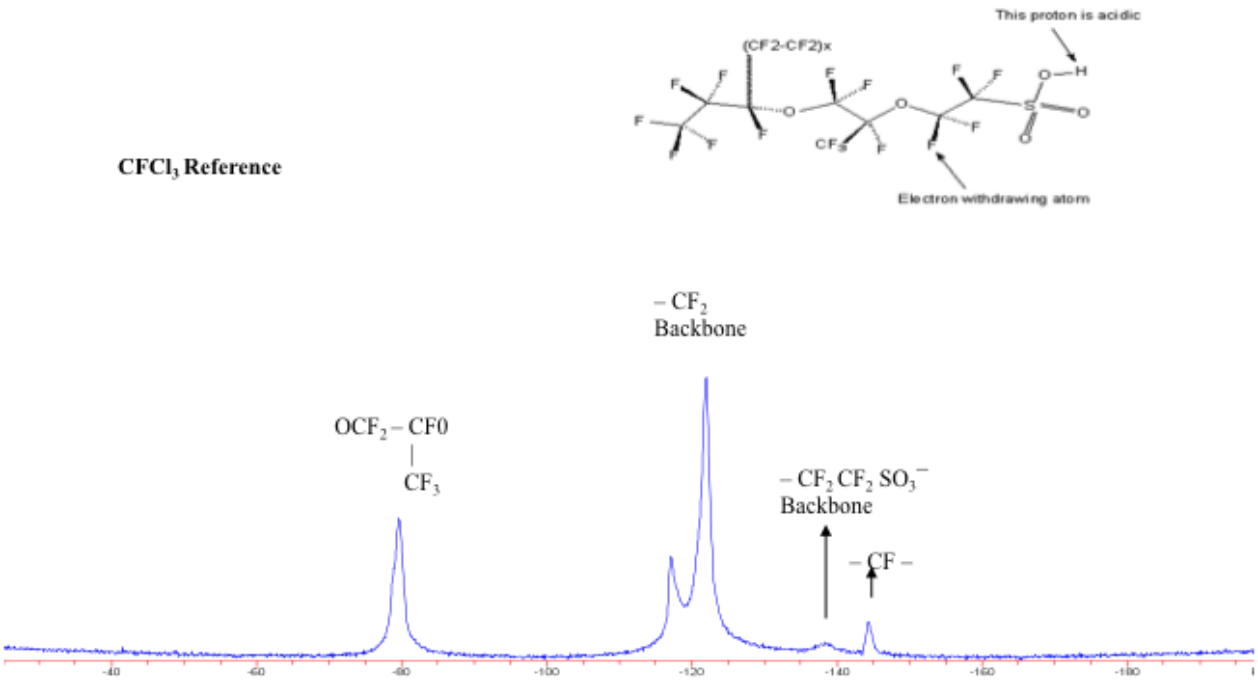

Figure 5.2: NMR Spectra of ^{19}F in Nafion Solution

The pulsed field gradient spin echo experiments were performed using a 5mm dual frequency DOTY diffusion probe. An aqueous solution of LiTf (Lithium Triflate) was used as a reference. Self diffusion coefficients were obtained by fitting the following equation:

$$A(g,2\tau) = A(0,0)\exp[-\gamma^2 g^2 D\delta^2(\Delta - \frac{\delta}{3})]$$

where A (0, 0) is the initial echo amplitude, A (g) is the attenuated echo amplitude and D is the self-diffusion coefficient, γ is the gyromagnetic ratio and g is the gradient field strength. Δ and δ are the delay time between the gradient pulses and duration of each gradient pulse. Δ and δ were adjusted to achieve maximum attenuation for a given g and 15 values of g (ranging from 0.5 ~ 210 T/m) were taken to get the diffusion profile. Spin lattice relaxation times T_1 were determined following the inversion recovery pulse (π-τ-π/2) sequence for 10 values of τ. Diffusion and T_1 measurements were performed at 25°C.

5.2.3. Viscosity Measurements

Viscosity measurements were performed using the falling ball viscometer provide by Gilmont as shown in fig 5.3. Viscosities were obtained by the following equation

$$\eta = k(\rho_f - \rho)t$$

where η is the viscosity of liquid, K is the constant for stainless steel ball which was measured experimentally with known viscosity, ρ_f is the density of the steel ball, ρ the density of the liquid, and t the time takes for ball to fall in viscometer. This experiment was done at 25^{o}C.

Figure 5.3: Viscometer with Falling Ball.

5.3. Result and Discussion

5.3.1. The distribution of congeries in the catalytic ink and catalyst layer by dynamic light scattering

The DLS experiment was performed at the Shanghai Institute of Microsystem and Information Technology, Shanghai Advanced Research Institute, Chinese Academy of Sciences in China.

Particle size distributions of catalyst ink prepared at the various temperatures are shown in Fig. 5.4. It is clearly seen that the catalyst ink prepared at the high temperature formed smaller agglomerates than those prepared at the low temperature. For the catalyst ink prepared at 25^{o}C, the particle size distribution was mainly in the region of ca.0.03 to 0.32μm and ca.0.72 to 52.5μm. About 63.4% of congeries size ranging from ca.0.72 to 52.5μm. Clearly, most of congeries formed from Pt/C particles and Nafion ionomers existed as large aggregated particles at room temperature. When the catalytic ink was pre-heated at ca.50^{o}C, many large particles broke up to form small ones, only 34.5% of congeries size ranging from ca. 0.72 to 45.7μm and 65.5% of congeries size ranging from ca. 0.02 to 0.28μm . Furthermore, when the catalyst ink was heated at ca.80^{o}C, 79.9% of congeries size ranging from ca. 0.02 to 0.28μm and 20.1% of congeries size ranging from ca.1.1 to 13.2μm. Particles larger than 14μm completely disappeared. Obviously, the large agglomerates formed from Pt/C particles and Nafion ionomers are broken up to form small ones at elevated temperatures.

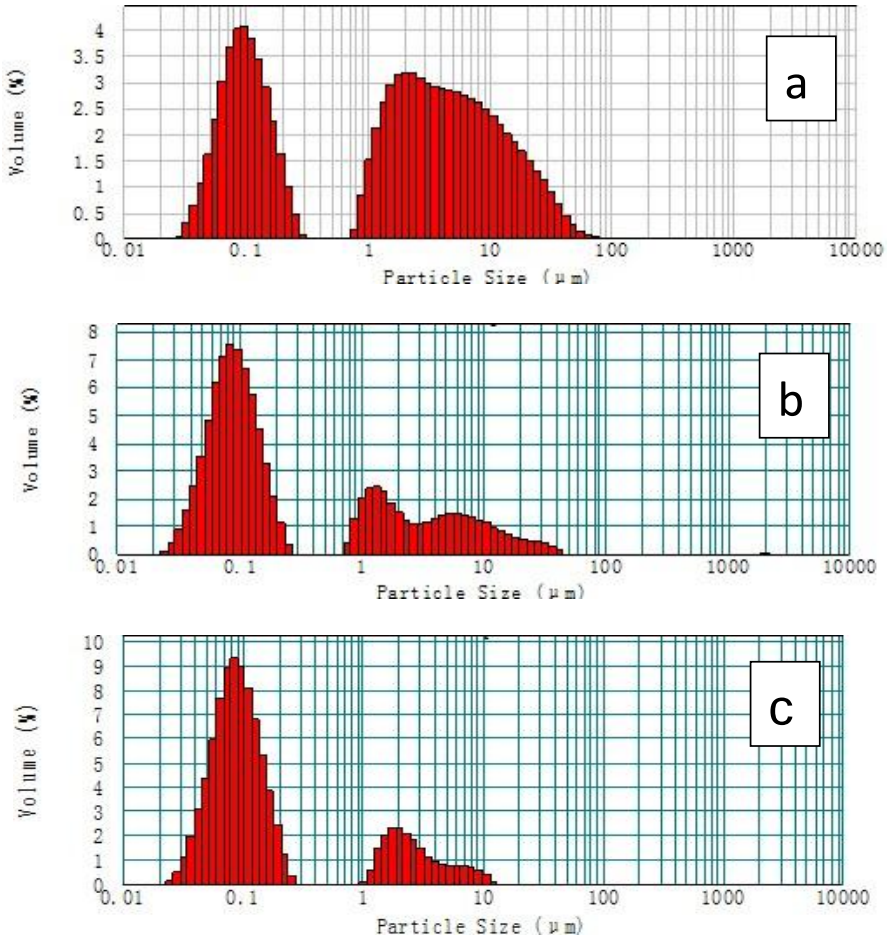

Figure 5.4: Particle size distribution of dilute Nafion solution after heat treatment at different temperature.

5.3.2. Hydrodynamic Radius of Nafion Particle by NMR diffusion and Viscosity Measurements

Hydrodynamic radii of Nafion particles in Nafion solution (without Pt/C catalyst ink) with heat treatment at different temperatures are shown in table 5.1. Hydrodynamic radii are obtained by the Stokes-Einstein equation as:

$$r = \frac{k_B T}{6\pi\eta D}$$

Where r = radius of the particle.

k_B = Boltzmann const. = $1.38\times10^{-23} m^2 kgs^{-2} k^{-1}$

T = Temperature in Kelvin

D = Self Diffusion Coefficient at temperature T

η = Viscosity of the Nafion solution at T

Samples for NMR and Viscosity measurements are labeled as A, B and C where sample A as prepared at 25°C, sample B at 50°C and sample C at 80°C (details in experimental section). Self-diffusion coefficient, T_1 values and viscosity are also shown in table 5.1.

Table 5.1: Self-diffusion coefficients, T_1 value, Viscosity and Radii of three heat-treated samples.

Temperature in Celsius	Sample Name	Nucleus	Spin-Lattice Relaxation Time, T_1 in second	Diffusion Coefficients in $\times10^{-11} m^2/s$	Viscosity in $\times10^{-3}$ Pa.s	Radius in $\times10^{-9} m$
25°C	Sample A	^{19}F	0.92(+/-0.05)	3.2 (+/-0.1)	1.9	3.6
	Sample B		0.89(+/-0.05)	3.6 (+/- 0.1)	2.2	2.8
	Sample C		0.90(+/-0.04)	4.4 (+/-0.1)	2.4	2.1

Spin-lattice relaxation time T_1 is almost same for all three samples, indicating that relaxation time is not affected by heat treatment. This is expected as T_1 depends only on the local environments of the molecule. Therefore, dispersion or aggregation of particles does not change T_1.

The self-diffusion coefficient increases with increasing the heat-treatment at high temperature as shown in table 5.1. Sample C has the highest self-diffusion coefficient although the viscosity is also high. This can be explained as the heat treatment at higher temperature (80^oC) makes the solution more viscous but dissociates the aggregates. A probable explanation for increased solution viscosity at higher temperature is that some of the alcohol solvent has evaporated. Therefore, the hydrodynamic radius of Nafion particle is smaller for sample C compared to other samples because radius and self-diffusion coefficient are inversely related. The radius of sample C is almost two times less than the sample treated at 25^oc. The size of particles from NMR result is much smaller than the size distribution from Dynamic Light Scattering (DLS). This is because Pt/C catalyst ink is used in DLS experiment which gives much larger aggregates than just the Nafion with Water/Alcohol mixture, which is used in NMR experiment.

5.4. Conclusion

It can be concluded from the result and discussion that the particle size of Nafion ionomers in solution and the size distribution in catalyst ink decreases with increasing pre-heated temperature. Sample C that is pre-heated at 80^oC obtained a higher self-diffusion coefficients, low hydrodynamic radius and low distribution of congeries. Despite the large difference in particle sizes between the catalyst ink and the precursor Nafion solution, the trend toward decreasing aggregate size with increasing heat treatment is the same for both systems, suggesting that Nafion aggregation plays a significant role in catalyst ink aggregation.

5.5. Acknowledgements

This project is supported by the U.S. office of Naval Research and National “863” High-Technology Research Programs of China.

Chapter 6

6. NMR Studies of Orientation Effect on Polymer Electrolytes for Lithium Batteries

This work has been done in collaboration with Dr. Golodnitsky at School of Chemistry, Tel-Aviv, Israel.

6.1. Introduction

Polymer electrolytes have been extensively researched for development as solid electrolyte separators between the lithium metal anode and Li-intercalation compound, typically a lithium transition metal oxide, for high energy density Li-ion batteries. In 1975, Peter V. Wright, a polymer chemist from Sheffield, first showed that poly- ethylene oxide (PEO) can act as a solid electrolyte conducting polymer [1]. PEO is composed of a repeat unit of $–CH_2CH_2O-$ and is thought to form helical secondary structures (Figure 6.1). Michel Armand was the first to suggest the use of PEO Li-salt complexes for electrolytes. Immediately after his suggestion, it was determined that lithium salts, such as lithium triflate (LiTf) (Figure 6.1) would dissolve well in PEO. But understanding the formation of Li-salt complexes and the nature of the charge transport mechanism were not so simple. In 1983, it was established after experiments and detailed mechanistic studies that ionic motion in salt polymer complexes were not due to charge hopping from site to site but rather a continuous motion occurring in the amorphous region of the polymeric material [2]. After three decades of effort at synthesizing amorphous polymer, only incremental improvements in conductivity (10^{-2} mS/cm at room temperature) have been realized [3].

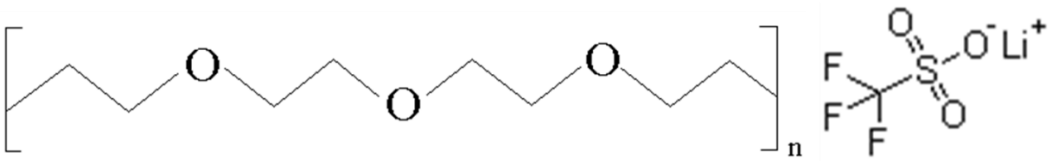

PEO LiTf

Figure 6.1: Structure of Polyethylene-oxide (PEO) and Lithium triflate (LiTf).

Recent studies on this issue have found that the ionic conductivity of crystalline LiTf-PEO complexes is higher than amorphous phase and helix-to-helix hopping is the rate-determining step in long-range lithium ion conduction at temperatures below the melting point (65^{o}C) [4-6]. The crystalline phase in concentrated PEO-based composite polymer electrolytes (CPE), containing nanosize inorganic fillers, has found to be a major contributor to the overall ionic conductivity at temperatures close to the eutectic point [7]. For the CPEs, the interfacial interaction between the filler particles and the polymer-salt complex significantly influences ionic transport [8-9].

Polymer crystals show direction dependent properties [10]. Typically, solid polymer electrolytes are prepared by casting from solution [10]. The casting of the polymer electrolyte provides mainly parallel to-the-film-plane helices. This leads to low ionic conductivity in the perpendicular direction, which for most practical applications, especially for high-energy-density all-solid-state batteries, is crucial [11]. Therefore, in order to increase the near-ambient-temperature orthogonal cation mobility (both inside the helical channel and via helix-to-helix jump), polymer chains should be oriented along the Z-axis [11]. In this chapter, NMR studies are described to determine the degree of orientation of LiTf:PEO_3 in magnetically aligned films from analysis of the nuclear quadrupole interaction

using ^{7}Li static NMR spectroscopy. The conductivity results are also described in this chapter which is obtained from School of Chemistry at Tel-Aviv in Israel.

6.2. Experimental

6.2.1. Preparation of composite polymer electrolytes

This work has performed in School of Chemistry, Tel-Aviv, Israel.

The polymer electrolytes were prepared from a slurry of poly (ethylene oxide) (PEO), (MW5×106) (Aldrich), with lithium salts by casting from acetonitrile (ACN) solution or a mixture of solvents on a Teflon tray. PEO was vacuum dried at 45°C for about 24h. The lithium salts (LiTf) were vacuum dried at 150°C for about 24h. All subsequent handling of these materials took place under an argon atmosphere in a VAC glove box with water content <10 ppm. LiTf was quickly dissolved in the relevant solvent at room temperature inside a glass flask, and then accurately weighed portions of PEO were added. Highly concentrated polymer electrolytes were originally conceived as composed of 1:3 lithium salt-to-EO complexes. Appropriate quantities of magnetic nanosize particles were dissolved in acetonitrile separately, followed by 30-min homogenizing in an ultrasonic bath. The two solutions were mixed and stirred for about 2h to obtain homogeneous slurry.

The LiTf:$P(EO)_3$ PEs containing magnetic nano size particles were cast under a strong magnetic field, created by commercial samarium-cobalt (SmCo) (0.82T) and neodymium-iron-boron (NdFeB) (1.22T) disc shaped permanent magnets in the standard "dipole" arrangement in a homemade device. The values of magnetic field were determined for a typical disc separation and was 23 mm. Samples were prepared under a highly inhomogeneous field by fixing a conically tapered iron shim to one of the magnet poles that

are referred as gradient magnetic field (GMF) as in fig 6.2. Samples that were prepared without applying any magnetic field are referred as no magnetic field (NMF). The thickness of the film varied from 100-150 µm (NMF) and 100-430 µm (GMF).

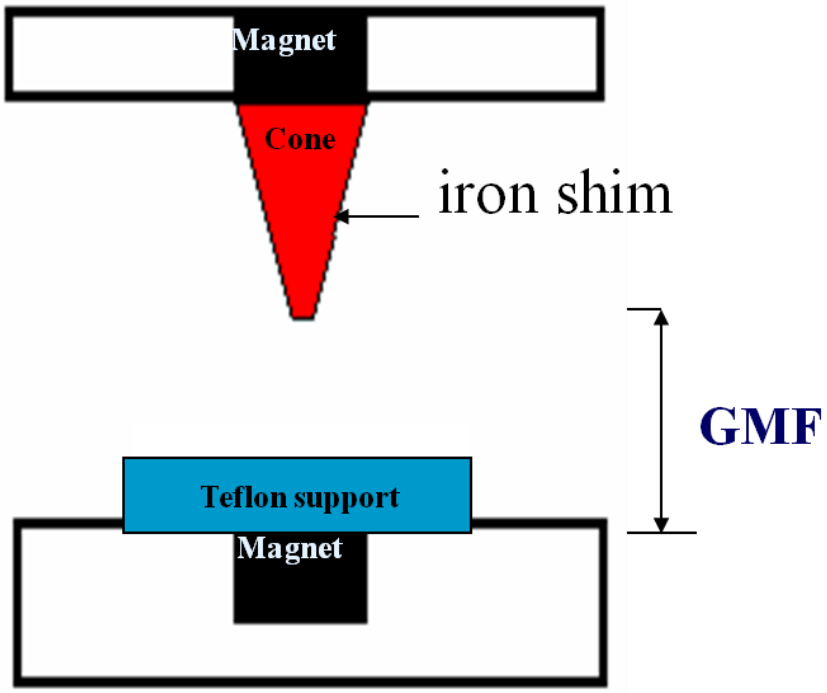

Figure 6.2: Experimental setup of casting polymer electrolytes under magnetic field.

6.2.2. NMR Experiment

^{7}Li wide line (static) NMR measurements were conducted with a Varian Direct Digital Drive NMR Spectrometer and 7.1T magnet corresponding to a ^{7}Li resonance frequency of 117.13 MHz. Spectral acquisition was accomplished by Fourier transformation of the half-echo following a 90_x–90_y solid echo pulse sequence with pulse width of 3 µs and pulse separation of 50 µs. Rectangular slices of sample were cut from films prepared with no MF and GMF as described previous section. The slices were fixed between two glass cover slips and sealed in a10 mm tube in Ar glove box, and then oriented in the NMR radio

frequency coil so that the angle between the plane of the film and the external magnetic field could be varied as in fig 6.3. Typically 2400 acquisitions were signal averaged for each spectrum with time between acquisitions of about 30s.

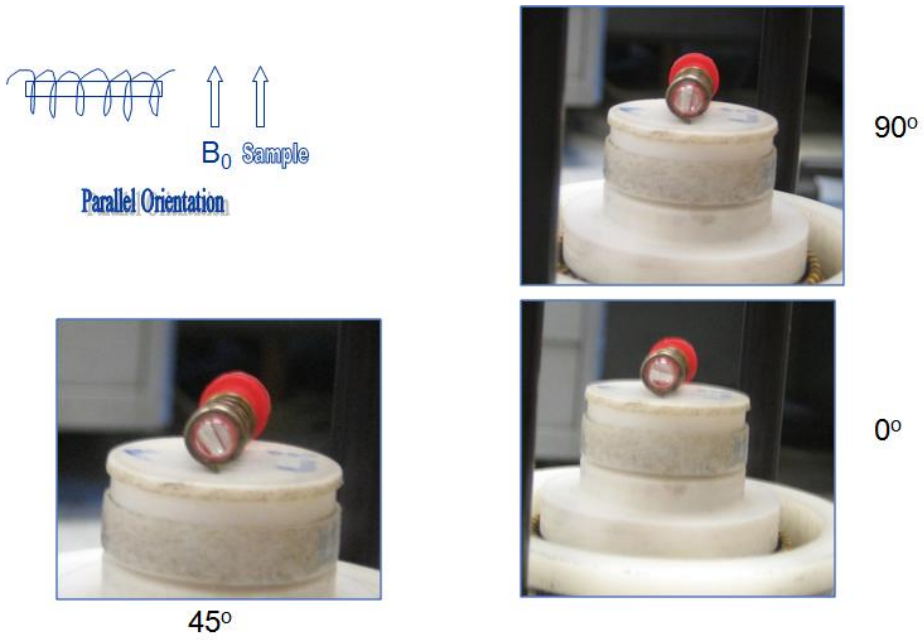

Figure 6.3: Polymer electrolytes inside NMR tube in a static broadband NMR probe.

6.3. Results and Discussion

6.3.1. Conductivity

Conductivity measurements have performed at Tel-Aviv University in Israel.

The Arrhenius plots of total conductivity of LiTf:P(EO)$_3$ PEs without magnetic field and with GMF by SmCo and NdFeB are shown in fig. 6.5. At 35°C, typically cast LiTf PE has shown a total conductivity of 1×10^{-7} mScm^{-1}. At near ambient temperatures, σ_T of the PE cast under GMF created by a SmCo or NdFeB magnet is fivefold and one order of magnitude higher, respectively. At temperatures near the melting point of the PEO, the difference in conductivity decreases. The total conductivity values of LiTf:P(EO)$_3$ were

separated into the intra chain and inter chain conductivity inputs and the SEI resistance, with the use of an equivalent circuit fitted for the relaxation phenomena occurring in the Li/PE/Li system (Fig. 6.4, inset). Both intra and inter chain conductivities are improved by MF casting, but the stronger effect is detected for σ_{GB}. The σ_{GB} value at 65°C increased with MF casting by a factor of 5 (from 2.4×10^{-5} to 1.1×10^{-4} mScm^{-1}), while at the same temperature, bulk increased by only a factor of 3 (from 1.3×10^{-4} to 4.5×10^{-4} mScm^{-1}). In 1:3 LiTf PEs cast under MF, the R_{SEI} is lower by a factor of 4.

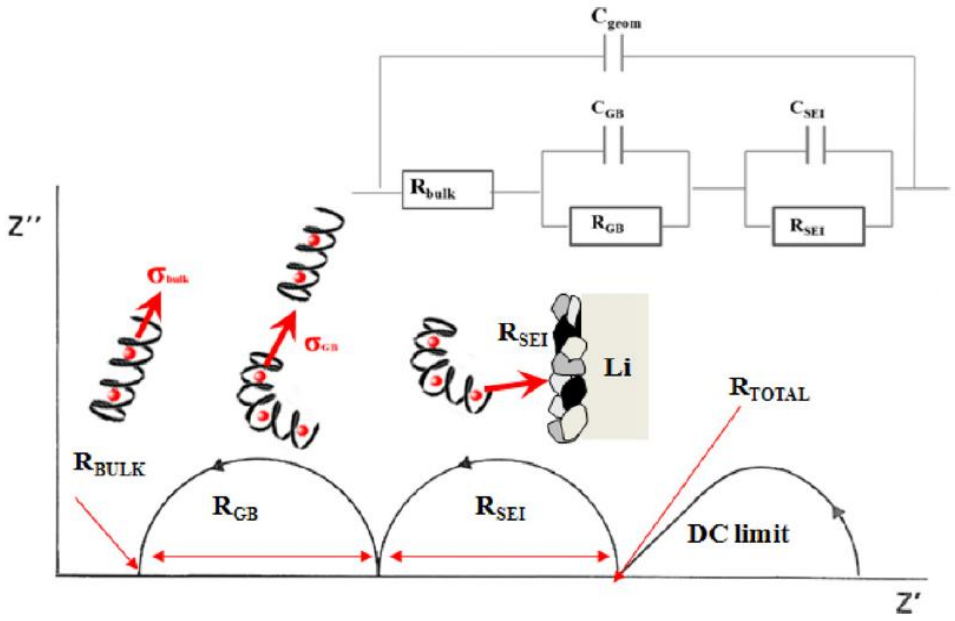

Figure 6.4: Schematic presentation of Nyquist plot and equivalent circle used for fitting.

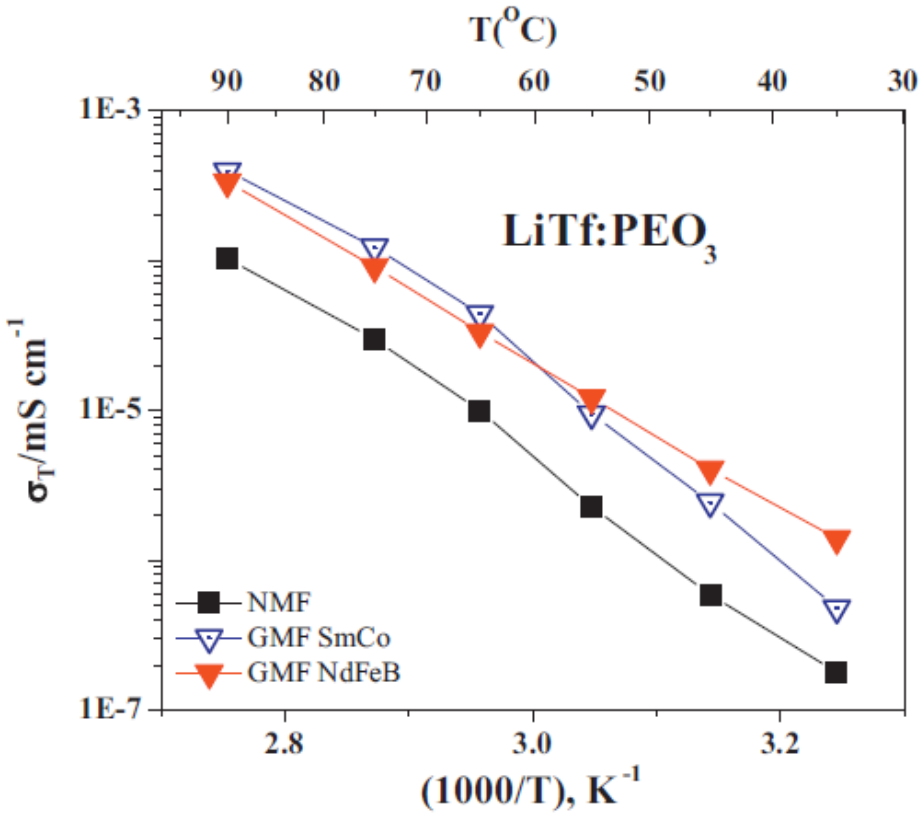

Figure 6.5: Arrhenius plots of LiTf:P(EO)$_3$ polymer electrolytes: typically cast without and with magnetic field of different intensity.

6.3.2. NMR results

NMR spectra of ^{7}Li for NMF and GFM PEs are shown in fig 6.6. ^{7}Li (I=3/2) is a quadrupolar nucleus and the outer satellite transitions are expected to be very sensitive to short range structural variations. Theoretical (simulated) spectra of a spin 3/2 nucleus with a fixed quadrupole coupling constant and asymmetry parameter at three different orientations that is three different angles between the NMR spectrometer magnetic field and the principle axis of the quadrupolar interaction tensor are shown in fig. 6.6. Simulated powder pattern for a randomly oriented polycrystalline sample, where the angular dependent nuclear quadrupole interaction is integrated over all solid angles are also shown in fig 6.7.

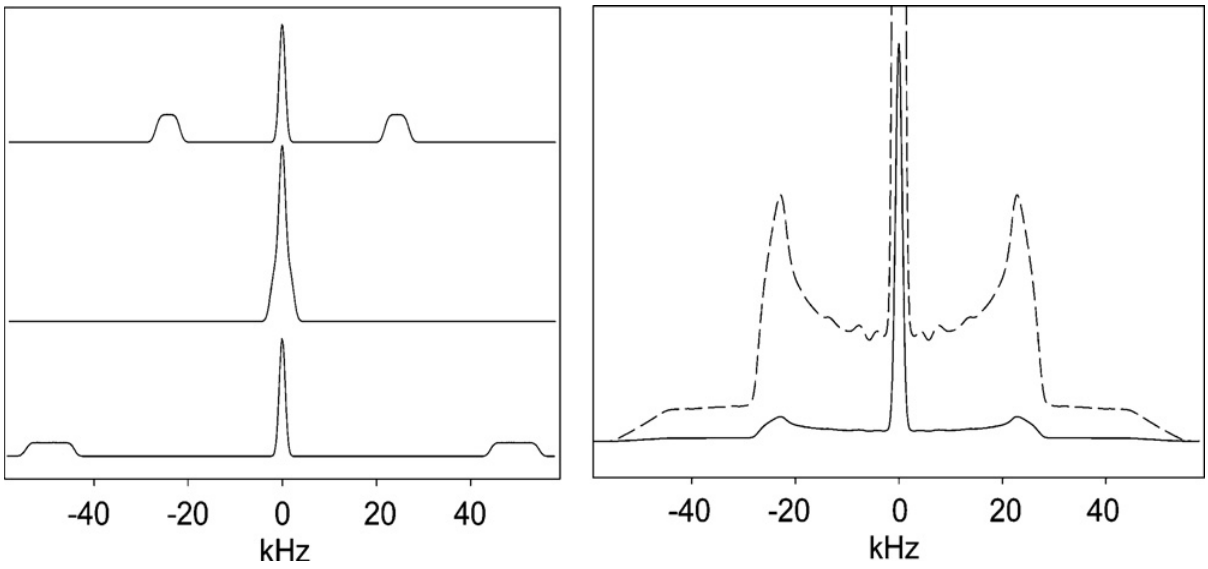

Figure 6.6: Simulated spectra of a spin 3/2 nucleus at three different angles between the NMR spectrometer magnetic field and the principle axis of the quadrupole interaction tensor (Left). Experimental vs. the simulated "powder pattern" for a randomly oriented polycrystalline sample (right).

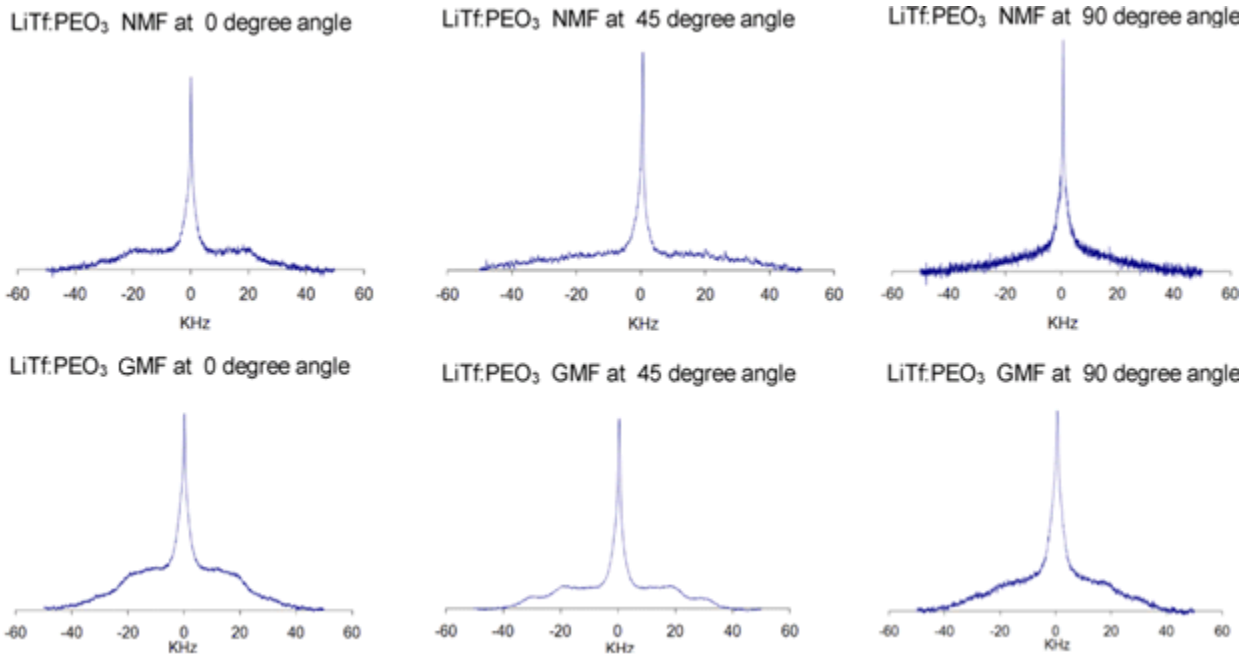

Figure 6.7: NMR spectra of LiTf:P(EO)$_3$ polymer electrolytes at different orientation.

It is clear from figure 6.6 that the local ordering by the quadrupole satellite transitions is different in films cast under GMF (bottom) compared to NMF (top). There is also a clear difference of NMR spectra in each sample at three different angles because there are in plane orientation effects from casting of solution. The narrow peak of the spectra is due to the central transition $\left(+\frac{1}{2} \Leftrightarrow -\frac{1}{2}\right)$. The shoulders of the spectra are the satellite transitions $\left(\pm\frac{3}{2} \Leftrightarrow \pm\frac{1}{2}\right)$ due to the first order quadrupolar interaction. The quadrupolar-coupling constant, estimated using the Win Solids software package is approximately 125 KHz.

6.4. Summary

The quadrupolar interaction provides a sensitive short range probe of the Li^+ environment, and the observed angular dependence of the spectra indicates some degree of molecular orientation in the samples prepared under a gradient magnetic field. Also, LiTf:P(EO)-based concentrated polymer electrolytes casting under strong magnetic field have higher ionic conductivity than NMF.

6.5. Acknowledgement

This project is supported by a grant from U.S. office of Naval Research and the BSF foundation for financial support.

Chapter 7

7. NMR study of $AlCl_3$ containing Ionic Liquid for Aluminum Batteries

This work has been done in collaboration with Dr. Daniel Steingart, Nilesh Ingale, Dr. Joshua Gallaway and Dr. Sanjoy Banerjee at City College of CUNY, New York, NY.

7.1. Introduction

Aluminum or Aluminum intercalation compounds as electrodes and Ionic Liquids (ILs) as electrolytes can provide advanced secondary rechargeable batteries with high energy density for electric vehicles. Aluminum anode batteries with ILs have many advantages compared to current Lithium-ion batteries such as: low cost due to the abundant aluminum resources, high energy density due to tri-valence of aluminum ions and safer operation due to non-flammable ILs. The comparison of anode materials in different battery configurations are shown in table 7.1 [10-14].

Table 7.1: Comparison of different electrodes based on charge capacity.

Type of Battery	Electrode	Status	Charge Capacity mAh/gm	Cycle Life
Li Battery	Li	Research	3860	-
Li-ion Battery	$LiCoO_2$	Commercial	140	1000
Li-ion Battery	Silicon	Research	3579	< 100
Zn/MnO2 Battery	Zinc	Research	820	20
Al based Battery	Aluminum	Research	2900	Cycleable

Theoretically, Al should be competitive for secondary rechargeable batteries, but technical problems have prevented its practical use. The standard reduction potential of aluminum is -1.66 V (vs. a standard hydrogen electrode), which prevents the use of aqueous

electrolyte due to decomposition of water before deposition of Al. Also Al has a strong affinity towards oxygen and hence cannot be electrolyzed from aqueous solutions [1]. Protective oxide layers form on the surface of Al, which provides excellent corrosion resistance but also prevents the use of Al as anode material. The Al oxide layer cannot be dissolved in most aqueous solutions. Ionic Liquids (ILs) can potentially be the most useful electrolyte for the recovery of Al. Ionic liquids have interesting properties such as, low vapor pressure, non-flammability, thermal stability and high electrical conductivity, which are very important in battery applications, as described elsewhere in this thesis [2]. ILs may also provide an alternative low temperature, low energy approach to primary aluminum production than the Hall-Heroult process (Calcined alumina is electrolyzed to aluminum metal in a molten bath of cryolite at 960^{o}C) [3].

Major studies have been conducted on Chloroaluminate ionic liquids such as 1-ethyl-3-methyl imidazolium chloride and 1-butyl-3-methyl imidazolium chloride for aluminum electrodeposition at ambient temperatures [3]. Chloroaluminate ILs are formed by mixing an organic halide with anhydrous $AlCl_3$. Numerous studies have shown that aluminum can only be electrodeposited from Lewis acidic chloroaluminates, in which the mole fraction of $AlCl_3$ is greater than 0.5 [4]. Acidic Cloroaluminate contains $Al_2Cl_7^-$ species, which is reducible in chloroaluminate melt by the following equation [3]:

$$4Al_2Cl_7^- + 3e^- \rightarrow Al + 7AlCl_4^- \quad \text{..... (7.1)}$$

In this chapter, an NMR study is described to understand the equilibria between principal chloroaluminate species [5]. Cyclic voltammetry and galvanostatic charging and

discharging experiments are also described in this chapter to understand the electrodeposition of aluminum from acidic mixtures of 1-ethyl-3-methyl imidazolium chloride (EMIMCl) and aluminum chloride ($AlCl_3$) and its use as secondary battery electrolytes.

7.2. Experimental

7.2.1. Preparation of Electrolyte

The part of this project was done at City College of CUNY.

All electrolyte preparation was performed in an inert atmosphere in a glove box (argon filled) provided by VAC atmosphere systems. The environment inside the glove box was maintained below 1ppm oxygen and moisture. The electrolyte solution 1-ethyl-3-methyl imidazolium tetrachloroaluminate (EMIMCl) (>95% pure) manufactured by BASF was obtained from Sigma-Aldrich. The lewis acidity was increased by addition of $AlCl_3$. The $AlCl_3$ (anhydrous, 99.985% metal basis) was obtained from Alfa Aesar Company. The $AlCl_3$ was added slowly to the electrolyte (EMIMCl+$AlCl_3$) over a period of time and the mixture was continuously stirred resulting in an amber colored solution. The solution was kept in an aluminum dish for 2-3 days, which absorbed residual moisture present in the ionic liquid, resulting in a colorless electrolyte.

The electrochemical test cell was made from acrylic sheet; copper plate was used as a working electrode (WE) and a pure aluminum plate as a counter electrode (CE). The reference electrode (RE) used was pure Al wire (99.9995%) from Alfa Aesar. All potentials are reported vs. aluminum RE. The electrodes were cleaned with 3M Scotch-Brite ultrafine pad before use and rinsed with deionized water and dried. The electrode spacing was 5 mm and the electrode surface area was 25 mm^2. The WE and CE are held facing each other and

RE was located between the WE and CE, 2.5mm from each. The electrochemical cell was assembled outside the glove box and then transferred to the glove box.

Battery cycling experiments were carried out with an Arbin Battery Testing system having 4 channels, using this same electrode configuration. Deposited Al was galvanostatically cycled by deposition and stripping on the working electrode with a copper current collector.

7.2.2. NMR Experiment

The samples were run using a Hahn echo pulse sequence at 11.7 T using a Varian Inova 500MHz NMR Spectrometer and a liquids probe at ambient temperature. The samples were referenced to aluminum chloride dissolved in D_2O at 0 ppm. Spin lattice relaxation times were also measured using the inversion recovery pulse sequence. NMR experiments were performed at 25^{o}C.

7.3. Result and Discussion

7.3.1: Effect of Electrolyte concentration

This experiment was performed at City College of CUNY.

Cyclic voltammetry was performed for different concentrations of the electrolyte as shown in Fig.7.1.

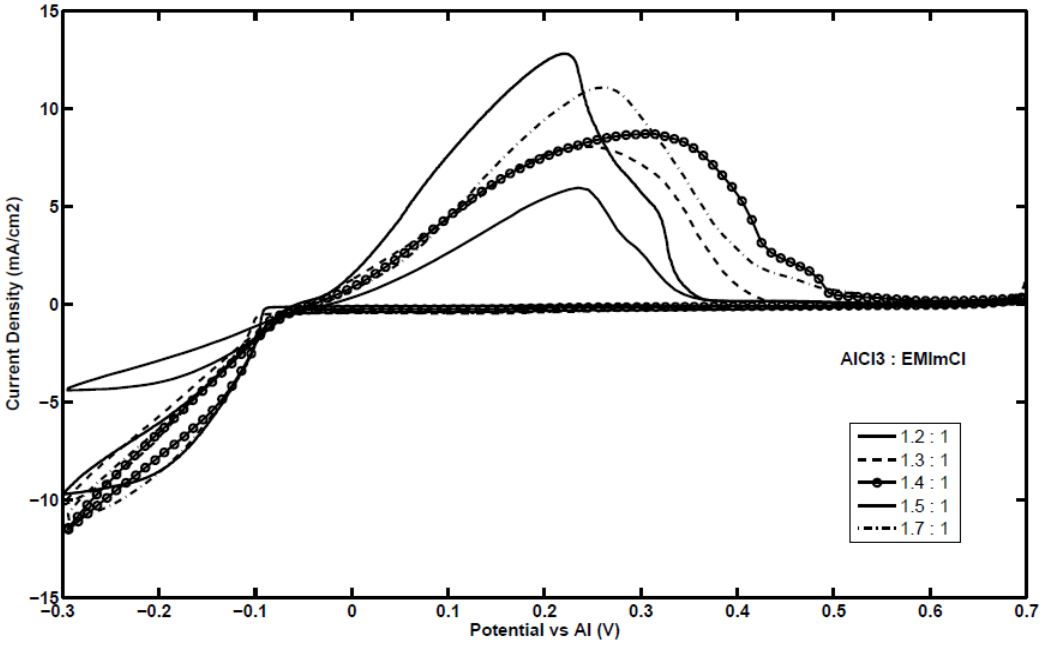

Figure 7.1: Effect of concentration of $AlCl_3$ based EMIMCl electrolyte on deposition and stripping of Al at scan rate of 2 mV/sec.

From Fig. 7.1, the deposition current increased as the $AlCl_3$/EMIMCl electrolyte concentration increased from 1.2:1 to 1.5:1, correspondingly to an increase in electroactive species Al_2Cl_7. This trend is seen even more clearly in the anodic portion of the curve. Table 7.2 shows the effect of concentration of electrolyte on the areas under the cathodic and anodic curves and current efficiency.

Table 7.2: Effect of different electrolytes and their concentration on the current efficiency

Concentration of the electrolyte (Molar Ratio)	Cathodic Area (C)	Anodic Area (C)	Current Efficiency (%)
EMIM based Electrolyte			
1.2 : 1	0.4417	0.2913	65.94
1.3 : 1	0.4245	0.3236	76.23
1.4 : 1	0.7276	0.6026	82.83
1.5 : 1	0.8056	0.7815	97.01
1.7 : 1	0.8465	0.8047	95.06

As the concentration of $AlCl_3$ in the electrolyte increased from 1.2:1 to 1.5:1, the current efficiency also increased. However, as the concentration of $AlCl_3$ in the electrolyte increased from 1.5:1 to 1.7:1, the current efficiency decreased. It has been shown by Gale et al. [6] that the effect of addition of $AlCl_3$ to the EMIMCl has a strong effect on the concentration of electroactive species $AlCl_4$ and Al_2Cl_7 present in the solution. This was shown by Raman spectroscopic measurements with a $AlCl_3$-1-butylpyridinium chloride system. In the experiments performed by Gale et al. [6], the ratio of $Al_2Cl_7^-$ to $AlCl_4^-$ was 1.2 in the case of 1.5:1.0 and 3.3 in the case of 1.75:1 electrolyte solution. Thus the amount of $AlCl_3$ present contributes to the formation of $Al_2Cl_7^-$, which is mainly responsible for Al electrodeposition. But as the concentration of $Al_2Cl_7^-$ increases, formation of higher Al complexes such as $Al_3Cl_{10}^-$ [7] occurs and $Al_2Cl_7^-$ is not available for Al electrodeposition, which in turn affects the current efficiency. All further experiments were carried out with 1.5:1 $AlCl_3$ and EMIMCl electrolyte solution.

7.3.2. Electrodeposited Al as proof of concept

This experiment had performed at City College of CUNY.

To study the reversibility of a deposited Al electrode, multiple cyclic voltammetry was carried out from 1.5:1 ($AlCl_3$ to EMIMCl) concentration of the electrolyte. It was observed that deposited Al can be quantitatively cycled with 95% current efficiency as the area under the deposition and stripping peak remains the same indicating the same amount of Al is electrodeposited and stripped from the Cu current collector for 100-120 cycles in cyclic voltammetry. After 100-120 cycles, the deposit was black in nature. For the study of deposited Al as an electrode in secondary rechargeable batteries, galvanostatic deposition

and stripping was carried out as would be the case in a practical battery. The optimal deposition current density was decided from galvanostatic experiments and SEM results. It was observed that at 12 mA/cm^2 the deposits obtained were pure Al in the form of spherical particles. The deposition current density used was 12 mA/cm^2 for 30 min and stripping current density used was 12 mA/cm^2 for 28 min. The 60th cycle of deposition and stripping is shown in Fig. 7.2.

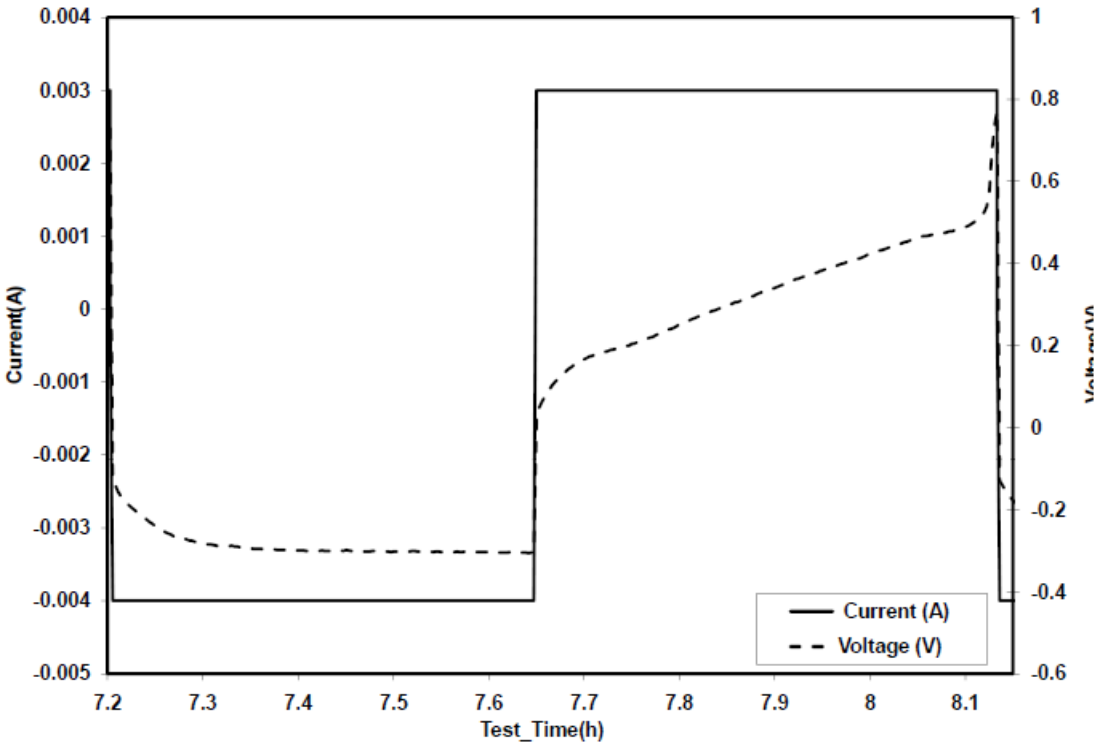

Figure 7.2: A typical deposition-stripping cycle of Al

An electrochemically reversible Al electrode electrodeposited from ionic liquid mixtures with energy efficiency of 84% was obtained. From Fig. 7.2, during deposition the voltage was around -0.35V and 0.4 V vs Al during stripping. But after 70 cycles, the voltage was not stable during stripping and increased abruptly to 0.8V vs Al RE indicating the Al

had reacted further and could not be electrodissolved. Bright Al could be quantitatively cycled for 60-70 cycles. But after that a black deposit was observed on the Cu current collector during deposition and stripping. Therefore, as the voltage rapidly increased during stripping, the stripping cycle was discontinued. The charge storage capacity of deposited Al electrodes is shown in Fig. 7.3. The amount of deposited Al and amount of Al stripped from the electrode, calculated from the amount of charge passed and Faraday's First Law, was used as the basis for this calculation.

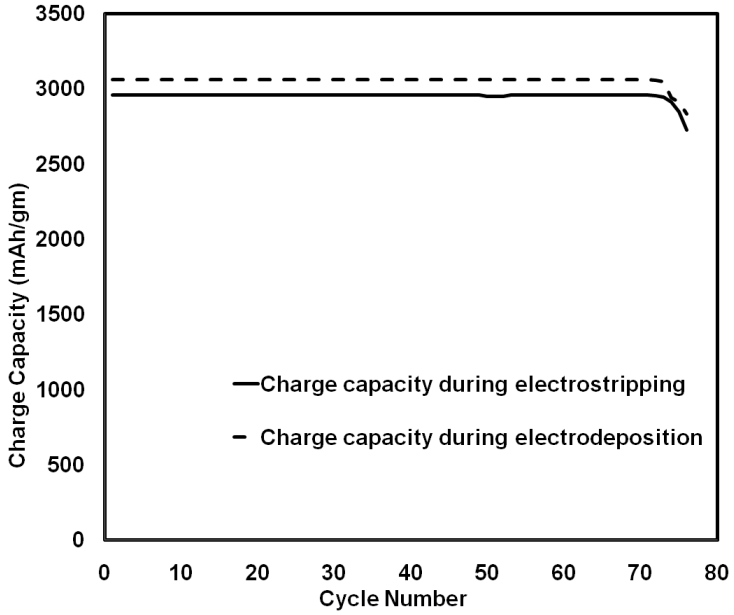

Figure 7.3: Charge capacity during electrodeposition and stripping.

The deposited Al electrode had a charge storage capacity of 2900 mAh/gm during deposition and the same during stripping which was maintained for 70 cycles with 84% energy efficiency. The theoretical specific capacity for Al electrode is 2980 mAh/gm [8].

During deposition and stripping, the Al electrode was used to its full capacity for 70 cycles. The charge capacity of deposited Al electrode was compared with graphite and $LiCoO_2$ electrodes in Li-ion batteries, which are around 140 and 372 mAh/gm respectively

[2]. The use of a silicon electrode in Li-ion batteries can give a charge capacity of 3579 mAh/gm. Zinc electrodes have a capacity of around 400 mAh/gm, which has been studied for Zn/MnO_2 battery [9]

7.3.3. NMR results

^{27}Al is a highly sensitive spin 5/2 quadrupolar nucleus that gives broad lines over a wide chemical shift range, and the shift ranges for 6, 5, 4-coordinated Al are well separated. ^{27}Al NMR Spectroscopy yields relaxation rates and chemical shift data, which are correlated to the binding and the local coordination environment around the aluminum nucleus.

The samples under investigation were different concentrations of $AlCl_3$ in EMIMCl IL solution as 1:1, 1.33:1, 1.5:1 and 2:1. The only anion available to bind to aluminum is chloride in all the samples studied.

The ^{27}Al NMR spectra of $AlCl_3$: IL mixtures of different concentration were recorded and are shown in figure 7.4. A resonance was observed at around 103 ppm for all concentrations of $AlCl_3$:IL which is consistent with the four – coordinated aluminum species, $AlCl_4^-$ and there was another resonance found at around 98 ppm with the increase of concentration of $AlCl_3$, which is consistent with the tetrahedral aluminum containing species, $Al_2Cl_7^-$ [3].

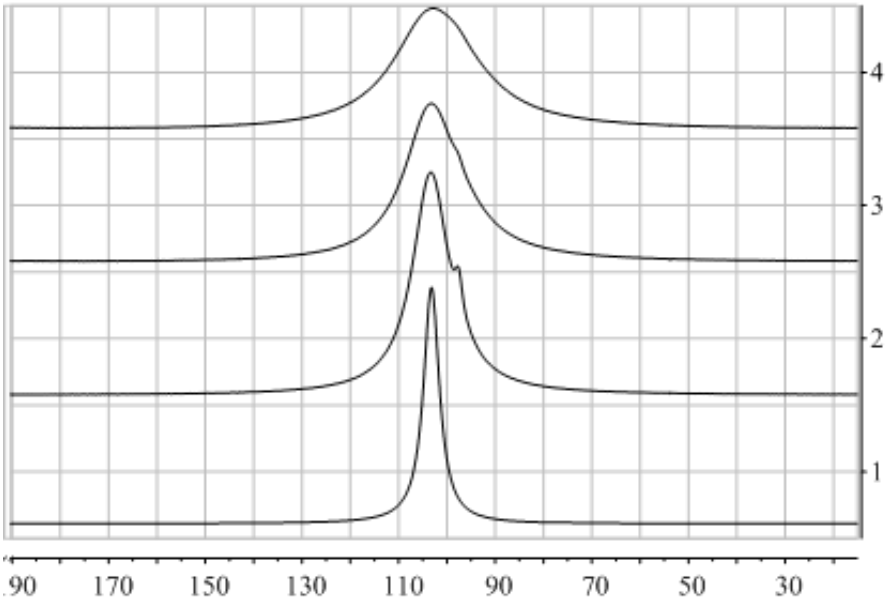

Figure 7.4: ^{27}Al NMR spectra of $AlCl_3$:EMIMCl at various $AlCl_3$ mole fraction as 1:1, 1.33:1, 1.5:1, 2:1 (down to up).

The presence of tetrahedral aluminum species, $AlCl_4^-$ and $Al_2Cl_7^-$ are also observed in electrolytes harvested from cycled cells. The initial composition is the 1.5:1 mixture and that spectrum is shown again in the bottom of Fig. 7.5. Distinct changes in linewidth and lineshape occur upon cycling as shown for the cases of 20 cycles and 50 cycles. The cycled electrolytes reveal a resolved spectral component associated with $AlCl_4^-$. The enhanced broadening of the 50-cycle sample arises from the aforementioned chemical exchange, but other factors such as changes in viscosity cannot be ruled out at this time. NMR spectra of cycled samples indicate that the concentration of chloroaluminate species in the electrolyte changes as a function of cycling.

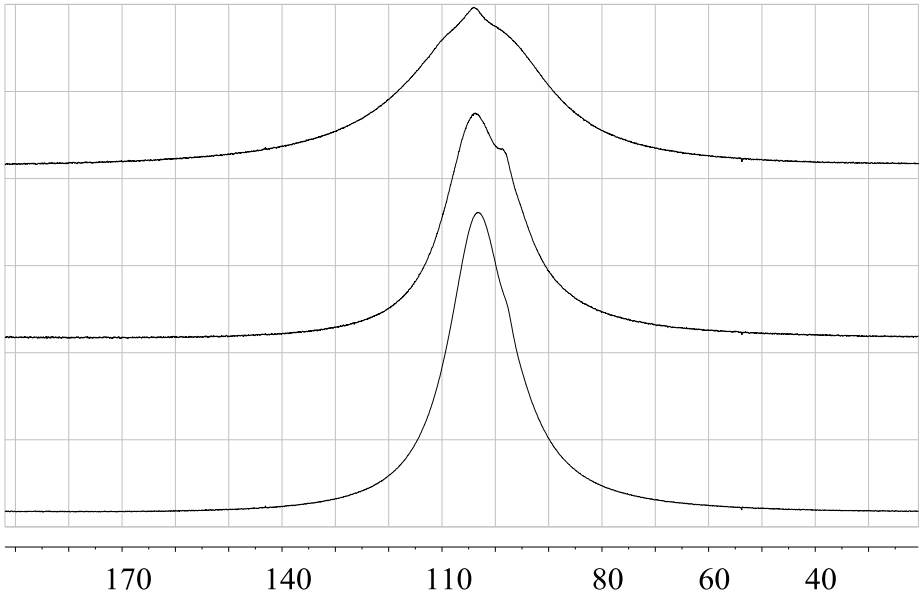

Figure 7.5: ^{27}Al NMR spectra of $AlCl_3$:EMIM 1.5:1 starting electrolyte 0 cycles, 20 cycles, 50 cycles (bottom to top).

The line widths of aluminum resonances vary with the relative concentration of aluminum chloride. This is, in part, might be attributed to changes in viscosity. T_1 relaxation data (table 7.3) also confirms that with an increase in the concentration of $AlCl_3$, the relaxation time decreases, resulting in the increase in line width of each resonance. Changes in T_1 and line width of the ^{27}Al resonances are attributed mainly to the efficient quadrupole relaxation mechanism.

Table 7.3: Spin-Lattice Relaxation times of different concentrations of $AlCl_3$ with IL at 25°C.

Samples Name	Relaxation Time, T_1 (s)
$AlCl_3$:EMIMCl (1:1)	0.2 (+/-0.002)
$AlCl_3$:EMIMCl (1.33:1)	1.8×10^{-04} ($+/-3.6\times10^{-05}$)
$AlCl_3$:EMIMCl (1.5:1)	1.5×10^{-04} ($+/-3.0\times10^{-05}$)
$AlCl_3$:EMIMCl (2:1)	8.78×10^{-05} ($+/-1.0\times10^{-05}$)
$AlCl_3$:EMIMCl (1.5:1) (20 cycles)	1.67×10^{-04} ($+/-2.6\times10^{-05}$)
$AlCl_3$:EMIMCl (1.5:1) (50 cycles)	9.14×10^{-05} ($+/-8.9\times10^{-06}$)

We can use the uncertainty relation (equ. 7.1) to check the average lifetime T_2* which is comparable to T_1 and line broadening as follows.

$$T_2^* \Delta\upsilon \approx T_1 \Delta\upsilon \approx \frac{1}{2\pi} \quad \ldots\ldots\ldots\ldots\ldots\ldots (7.1)$$

Where $\Delta\nu$ is the linewidth (half width full spectra).

Table 7.4: Average Life Time and Line width of different concentrations of AlCl3 with IL at 25°C.

Samples Name	Linewidth in Hz	Average Lifetime T_2* in s
$AlCl_3$:EMIMCl (1:1)	17.3	0.01
$AlCl_3$:EMIMCl (1.33:1)	1002	2×10^{-04}
$AlCl_3$:EMIMCl (1.5:1)	1843	8.6×10^{-05}
$AlCl_3$:EMIMCl (2:1)	2466	6.5×10^{-05}
$AlCl_3$:EMIMCl (1.5:1) (20 cycles)	2436	6.5×10^{-05}
$AlCl_3$:EMIMCl(1.5:1) (50 cycles)	3499	4.5×10^{-05}

Table 7.4 shows that T_2* and T_1 decrease with increasing concentration of $AlCl_3$ in IL. In order to properly interpret this result in terms of the relative concentrations of different Al species, one would need to measure the solution viscosity.

7.4. Summary

The Al electrodeposited from an acidic mixture of $AlCl_3$ and 1-ethyl-3-methyl imidazolium chloride is deep cycled for 70 cycles of deposition and stripping. The charge storage capacity of the deposited Al is 2900 mAh/gm (comparable to its theoretical charge storage capacity). Further cycling is limited due to the formation of a black deposit of uncertain structure and composition. During cycling electrodeposited Al, compositional changes take place in the electrolyte solution. From NMR results, it has been observed that the concentration of chloroaluminate species $Al_2Cl_7^-$ and $AlCl_4^-$ changes with increasing concentration of $AlCl_3$ and upon cycling.

7.5. Acknowledgement

This work was supported by the U.S. Department of Energy.

8. Bibliography

Chapter 1 & Chapter 2

1. Thomas B. Reddy, "Lindens Handbook of Batteries" Fourth Edition, The McGraw Hill (2011).

2. Horst Friebolin, "Basic One and Two Dimensional NMR Spectroscopy", Wiley-VCH (1998).

3. C.P. Slichter, "Principles of Magnetic Resonance", Happer and Row Publishers (1996).

4. J.R.Singer, "NMR Diffusion and Flow Measurements and an Introduction to Spin Phase Graphing", J.Phys, E:Sci. Instrum, Vol. 11, 1978, Printed in Great Britain.

5. E. O. Stejskal and J. E. Tanner, "Spin Diffusion Measurements: Spin Echoes in the presence of a Time Dependent Field Gradient", The Journal of Chemical Physics, Volume 42, Number1, January 1965.

6. M. H. Levitt, "Spin Dynamics", John Wiley & Sons, LTD (2007).

7. Joseph P. Hornak, Ph.D., "Basic of NMR".

8. Fuel Cell Basics, FC Tec, http://www.fctec.com/fctec_types_pem.asp, 2010.

9. Martyn J. Earle and Kenneth R. Seddon, "Ionic Liquids Green solvents for the future", Pure Appl. Chem., Vol. 72, No. 7, pp. 1391-1398, 2000.

10. Hiroyuki Ohno, "Electrochemical Aspects of Ionic Liquids", Wiley, March 02, 2011.

11. Walter A. van Schalkwijk and Bruno Scrosati, "Advances in Lithium-ion Batteries", Kluwer Academic / Plenum, NY, 2002.

12. Richard. Zhang and Z. Conrad Zhang, "Selective Sulfer Removal from Fuels using Ionic Liquids at Room Temperature", Akzo Nobel Chemicals, Inc.

13. A. Berthod, S. Carda – Broch, " Uses of Ionic Liquids in Analytical Chemistry".

14. Shengdong Zhu, Yuanxin Wu, Qiming Chen, Ziniu Yu, Cunwen Wang, Shiwei Jin, Yigang Ding and Gang Wu, "Dissolution of Cellulose with ionic liquids and its application: a mini – review", Green Chem, 2006, 8, 325-327.

15. Richard P. Swatioski, Scott K. Spear, John D. Holbrey and Robin D. Rogers, "Dissolution of Cellose with Ionic Liquids", J. AM. CHEM. SOC. 2002, 124, 4974-4975.

16. F. Enres, D. MacFarlane, A. Abbott, "Electrodeposition of Ionic Liquids", WILLEY-VCH Verlag GmbH & Co. KGaA, Weinheim.

17. A.S. Aricò, P. Bruce, B. Scrosati, J.M. Tarascon, W. Van Schalkwijk, Nature Mater. 4 366 (2005).

18. Jeremy Titman, "Introduction to solid state NMR anisotropic interactions", School of Chemistry, University of Nottingham.

19. Willium S. Price, "NMR Studies of Translational Motion", Cambridge University Press 2009.

20. Geil, B. "Measurement of Translational Molecular Diffusion Using Ultrahigh

Magnetic Field Gradient NMR." *Concepts in Magnetic Resonance Part A* 10, no. 5 (1998): 299-321.

21. Malcolm H. Levitt, "Spin dynamics", WILEY, Second Edition.

22. Jaime A. Farrington, "Variable Pressure and Temperature NMR Studies of Fuel Cell Polymer Electrolyte Membranes", Ph.D. Thesis, City University of New York, 2010.

23. Sohan De Silva, "Solid State NMR Studies of Energy Conversion and Storage Materials", Ph.D. Thesis, City University of New York, 2011.

Chapter 3

1. M. A. Navarra, J. Manzi, L. Lombardo, S. Panero and Bruno Scrosati, "Ionic Liquid-Based Membranes as Electrolytes for Advanced Lithium Polymer Batteries" ChemSusChem 2011, 4, 125-130.

2. A. Fernicola, Priscilla Reale, B. Scrosati, "Application of Ionic Liquids as electrolytes for safe and sustainable lithium ion batteries", abstract.

3. A. Fernicola, C. Sirisopanaporn and B. Scrosati, "LiTFSI-Py_{24}TFSI : a novel electrolyte for rechargeable lithium batteries", abstract.

4. P. Reale, A. Fernicola, B. Scrosati, "Compatibility of the Py_{24}TFSI-LiTFSI ionic liquid solution with $Li_4Ti_5O_{12}$ and $LiFePO_4$ Lithium ion battery electrodes", Journal of Power Sources 194(2009) 182-189.

5. M. Armand, F. Endres, D.F. MacFarlane, H. Ohno, B. Scrosati, " Ionic liquid

materials for the electrochemical challenges of the future" Nature Materials, 8 (2009) 621.

6. A. Fernicola, F. Croce, B. Scrosati, T. Watanabe, H. Ohno, "LiTFSI-BEPyTFSI as an improved ionic liquid electrolyte for rechargeable lithium batteries", J. Power Sources 2007, 174, 342.

7. A. Fernicola, F. C. Weise, S. G. Greenbaum, J. Kagimoto, B. Scrosati and A. Soletoa, "Lithium-Ion-Conducting Electrolytes: From an Ionic Liquid to the Polymer Membrane", J Electrochem Soc. 2009 May 5; 156(7): A514-A520.

Chapter 4

1. Pregosin, P. S. Pure Appl. Chem. 2009, 81, 615.
2. Pregosin, P. S.; Martínez-Vivente, E.; Anil Kumar, P. G. Dalton Trans. 2003, 4007.
3. Pregosin, P. S.; Anil Kumar, P. G.; Fernández, I. Chem. Rev. 2005, 105, 2977.
4. Stallmach, F.; Galvosas, P. Ann. Rep. NMR Spectrosc. 2007, 61, 51.
5. Borodin, O.; Gorecki, W.; Smith, G. D.; Armand, M. J. Phys. Chem. B 2010, 114, 5786.
6. Umecky, T.; Saito, Y.; Matsumoto, H. J. Phys. Chem. B 2009, 113, 8466.
7. Hayamizu, K.; Tsuzuki, S.; Seki, S. J. Phys. Chem. A 2008, 112, 12027.
8. Umecky, T.; Kanakubo, M.; Ikushima, Y. J. Mol. Liq. 2005, 119, 77. Johansson, P.; Nilsson, H.; Jacobsson, P.; Armand, M. Phys. Chem. Chem. Phys. 2004, 6, 895.
9. Egashira, M.; Scrosati, B.; Armand, M.; Beranger, S.; Michot, C. Electrochem. Solid State Lett. 2003, 6, A71.

10. E. O. Stejskal, J. E. Tanner, J. Chem. Phys. 42 (1965) 288.

Chapter 5

1. L.D. Raistrick, in: J.W. Van Zee, R.E. White, K. Kinoshita, H.S. Burney (Eds.), Diaphragms, Separators, and Ion Exchange Membranes, PV 86-13, The Electrochemical Society Proceedings Series, Penningon, NJ, 1986, p.172.
2. S. Wang, G. Sun, Z. Wu and Q. Xin, "Effect of Nafion ionomer aggregation on the structure of the cathode catalyst layer of a DMFC", Journal of Power Sources 165 (2007) 128-133.
3. Ewa Szajdzinska-Pietek, S.S., Andrzej Plonka, Self-Assembling of Perfluorinated Polymeric Surfactants in Nonaqueous Solvents. Electron Spin Resonance Spectra of Nitroxide Spin Probes in Nafion Solutions and Swollen Membranes. Langmuir, 1994. 10(7): p. 2188-2196.
4. Y. Kang, M. Ren, Z. Zou, Q. Huang, Z. Li, D. L. Akins and Hui Yang, "Improved electrocatalytic performance of Pd nanoparticles with size-controlled Nafion aggregates for formic acid oxidation", Electrochimica Acta 55 (2010) 5274-5280.
5. Q. Chen and K. Schmidt-Rohr, "19F and 13C NMR Signal Assignment and Analysis in a Perfluorinated Ionomer (Nafion) by Two-Dimensional Solid-State NMR", Macromolecules, 2004, 37 (16), pp 5995–6003.

Chapter 6

1. Bernadette Bensaude-Vincent and Michel Armand, Polymer Electrolytes, Materials Science & Engineering.
2. C. Berthier, W. Gorecki, M. Minier, M. B. Armand, J. M. Chabagno, P. Riguad, Solid State Ionics 11 (1983) p. 91.
3. M. B. Armand, Annu. Rev. Mater. Sci. 16 (1986) 245.
4. S.H. Chung, Y. Wang, S.G. Greenbaum, D. Golodnitsky, E. Peled, Electrochem. Solid-State Lett. 2 (11) (1999) 553.
5. D. Golodnitsky, E. Peled, Electrochem. Acta 45 (2000) 1431.
6. D. Golodnitsky, E. Peled, E. Livshits, A. Ulus, Z. Barkay, I. Lapides, S.G. Greenbaum, S.H. Chung, Y. Wang, J. Phys. Chem. A 105 (44) (2001) 10098.
7. E. Staunton, Y. G. Andeev, P. G. Bruce, Faraday Discuss, 134 (2007) 143.
8. D. Golodnitsky, G. Ardel, E. Peled, Solid State Ionics 147 (2002) 141.
9. A.J. Bhattacharyya, J. Maier, Adv. Mater. 16 (2004) 811.
10. E. Livshits, R. Kovarsky, N. Lavie, Y. Hayashi, D. Golodnitsky, E. Peled, "New insights into structural and electrochemical properties of anisotropic polymer electrolytes", Electrochimica Acta 50 (2005) 3805-3814.
11. R. Kovarsky, D. Golodnitsky, E. Peled, S. Khatun, P. E. Stallworth, S. Greenbaum, A. Greenbaum, "Conductivity enhancement induced by casting of polymer electrolytes under a magnetic field", Electrochimica Acta 2011.

Chapter 7

1. Mingming Zhang, Venkat Kamavarum, and Ramana G. Reddy, "New electrolytes for aluminum production: Ionic liquids", The Journal of The Minerals 55(11), pp. 54–57 (2003).

2. M Armand and J-M Tarascon, “Building better batteries.”, Nature 451(7179), pp. 652–7 (2008).

3. N. M. Rocher, E. I. Izgorodina, T. Ruther, M. Forsyth, D. R. MacFarlane, T. Rodopoulos, M. D. Horne and A. M. Bond, “Aluminium Speciation in 1-Butyl-1-Methylpyrrolidinium Bis(trifluoromethylsulfonyl)amide/ $AlCl_3$ Mixtures”, Chem. Eur. J. 2009,15, 3435-3447.

4. T. Rodopoulos, L. Smith, M. D. Horne and T. Ruther, “Speciation of Aluminium in Mixtures of the Ionic Liquids $[C_3mpip][NTf_2]$ and $[C_4mpyr][NTf_2]$ with $AlCl_3$: An Electrochemical and NMR Spectroscopy Study”, Chem. Eur. J. 2010, 16, 3815-3826.

5. K. Ichikawa, T. Matsumoto, J. Magnetic Resonance, 63, 445-453 (1985).

6. R. J. Gale, B. Gilbert, and R. a. Osteryoung, “Raman spectra of molten aluminum chloride: 1-butylpyridinium chloride systems at ambient temperatures", Inorganic Chemistry 17(10), pp. 2728{2729 (1978).

7. P.K. Lai and M. Skyllas-Kazacos, “Electrodeposition of aluminum in aluminum chloride/1-methyl-3-ethylimidazolium chloride", Journal of electroanalytical chemistry 248, pp. 431{440 (1988).

8. David Linden and Thomas. B. Reddy, editors, Handbook of Batteries volume 17, McGraw-Hill New York 3rd edition (2002).

9. Manickam Minakshi, Dominique Appadoo, and Danielle E. Martin, "The anodic behavior of planar and porous zinc electrodes in alkaline electrolyte", Electrochemical and Solid-State Letters 13(7), pp. A77-A80 (2010).

10. Gholam Abbas Nazri, Gianfranco Pistoria, "Lithium Batteries: Science and Technology", Springer Science, LLC, 2003.

11. Vijay A. Sethuraman, Kristin Kowolik and V. Srinivasan, "Increased Cycling Efficiency and Rate Capability of Copper-coated Silicon Anodes in Lithium-ion Batteries", Journal of Power Sources, 196 (1), 393-398, 2011.

12. Thomas B. Reddy, "Lindens Handbook of Batteries", Fourth edition, McGraw-Hill.

13. A. A. Arie, O. M. Vovk, J. O. Song, B. W. Cho, J. K. Lee, "Carbon film covering originated from fullerene C60 on the surface of lithium metal anode for lithium secondary batteries", J. Electroceram (2009) 23:248-253.

14. S. Ghosh, W. Wen, R. C. Urian, C. Heath, V. Srinivasamurthi, W. M. Reiff, S. Mukerjee, V. Naschitz and S. Licht, "Reversible Behavior of K2Fe(VI)O4 in Aqueous Media In Situ 57Fe Mo¨ssbauer and Synchrotron X-Ray Spectroscopy Studies", Electrochemical and Solid-State Letters, 6 (12) A260-A264, 2003.